UNIVERSITY OF CALIFORNIA,
IRVINE

On the Effects of Clapping on the Aerodynamics and Flight Mechanics of Bio-inspired Flapping Robots

DISSERTATION

submitted in partial satisfaction of the requirements
for the degree of

DOCTOR OF PHILOSOPHY

in Mechanical and Aerospace Engineering

by

Dipan Deb

Dissertation Committee:
Associate Professor Haithem E Taha, Chair
Adjunct Professor Robert Liebeck
Assistant Professor Jacqueline Huynh

2023

DEDICATION

I would like to dedicate my thesis to my incredible friends, loving family, and dedicated labmates. Without their direct and indirect support, this journey would not see the light at the end of the tunnel.

TABLE OF CONTENTS

LIST OF FIGURES

LIST OF TABLES

ACKNOWLEDGMENTS

Firstly I would like to thank my advisor Professor Haithem E Taha, who has been a friend, philosopher and guide in the true sense throughout my PhD journey. I would like to thank him for his unwavering support towards me and my work and taking time to answer even my mundane and frivolous questions and doubts. Secondly I would like to acknowledge the contributions and collaborations of my friend and colleague Kevin Huang and Moatasem Fouda. We learned, built and trouble shot experimental methods and setups together and also had fun doing that. Moreover, I would like to thank my friends Afreen Syeda, Vishnu Kunchur and Kavyakantha R S for their contribution and mental support during my PhD. Even though their professional backgrounds hardly overlap with mine, their curiosity about my work motivated me to push my boundaries. Furthermore, I would like to acknowledge the support provided by my friends and colleagues Mahmoud Abdelgalil, Asmaa Eldesoukey, Abdelrahman Elmaradny, Laura Olea, Nabil Khalifa, Purushottam Verma, Michelle Manku, Aakash Verma and Miquel Manich.

I would also like to thank the National Science Foundation and the Air Force Office of Scientific Research for funding the research work. My gratefulness also extends to the department of Mechanical and Aerospace Engineering and Holmes Family for blessing me with scholarships.

Additionally, I would like to show my gratitude toward the publishers of Bioinspiration & Biomimetics and Scientific Reports for providing me permission to incorporate the published works into my dissertation.

VITA

Dipan Deb

EDUCATION

Doctor of Philosophy in Mechanical and Aerospace Engineering **2023**
University of California Irvine *Irvine, California*

Master of Technology in Aerospace Engineering **2018**
Indian Institute of Technology Kanpur *Kanpur, UP, India*

Bachelor of Engineering in Mechanical Engineering **2015**
Indian Institute of Engineering Science and Technology Shibpur *Shibpur, WB, India*

RESEARCH EXPERIENCE

Graduate Research Assistant **2019–2023**
University of California, Irvine *Irvine, California*

Graduate Research Assistant **2017–2018**
Indian Institute of Technology Kanpur *Kanpur, UP, India*

TEACHING EXPERIENCE

Teaching Assistant **2020–2023**
University of California, Irvine *Irvine, California*

Teaching Assistant **2018**
Indian Institute of Technology Kanpur *Kanpur, UP, India*

REFEREED JOURNAL PUBLICATIONS

Flow visualization and force measurement of the clapping effect in bio-inspired flying robots **2021**
Bioinspiration and Biomimetics

Thrust enhancement and degradation mechanisms due to self-induced vibrations in bio-inspired flying robots **2023**
Scientific Reports

REFEREED CONFERENCE PUBLICATIONS

Effect of Self-Induced Body Vibrations on Thrust Generation in Bio-inspired Flying Robots **Jan 2022**
AIAA Scitech 2022 Forum

Effect of System Generated Perturbation on the Measurement of Average Thrust for a Bio-inspired Flapping Wing Robot **April 2021**
SoCal Fluids

Analysis of the Clapping Effect in Bio-inspired Flapping Wing Robots **Fall 2020**
APS Division of Fluid Dynamics Meeting Abstracts

Analysis of Clapping Effect in Bio-inspired Flapping Wing Mechanism **April 2019**
SoCal Fluids

Experimental Investigation and Design of Bio-Inspired Flapping-Winged Micro-Air-Vehicles (FWMAVs) **2023**
IDETC-CIE

ABSTRACT OF THE DISSERTATION

On the Effects of Clapping on the Aerodynamics and Flight Mechanics of Bio-inspired Flapping Robots

By

Dipan Deb

Doctor of Philosophy in Mechanical and Aerospace Engineering

University of California, Irvine, 2023

Associate Professor Haithem E Taha, Chair

Whenever we look at nature for inspiration, it never disappoints us. Either explicitly or implicitly, the technological know-how of mankind is greatly inspired and derived from natural provenance. The field of aerodynamics is not an exception; a clear example is the recent branch of Bio-inspired flapping robots (BIFRs), alternatively Flapping Wing Micro Air Vehicles (FWMAVs). Despite its inherently complex and intriguing aerodynamics and flight mechanics, the realm of flapping flight continuously surprises us with its numerous exciting potentials. The presence of wing-wing interaction in flapping flight is an example of such potential. One particular type of this wing-wing interaction is commonly known as the 'clapping effect', which is the main focus of this Dissertation. The aerodynamic performance of clapping wings, in terms of mean thrust production, exceeds that of a traditional flapping mechanism with no wing-wing interaction. In order to analyze the performance of the 'clapping effect', four different FWMAV models were developed, varying in the extent of wing clapping, and their aerodynamic performances were assessed in terms of thrust and power consumption at different flapping frequencies. The results indicated that the clapping effect enhances aerodynamic performance in terms of thrust generation. In order to explain the observed results, a flow visualization setup was constructed to gain insight into the flow field and the underlying vortex interaction. Additionally, BIFRs experience time-periodic aero-

dynamic forces, which induce oscillations in the body motion around the mean trajectory. These oscillations affect the performance of two-winged and four-winged BIFRs in different ways since both robots rely on different mechanisms for thrust generation. We constructed two different experimental setups: one that allows free vibration in one direction and another that does not allow any vibration. To measure the self-induced vibration, a motion capture system was used. The four-winged robot with the clapping effect, which was already superior in thrust production in a stationary environment, was found to be even more efficient in an oscillatory environment, in contrast to its two-winged counterpart with a traditional flapping mechanism. Moreover, flow visualization unveiled the reason behind such behavior, which also lies in vortex interaction. The superiority of the clapping effect is not confined to aerodynamic performance. It was found to exploit a significantly more robust vibrational stabilization mechanism, in comparison to the two-winged model that does not enjoy wing-wing interaction; the four-winged robot possesses a stable equilibrium beyond a critical frequency.in contrast to the two-winged model, which did not exhibit a stable response at any flapping frequency in the range considered for this study. In conclusion, we found that the clapping effect leads to a significantly more efficient thrust production, allows exploitation of the self-induced vibration for further thrust augmentation, and promotes vibrational stabilization. All these benefits are utilized in a new drone concept, named the quadflapper. The quadflapper is propelled by four four-winged robots. The inherent clapping effect of these flapping robots is used to maneuver and control the quadflapper in a smooth manner.

Chapter 1

Introduction

1.1 Motivation

Bio-inspired flying robots (BIFRs), more specifically Flapping Wing Micro Air Vehicles (FWMAV), have been a major focal point of research in the aerodynamics, dynamics, and control community in the last few decades. In the last century, the main attention was directed toward uncovering the unconventional lift mechanisms in flapping flight. With the more precise observation of the insect flight and how they make use of the unsteady lifting mechanisms (e.g., wake capture, leading-edge vortex, etc.), this puzzle was resolved [31] [24] [28]. Having understood the lifting mechanisms in insect flight, several researchers independently developed unique designs for FWMAVs [1] [34]. Although these designs are far from being saturated, flapping flight exhibited new potential through the wing-wing interaction. The mechanism responsible for the wing-wing interaction is named 'clap-and-peel' ('clap-and-fling' for rigid wings) [5] [6] [48]. This mechanism is found to be responsible for demonstrating vibrational stabilization in flapping flight [66]. Moreover, the clap-and-peel mechanism is utilized in a novel drone concept named 'Quadflapper' [42]. The Quadflapper

is easy to maneuver and robust in control as compared to a traditional drone. Since the clap-and-peel exhibited these characteristics, there was a need to study the aerodynamics and flight mechanics of this particular mechanism, which is also the motivation of the current dissertation.

1.2 Background

Over the last two decades, flapping-wing micro-air-vehicles (FWMAVs) have received significant attention within the scientific community. In 2005, the Defense Advance Research Project Agency (DARPA) has opened a contest to develop a Nano air vehicle (NAV), which was defined as an autonomous flying machine whose maximum dimension is less than 15 cm, with a very light weight (<10 gram) and capable of performing a variety of civil and military applications [1, 34]. These miniature vehicles were meant to be for indoor reconnaissance and surveillance. With the successful development of the NAV Hummingbird by Aerovironment, it was shown that hovering and forward flight could be attained through flapping-wing only propulsion [38].

One of the most special micro air vehicles is the flapping-wing type that flies like insects or birds, inspired by their Biology or Bio-inspired flapping robot (BIFR). Flapping insects use unconventional aerodynamic mechanisms (eg. leading edge vortex) to create high lift at ultra-low Reynolds numbers [26, 30, 24]. They also exploit unconventional stabilization mechanisms (eg. vibrational stabilization) to stabilize their bodies during flight and recover from gust disturbances [72, 71, 65, 33, 69].

One of the most challenging flying conditions of flapping flight is hovering. There have been numerous studies to investigate the aerodynamics of hovering flapping flight. Weis-Fogh tested the quasi-steady assumption for insect flight, where unsteady effects are more

conspicuous, and showed that quasi-steady aerodynamics can predict the main features of hovering flights [77]. However, Ellington [27] examined the results of Weis-Fogh's in the light of more accurate kinematic and morphological data, and his conclusion was opposite to that of Weis-Fogh's. Ellington [29] further showed that the leading edge separation bubble plays a prominent role in the hovering flight of insects. In comparison to a thin airfoil, Ellington asserted that the leading edge bubble modifies the camber and the thickness of the thin profile which enhances lift at low Reynolds numbers. Bayiz et al. (2018) [11] compared the hovering efficiency in rotary and flapping modes using rigid rectangular wings. They observed that flapping wings are more efficient in achieving a higher average lift coefficient in hovering. Sarkar et al. (2013)[61] studied aerodynamic performance under asymmetric flapping kinematics using sinusoidal and triangular waveforms. The frequency-asymmetry mechanism showed an increase in aerodynamic loads for the sinusoidal case. During the faster stroke, the lift can be enhanced depending on the level of asymmetry. The results of these investigations can be used to design an efficient flapping robot for hovering.

Recently, several research groups have independently developed different unique designs. Harvard engineers [80] designed and built the smallest FWMAV, the AeroVironment nano humming-bird set the standard for the flight performance and control of FWMAVs [41], and TU Delft developed the well-known Delfly family which uses a bi-plane flapping configuration [18, 17]. Inspired by their corresponding biological flyers, FWMAVs usually hover using a horizontal stroke plane [25, 56]. This design allows two degrees of freedom for the wing (assuming rigid): back-and-forth flapping and pitching. However, the stringent size, weight and power (SWaP) constraints typically imposed on the design of FWMAVs urged most of the concepts [25, 62, 70, 54] to adopt passive control for the pitching angle. On the other hand, in order to achieve optimal flapping performance, one may have to use active control of the wing pitching angle [12, 86]. Hence, it is of great interest to design actuation mechanisms that not only control the flapping angle [15], but also allow control of the pitching angle using only one driver motor.

(a) Commercial flapping wing drone [2]

(b) Modified version of the Flapping Wing Air Vehicle with an active mechanism (top view)

Figure 1.1: Commercial flapping drone and our modified version with an active pitching mechanism

Balta et al. [9] developed a novel active pitching mechanism, which controls both the pitching and flapping angles using only one actuator. This mechanism can achieve a pitching motion profile that is synchronized with the flapping motion, hence improving the performance of the FWMAV. In order to construct an air vehicle with this new flapping mechanism, we modified a flapping drone from the available market, shown in Figure 1.1a. This flapping drone uses a passive pitching mechanism that powers four wings (two pairs of wings), which clap once during each cycle.

The flapping mechanism of the commercially available flapping drone is neatly manufactured. So, we opt to modify it rather than manufacture a whole new mechanism. The modification procedure is as follows: from a passive mechanism that powers four wings to a passive mechanism that powers two wings, and then to an active mechanism that powers two wings, as shown in Figure 1.1b. While doing so, we found that the thrust capability considerably decreases when the passive four-wing air vehicle is transformed into the corresponding passive two-winged air vehicle. In other words, a FWMAV with four wings that flies by clapping its wings generates a considerably larger thrust than a FWMAV with two wings having the same frequency and double the stroke angle. It should be noted that this behavior is not intuitive since the generated thrust depends linearly on the number of wings and quadratically on

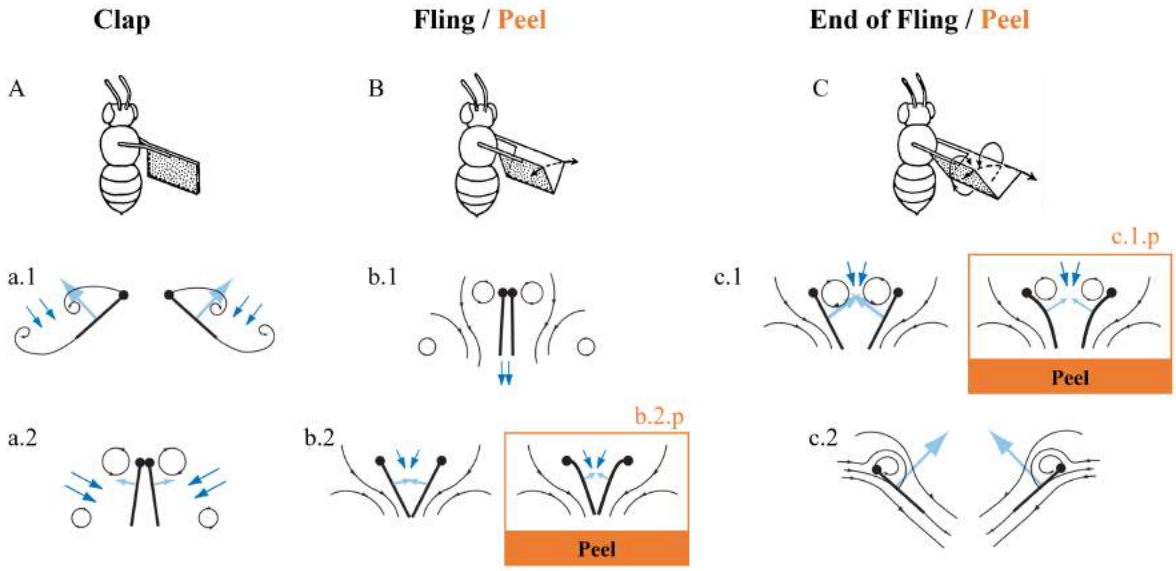

Figure 1.2: Summary of the clap-and-fling/peel mechanism based on the previous literature. Images A, B, and C are from Weis-Fogh [78, 79]. Images a.1, a.2, b.1, b.2, c.1, and c.2 are from SP. Sane [60]. Images b.2.p, and c.1.p are from Tay [74]. The flight sequence goes from A to C, or from a.1. to c.2

the stroke angle. The unconventional aerodynamics of this phenomenon urged the team to study the thrust generation mechanism due to clapping in more detail.

In fact, the clap and fling mechanism has been widely studied over the past few decades. Weis-Fogh was the first to point to lift enhancement in insects and birds due to clap and fling [78, 79], which triggered several research efforts in this direction ([54, 5, 15, 39]). Sane studied the improvement of flight forces by some mechanisms, such as the wing-wake interaction, at different angles of attack [60]. Tay et al. investigated the impact of the size on force production [74]. Their explanation of the clap-and-fling/peel mechanism are summarized in Figure 1.2. However, the more recent results of Martin et al. [52] concluded that such a lift enhancement actually depends on the Reynolds number. Moreover, even when there is a clapping lift enhancement, the strength of such enhancement also depends on the Reynolds number [53], which may highlight the important role of elasticity in this mechanism.

The effect of flexibility on clap and fling motion has also been studied concluding that

flexible wings are more effective in generating desirable forces [57, 58, 52], which is intuitively expected. Moreover, it was found that more flexible wings adjust their feathering angle in a way mitigates undesirable phase delay, which leads to an increase of the aerodynamic force [54]. The benefit is also extended to the efficiency, where FWMAVs with flexible wings are proven to passively increase their efficiency, as they store and release elastic energy every cycle [59, 85]. Effects of different aspect ratios and stroke angles have been investigated in the context of vortex dynamics in clapping motion [43].

Mathematical modeling of aerodynamic forces during clap-and-fling in FWMAVs is quite a challenging task due to the associated rich flow physics. The first models [76, 60] focused on studying multiple flight cases and proved that wing-wing and wing-wake interactions provide exceptional lift enhancement beyond steady aerodynamic properties. Percin et. al [58] have investigated wing kinematics with structural deformation measurement synchronized with force and power consumption. They found out that the wing-wing interaction not only creates favorable flow condition but also influences the aerodynamic forces through changing the effective wing geometry. Moreover, they observed a favorable effect of increasing aspect ratio on the force to power consumption ratio (i.e., efficiency). Armanini et al. [5] focused on producing a model for the time-resolved aerodynamic forces in the clap-and-fling mechanism. They realized that in order to construct a model that predicts accurately the time-variation of the lift force during clap and fling of the test platform, it is essential to account for the wing-wing interaction (they did it by including a fling circulation factor). Additionally, in their following work on clap-and-peel [7], they were able to decouple the effect of wing-tail interaction and model it separately from the wing's. This addition improved their estimation of the lift force and provided more clarity on the impact of each characteristic of the model.

A comparison between different flight mechanisms in insects, birds and bats, was carried out by Marden [51]. He realized that the majority have the same lift generation during takeoff except for the ones that exploit clap-and-fling, which created about 25% more lift. Later,

Cheng and Sun [16] performed a comparative study between full clap and partial clap by numerically solving the Navier-Stokes equations. Based on their analysis of the pressure distribution over the wings, it was concluded that partial clap motion is more practical for insects. It enhances the lift force without negatively impacting their efficiency. Nakata et. al [54] have investigated the flexible wing aerodynamics of a bio-inspired flapping MAV by combining CFD with wind tunnel measurements. They have showed that using the same model, the four-wings MAV generates twice the lift force of its two-wings counterpart, at body angle larger than 40^0. Also, they found that the two-wings MAV with a softer Mylar wings generates more lift forces than the four-wings MAV in case where the body angle was larger than 30^0, which shows the paramount role of aeroelasticity in the clap-and-fling mechanism. Additionally, Tay et al. [74] proved using their quantitative model that even if the flapping wing MAV is reduced to a size of an insect, the X-wing configuration provides two times more lift force than a regular two-wing model. These results were also validated by Nguyen et al. [55], who found a 44.82% more lift in the four-wings compared to two-wings using an own model similar to the "DelFly II". Lehmann et al. [48] found an increase of lift of 17% when using two computer-controlled rigid wings that were designed to clap-and-fling. This lift enhancement is considerably less than that by the other researchers, reported above, because the wings were significantly more separated on the closing stage. Finally, Jadhav et al. [39] performed a focused study on the clap portion of the clap-and-fling. Using CFD and PIV, they found that the closer the clap, the higher the lift generated.

These results point to the important role played by closing gap at the end of clapping, which has not been duly studied in the literature using flexible wings (perhaps Cheng and Sun [16] is the most relevant effort that gave some attention to this study). Other research efforts have studied the effect of the gap at the end of the stroke, but did not find a major increase in the vertical force during those moments [47, 45, 8]. However, these efforts were using rigid wings, which may point to the importance of flexibility in exploitation of clap and fling, as discussed by Nakata et. al [54]. Therefore, it urges a more detailed experimental research

with proper FWMAV models that are specifically developed for the comparative study.

To assess the effect of full and partial clapping and the aerodynamic mechanism that generates such an increase in thurst forces, we engineered four FWMAV models with: (i) four wings that fully clap, (ii) four wings that partially clap, (iii) four wings that do not clap, and (iv) two wings. We analyzed the thrust and power characteristics of each FWMAV model at different flapping frequencies. In the light of these force and power measurements, we conducted flow visualization to obtain physical insights into the reason behind the clapping unsteady lift enhancement mechanism.

Moreover, it is important to emphasize that when an insect hovers over a flower, it is not completely stationary in space over the flower. Instead, it undergoes oscillatory motion in almost all directions. These oscillations can be observed in the video, Hedrick and Daniel (2006) presented in the supplementary section of their paper [35]. Hence, it experiences self-induced vibrations. This vibration may change the flow field around the wing and thus affect the generated aerodynamic forces. In ideal hovering, there should be no self-induced vibration but in real cases, these vibrations are unavoidable due to the inevitable oscillatory nature of the driving aerodynamic forces. To the authors' best knowledge, there is little effort exerted that focuses on this point [73] [84], and the effect of self-induced vibration on the clapping mechanism is significantly under-explored. In this thesis, we studied the effect of self-induced body vibration in the flapping flight. To achieve this goal, we considered two different setups for aerodynamic force measurement (specially thrust) : (1) Pendulum setup or oscillatory test and (2) Load cell setup or fixed test. In the pendulum setup, we replaced the mass of a pendulum with a flapping wing robot. Whenever the robot flaps, it generates thrust and moves upward along the circular trajectory of the pendulum, assuming equilibrium at some angular position. We can measure this angle and use it to calculate the average thrust. We prefer this pendulum setup over the Harvard Robofly experimental setup (moving along vertical rails) [81] because it allows multiple equilibrium positions at different

flapping frequencies. Hence, the thrust can be estimated via a simple measurement of the angular position of the pendulum rod. In contrast, if the thrust of a flapping robot moving along vertical rails is different from its weight, the robot will continuously move up (or down); and estimating the thrust will require accurate measurement of the acceleration/deceleration of the robot. Clearly, measuring the angular position of the pendulum rod is simpler and more accurate than measuring the acceleration of a vibrating body. Also, this is a standard setup used to measure thrust generated by rotary wings [22]. The flapping robot vibrates about the angular position i.e., the measured thrust includes the effect of vibration. In contrast, in the loadcell or fixed test setup, there is no room for such a vibration. So using these two setups, we can measure the effect of self-induced vibration on flapping thrust generation.

Two BIFRs are considered for this study: one has two wings and the other has four wings. The one, that is two-winged, is named Model A. The wings of these models have a stroke angle of $\sim 60^0$. Unsteady responses like leading edge vortex [31], wake capture [24] [60] are utilized by the two-winged model in flapping flight. The four-winged model or Model B exploits a wing-wing interaction phenomenon named 'clap-and-peel' for generating thrust. There has been a surge of interest in recent years to study the interaction of multiple bodies in a fluid flow [36] [21] [44]. Deb et al.(2020) [21] observed in-phase and out-of-phase oscillations in a couple of rigid plates which are oriented one beside the other, through wind tunnel experiments. They explained the modes of oscillation of the plates through flow field data and visualization. Some studies also included flexibility. Flexible flags in different orientations like tandem and side-by-side and their interaction in those configurations were studied by Alben (2009) [3]. In flapping flight, wing-wing interaction has been exploited by the four-wings model by using 'clap-and-fling' [39] (for flexible wings -'clap-and-peel' [6]) to generate thrust. Outcomes of wing-wing interaction like stronger leading edge vortex [5] and jet effect [39] [48] are utilized for thrust generation by the clap-and-peel mechanism. Balta et al. (2021) [10] showed with flow visualization that the peeling phase of the flapping cycle

draws air in and the clap phase propels it downstream; that thrust is augmented using a jet effect (Figure 1.2. A blob of air flows between the wings in the peeling phase, which strengthens the leading edge vortex. Some efforts were made to capture the clapping effect into an aerodynamic model [49] [46] [83]. Armanini et al. [5] studied the improved strength of the leading edge vortex during clapping and included this phenomenon in a quasi-steady aerodynamic model. They further studied the clapping-effect interaction with the tail-wake and wing-wake [6].

The mechanism for thrust generation in a four-winged robot is different from the conventional one due to the wing-wing interaction, or the clap-and-peel mechanism [10] [48]. Thus it is expected that the effects of the self-induced vibration will not be similar for the two-winged and the four-winged robots.

The perks of the clapping effect do not end at taking advantage of the self-induced vibration. It also exhibits a natural stabilization mechanism, known as vibrational stabilization. Vibrational stabilization is considered an unconventional method to achieve stability in an otherwise unstable equilibrium through the application of vibration. This intriguing occurrence was initially documented by Andrew Stephenson in 1908, using an inverted pendulum [64]. In contrast to a typical pendulum, which has a stable equilibrium at its lowermost point and an unstable equilibrium when inverted, the unstable point can attain stability when subjected to sufficiently fast vibrations. Notably, this counterintuitive stabilization phenomenon operates without the need for feedback control, relying solely on inherent dynamics. It was not until 1951 that Pyotr Kapitza elucidated the underlying physics of this phenomenon, employing the concept of effective potential [40], eventually leading to the pendulum being named after him. Achieving stability with the help of vibration is not confined to rigid body mechanics only. The utilization of vibration as a means to attain stability goes beyond the realm of rigid body mechanics. In a notable study, Apffel et al. (2020) successfully achieved stabilization of a levitating liquid layer through controlled container vibration [4]. Moreover,

their investigation extended to the remarkable feat of stabilizing a toy boat's inverted floating configuration, and they additionally substantiated the stability of this inverted water surface through analytical means.

The phenomenon of vibrational stabilization is observable in natural occurrences like the flapping flight of insects. In 2020, Taha et al. employed chronological calculus to elucidate the utilization of vibrational stabilization in response to pitch perturbations by a hawkmoth during hovering [69]. Furthermore, Taha, Kiani, and Navarro conducted experimental work illustrating vibrational stabilization in a two-degree-of-freedom system using a bio-inspired flapping robot [67]. This present study continues to adopt the two previously mentioned flapping robots: (i) Model A and (ii) Model B and similar experimental configurations, employing a system characterized by two degrees of freedom. Both models employ an identical crank-and-rocker mechanism for flapping and share the same wing material and geometry. The sole distinction between these robots resides within their aerodynamic characteristics.

In this study, both flapping robots have been affixed to the experimental apparatus, and the ensuing system behaviors are meticulously documented across varying flapping frequencies. Notably, a discernible dissimilarity in stability manifests between the two flapping robots at higher flapping frequencies.

Chapter 2

Experimental Methods

2.1 Introduction of the Flapping Robots

The research focus is on analyzing the aerodynamic performance of clap and fling mechanism due to wing-wing interactions. During the flapping cycle when wings come closer; it is called clapping and when it separates away, that part of the cycle is named as fling. Therefore, we developed four models with different wing configurations (see Figures 2.2, 2.3 and 2.4). The first model (A) has only two wings, the second model (B) has four wings that close and clap completely, the third model (C) has four wings that close and clap partially and the fourth model (D) has four wings that close partially but do not clap (thanks to the separator placed between the wings, see Figure 2.5).

The observation that triggered this study is the considerable difference in aerodynamic behavior between models C and D, which are almost identical, but the former claps partially and the latter does not clap. Then, by analyzing the two most different systems (models A, B), we can understand the underlying physics behind the boosted performance due to clapping. Comparisons are performed between the four models in terms of the average thrust

FWMAV	Description	Number of wings	Stroke angle	Weight
Model B	FWMAV with four wings and full close/clap	2 / side	35° / wing	8.17 gr.
Model C	FWMAV with four wings and partial close/clap	2 / side	37° / wing	8.37 gr.
Model D	FWMAV with four wings, partial close and no clap	2 / side	37° / wing	9.8 gr.
Model A	FWMAV with two wings	1 / side	60° / wing	7.36 gr.

Table 2.1: Description and basic properties of each FWMAV used in the research

and power consumption at different flapping frequencies. Additionally, the flow dynamics have been qualitatively captured using a flow visualization setup.

2.2 Characterization of the Models

The Flapping Wing Micro Air Vehicles used in the experiment have the same characteristics except for the mechanism. As discussed in our previous effort [9], the mechanism is a crank rocker, which transforms a circular motion into an oscillatory one. Model B uses two crankrocker mechanisms where two wings are attached to linkage 4 in the mechanism (see Figure 2.1). Therefore, the wings can clap completely. Models C & D have a modified mechanism that only allows the FWMAV to clap partially (see Figure 2.4b and 2.4c). This is achieved by increasing the length of rod 1, which is the base (see Figure 2.1b). As for model D, we added four rods on each side to prevent clapping (see Figure 2.5b). In model A the linkage 4 is replaced by a similar one that is attached to only one wing, as shown in Figure 2.2c. All models are equipped with the same wings, with a span of 28.2 cm and a maximum chord of 9.5 cm. The rest of the parameters are shown in Table 2.1.

The stroke angle of the wing is the angle enclosed by the two extreme positions of the wing during the cycle. In the four-winged models (B, C, D), the wings go from 0° to ±35°, which

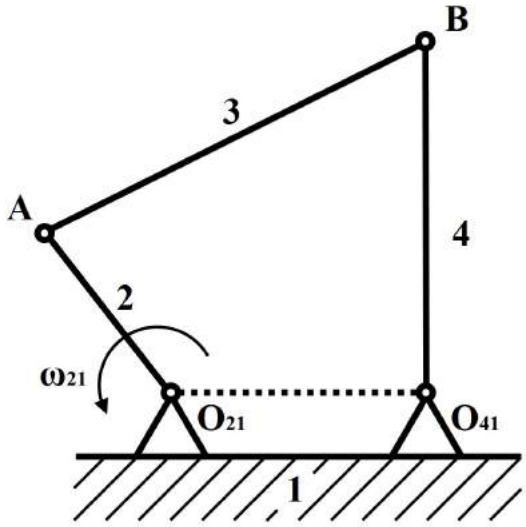

(a) Schematic of the crank rocker mechanism

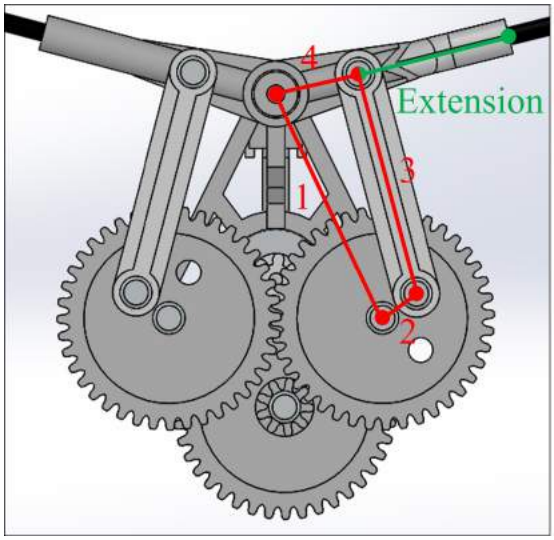

(b) Crank rocker mechanism from Model B

Figure 2.1: Crank rocker mechanism used in the models of this study

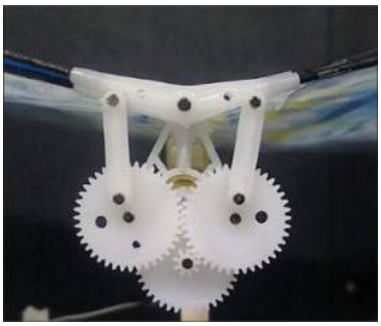

(a) Model B

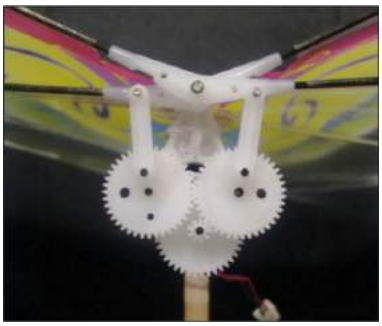

(b) Models C and D

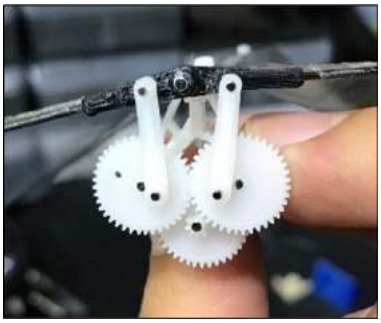

(c) Model A

Figure 2.2: Top view of the mechanisms used in each model of the FWMAV

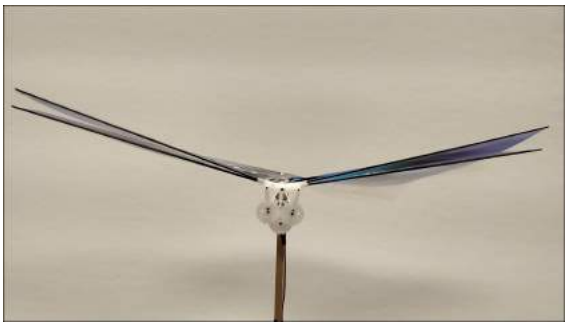

(a) Model B

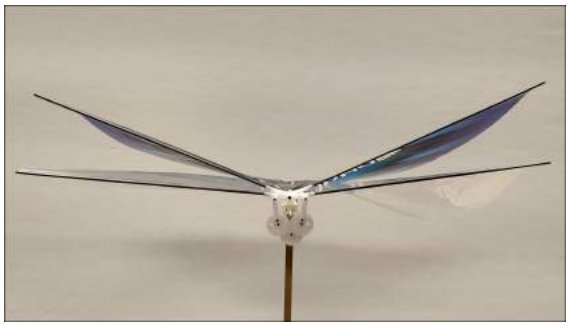

(b) Models C

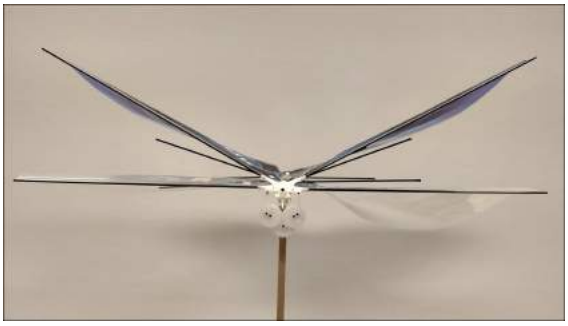

(c) Model D

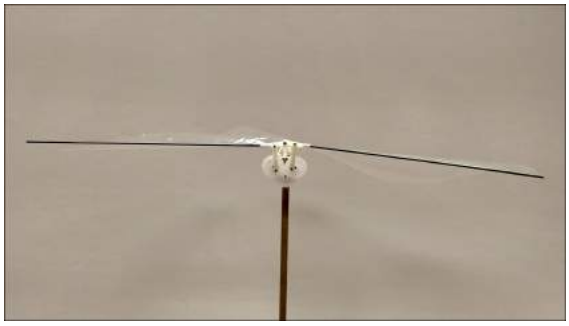

(d) Model A

Figure 2.3: Top view of the four models

means that the stroke angle of one wing is 35°. On the other hand, in the two-winged model (A), the stroke angle is 60°.

2.3 Averaged Thrust and Power Measurements

The experimental setup consists of a pendulum that has one degree of freedom, with the mass of the pendulum replaced by the flapping-wing MAV model, as shown in Figure 2.6. As such, at a given frequency, the steady state pendulum angle γ is used to estimate the averaged thrust T as:

$$T = \left(m_{\text{FWMAV}} + \frac{1}{2} m_{\text{rod}} \right) g \sin \gamma, \tag{2.1}$$

(a) Model B

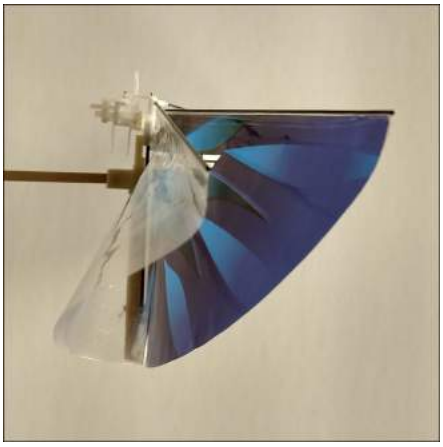

(b) Models C

(c) Model D

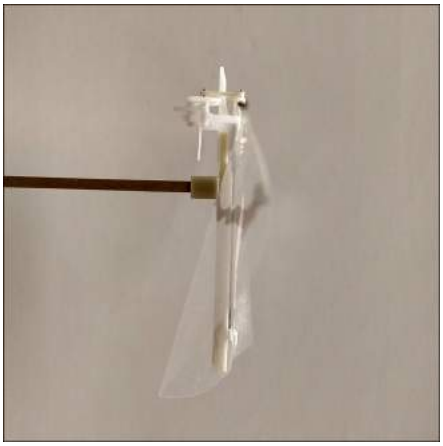

(d) Model A

Figure 2.4: Side view of the four models

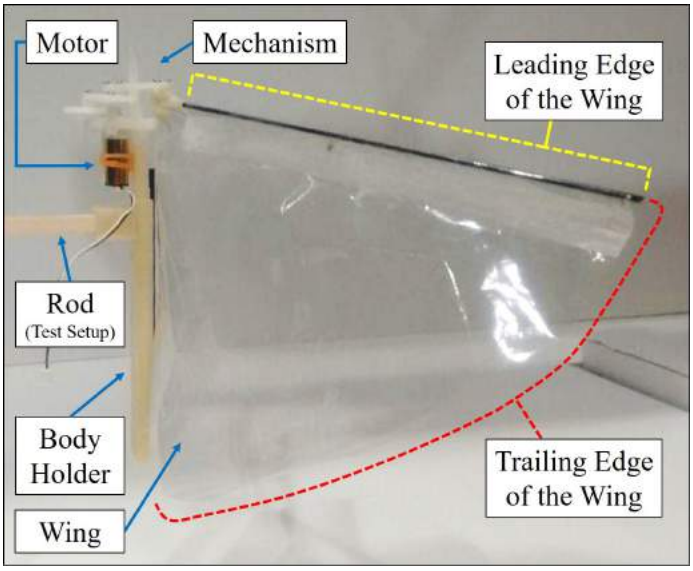

(a) Side view of the Model A

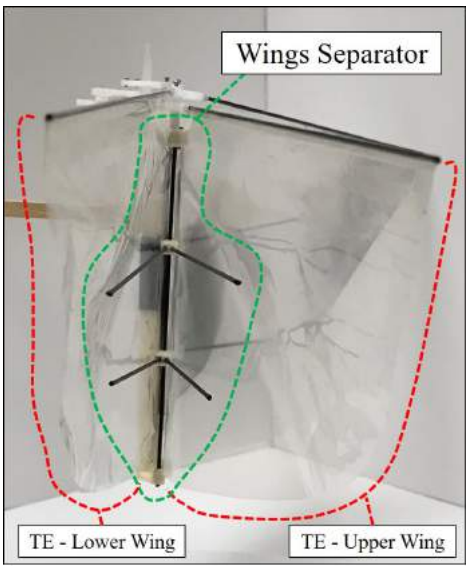

(b) Wings separator of the Model D

Figure 2.5: Side views of Model A and Model D, which show the separator structure used to prevent the wings from clapping.

where m_{FWMAV}, m_{rod} are the FWMAV and rod masses, respectively. In this test, we also read the provided voltage and current from the power supply to estimate the *total* averaged power consumption. This configuration is preferred over the Harvard Robofly experimental setup (moving along vertical rails) [82] because it allows multiple equilibrium *positions* at different flapping frequencies [65]. Also, it is preferred over a completely static configuration [54, 58, 7, 85, 39, 55] because it allows the FWMAV's body to oscillate around the hovering equilibrium; hence, it accounts for aerodynamic-dynamic interactions [72, 33]—mimicking hover more realistically. Moreover, the same test is repeated without wings to obtain the *mechanical* power consumption of the mechanism at different frequencies. Therefore, the *aerodynamic* power can be obtained from the relation:

$$\text{Aerodynamic Power} + \text{Mechanical Power} = \text{Total Power} \tag{2.2}$$

This aerodynamic power consumption is the main comparison metric used to assess the efficiency of a given model.

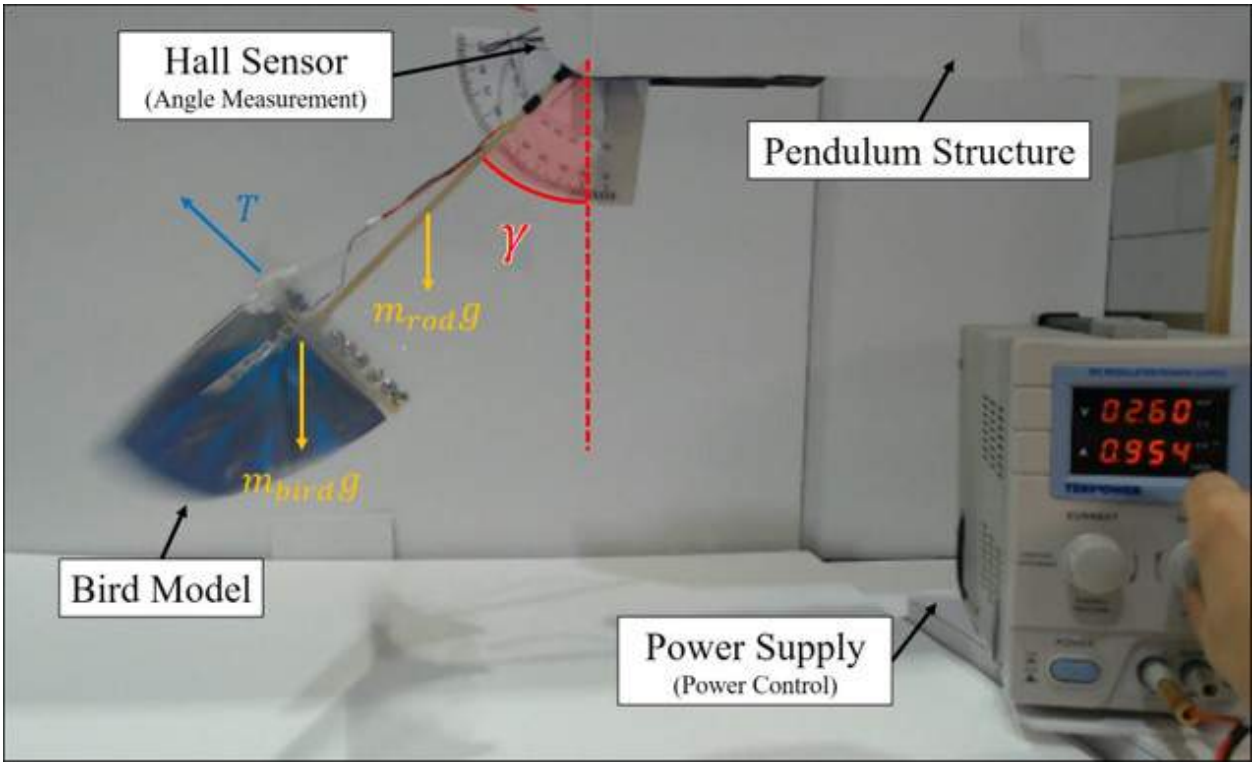

Figure 2.6: Average thrust and power test. The image shows the 1 DoF pendulum test with Model B.

2.4 Flow Visualization Setup

The flow visualization test allows us to study the qualitative physics due to the interaction between the wings and the surrounding air. Therefore, we can gain physical insight about the thrust enhancement observed in the average-force measurements. In this setup, the smoke machine creates a layer of smoke that moves with the flow over the wing, and is illuminated by a laser sheet. Then, using a high-speed camera, we obtain a qualitative picture of the flow field around one section of the wing. We perform this two-dimensional flow visualization over three different sections along the span of the wing. Figure 2.7 shows a schematic of the flow visualization setup, which consists of (a) a metallic support frame, which also protects the flow from ambient disturbances (its sides are covered using a black background, and the rest is open); (b) a smoke generator, which allows control of the intensity and speed of the smoke (for the current test, it is set at the slowest swap, so that it would not spoil

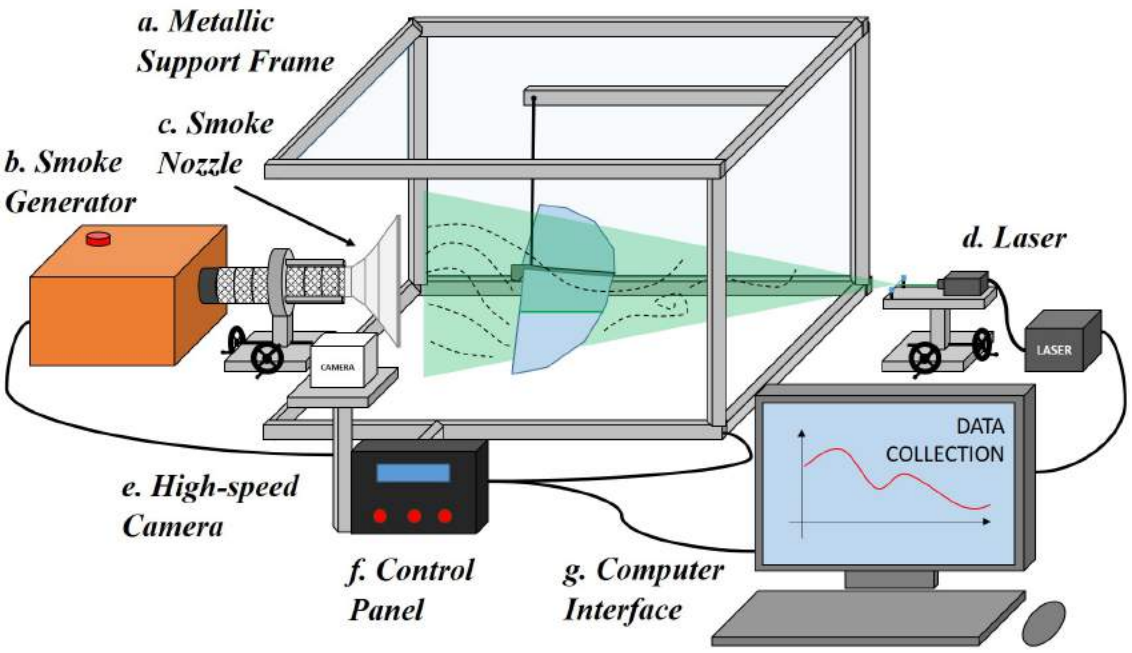

Figure 2.7: Flow visualization system setup (a) metallic support frame, (b) the smoke generator, (c) the smoke nozzle, (d) the laser, (e) the camera, (f) the control panel, and (g) the computer interface

the hovering configuration); (c) a nozzle attached to the smoke generator, which turns the generated smoke flow into a vertical plane to cover a two-dimensional plane over a specified wing section; (d) a laser beam with lens which turns it into a plane; (e) a high-speed camera; (f) a control panel, which is used to control the FWMAV's flapping frequency; and (g) a computer interface used to process the data.

2.5 Measurement with Self-induced Vibration

In order to investigate the effect of the self-induced vibration on Models A & B, we use different experimental setups like (1) Pendulum test or oscillatory test (Figure 2.6) and (2) Loadcell or fixed test (Figure 2.8) for measuring the thrust generated by the two above-mentioned models. We use uxcell 100g loadcell, with 1mV/V sensitivity. Each run includes

a one-second record of data with a sampling frequency of 5000 samples/second. The data is averaged over the maximum number of integer cycles within the data acquisition time span of one second. FFT is then performed for the time series of the measured thrust to estimate the flapping frequency. We trim an aluminum block to fit the loadcell onto it and we mount the FWMAV on the loadcell. The thrust signals from the loadcell are filtered twice before analysis. A hardware low pass filter of type USBPGF-S1 is used for the first stage of filtration. Subsequently, the signals are acquired by the NI DAQ and filtered again by a digital filter provided by the LabVIEW software itself. The same LabVIEW program helps to record the data as well. We have also included the structural response of the loadcell system in the appendix [63]. Whereas, in the previously mentioned pendulum test, the FWMAV body is free to oscillate. So, the effect of body-induced vibrations is already included in the measured average thrust.

On the other hand, the load cell test (Figure 2.8) measures thrust with time during the flapping cycle. By applying the time average to the obtained data, we can calculate the mean thrust at each given value of the flapping frequency. The loadcell setup consists of a uni-axial loadcell.

Figure 2.9 shows the variations of thrust coefficient with the flapping frequency of three different runs for the two (Fig: 2.9a) and four-winged (Fig: 2.9b) flapping models using both the loadcell (fixed test) and pendulum (oscillatory test) setups. Each run is performed at the same input power to the flapping mechanism. The error bars in both the frequency (horizontal bar) and thrust measurements (vertical bars) are presented. It is noted that the horizontal error bars in the pendulum setup are relatively larger than the loadcell setup, which is perhaps due to the less accurate measurement of the flapping frequency using the strobe light. However, it is within reasonable bounds and was deemed satisfactory for the current study. As for the observation, figure 2.9a shows the averaged thrust coefficient C_T measured for model A for given flapping frequencies. It clearly shows that the thrust

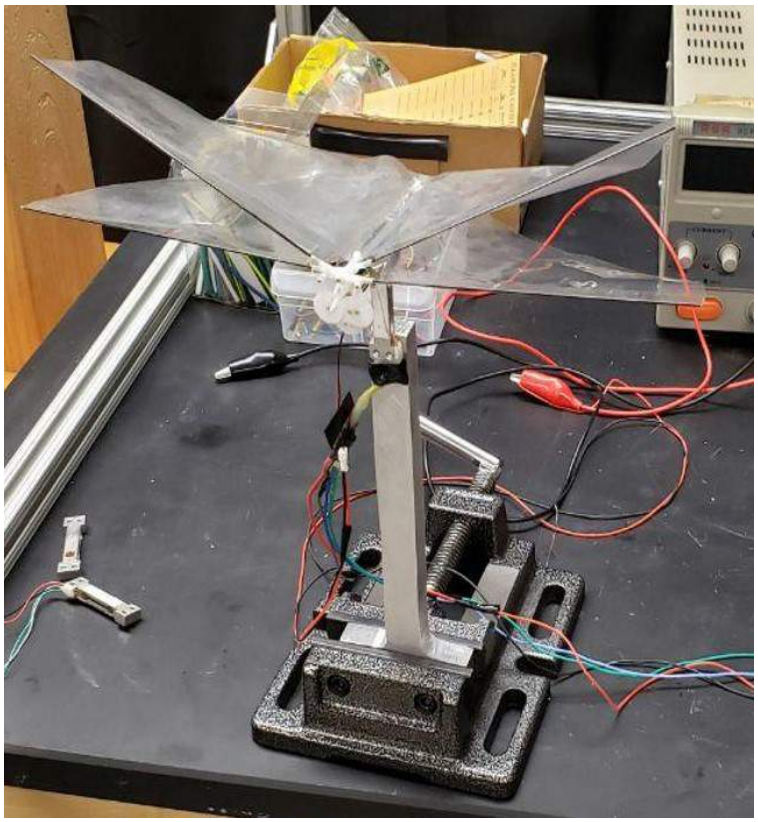

Figure 2.8: FWMAV mounted on a loadcell setup

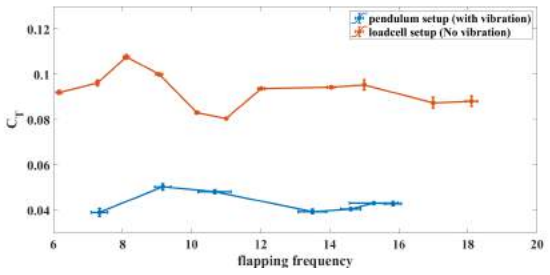

(a) C_T vs f for Model A

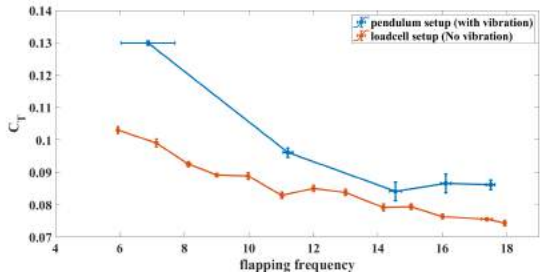

(b) C_T vs f for Model B

Figure 2.9: Comparison of thrust co-efficient for both the Models (A & B) from both the pendulum and loadcell setups with error bars

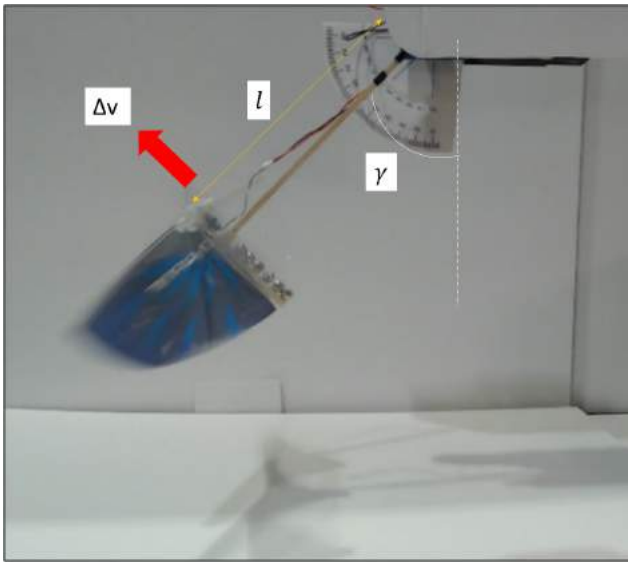

Figure 2.10: Δv measurement from the Pendulum angle

measurements from the oscillatory test are less than the fixed test. On the other hand, the situation is reversed for Model B as shown in Figure 2.9b. This clear difference in behavior is the focus of this study.

The generated aerodynamic forces by the FWMAVs are periodic in nature. Hence even after achieving a stable equilibrium in the system, the FWMAV oscillates about that equilibrium point. On the other end, the fixed test setup allows no such oscillation. Moreover, Model B exploits wing-wing interaction or clapping effect to generate thrust which differs from the thrust generation of Model A [10]. Thus the vibration also has different effects on the thrust generation and results in the opposite trend observed in Figure 2.9.

In order to investigate the effect of the vibration, we need to define it first. In the oscillatory test, the angular position of the FWMAV, denoted by γ, oscillates around a mean point γ_0, with a zero-mean periodic variation $\widetilde{\gamma}$. For a given flapping frequency we can say that the FWMAV assumes an angular location $\gamma(t) = \gamma_0 + \widetilde{\gamma}(t)$. Denoting the length of the wooden rod as l, the vibration velocity can be defined as $\Delta v = l\dot{\gamma}$. The red arrow shows the direction of positive Δv in Figure 2.10. The flapping angle ϕ is also measured simultaneously with the pendulum angle γ at a given point in time. For this purpose, we use a motion capture system

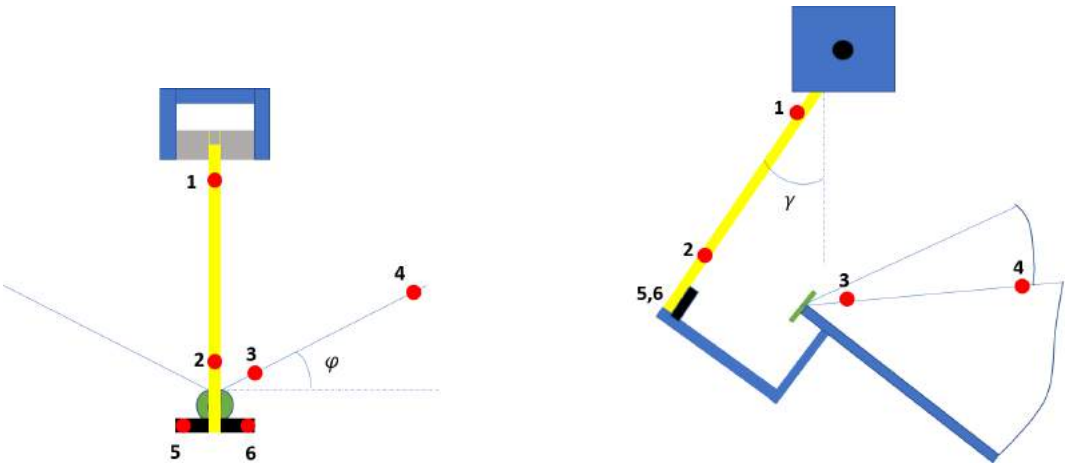

(a) View from the front (b) View from the side

Figure 2.11: Schematic of the FWMAV and the pendulum with the active markers

with one tracker and six markers as mentioned in this 2022 conference paper [19]. Figure 2.11 shows the positions of these markers. Figure 2.11b shows that the markers positioned on the wooden rod (1 & 2) are for measuring $\gamma(t)$, the markers on the leading edge (3 & 4) as shown in Figure 2.11a are for the measurement of $\phi(t)$, and the two markers (5 & 6) at the bottom of the rod are for defining local horizon. All these markers are active in nature. A 3D tracker receives signals from the markers and sends them to the computer. The tracker has 0.1mm spatial and $1\mu s$ temporal accuracy. The VZSoft software acquires the signal and records the data on the computer. We use MATLAB to read and process the data to observe the perturbation motion.

Flow visualization is executed to investigate the effect of the vibration in the flow field for both the models and the setups. The images captured for the cases with and without vibration, explain the flow physics underlying the performance observed in Figure 2.9. The visualization is captured for $6Hz$ flapping frequency with a camera at 240 FPS. As the laser sheet is two-dimensional, the visualization is done at different spanwise positions. These locations are demarcated in green in Figure 2.12.

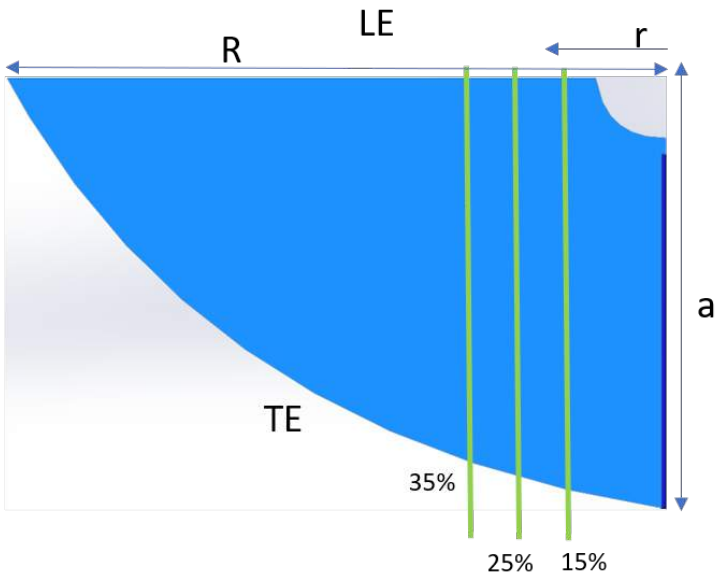

Figure 2.12: Visualization locations in the spanwise direction

2.6 System Response Measurement

Two different configurations of bio-inspired flapping robots are considered: (i) Model A & B. Both flapping robots, Model A and Model B, are able to flap with a crank-rocker mechanism, which is also utilized by Balta et al. [10] in the same laboratory. In our study, thrust measurements obtained from the same flapping robots (Models A and B) align with the established literature [10]. Consequently, it can be anticipated that the responses of the dynamical system will vary when tested with these distinct flapping mechanisms.

Figure 2.13 presents a schematic of the experimental setup used in the present work. The setup consists of a metallic frame (shown in light green), which serves as a mounting platform for the experimental setup. It is securely fixed to the laboratory floor. There is a pendulum rod (in yellow) mounted on hinge 'a'. The rod is allowed to rotate freely about the hinge, enabling it to swing like a regular pendulum. The pendulum angle between the pendulum rod and the vertical axis is denoted by γ. The BIFR (in blue) is mounted to the pendulum rod through a connecting rod (in green) at the hinge 'b' located on the robot as shown in

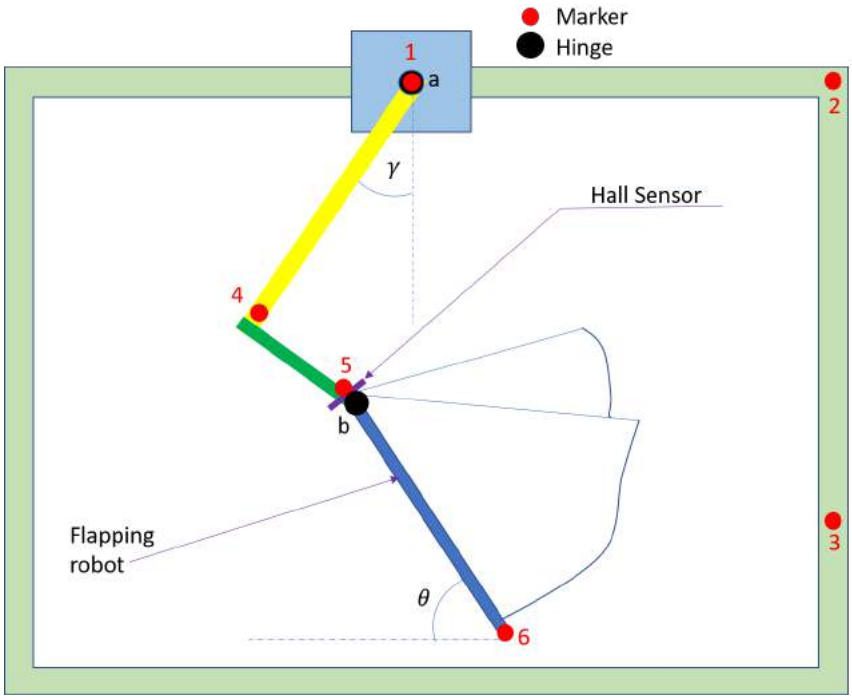

Figure 2.13: Schematic of the Experimental Setup with Marker locations.

figure 2.13. The body of the robot is free to rotate about this hinge. The body pitching angle between the BIFR body and the horizontal axis is denoted by θ. Whenever the robot flaps, depending on the frequency of flapping, γ and θ undergo oscillatory response about certain average values. These angles provide valuable information about the behavior and dynamics of the system under study. The angle θ represents the pitching angle of an animal or a BIFR in free flight, and the angle γ mimics the translatory motion of the BIFR. In fact, this reduced-degree-of-freedom setup is typical in the literature on helicopter stability and control [23].

In order to measure the angles synchronously, we have the previously mentioned motion capture system. This system consists of active markers and a tracker. Six markers (shown in red in figure 2.13) are strategically placed for measurements. Markers 1, 2, and 3 are fixed orthogonally on the metallic frame, providing a stable reference. Marker 1, placed on the hinge 'a', along with marker 4, allows for the measurement of the angle γ. The angle θ is measured with the help of markers 5 and 6. The signals are acquired from the markers at

500 samples per second. In addition to the angles γ, θ, a hall sensor is utilized to measure the flapping frequency of the BIFR.

Chapter 3

Aerodynamic Modeling

3.1 Basic Force and Power Analysis in the absence of Wing-Wing Interactions

Consider a wing section of width dr at a distance r from the wing root, as shown in Figure 3.1. The differential thrust force generated on this wing section is written as

$$dT(r,t) = \frac{1}{2}\rho(r\dot{\phi})^2 c(r) C_L dr \tag{3.1}$$

where $\dot{\phi}$ is the flapping angular speed, $c(r)$ is the spanwise chord distribution, C_L is the lift coefficient, and ρ is the air density. Integrating over the wing span, we obtain

$$T(t) = \frac{1}{2}\rho\dot{\phi}^2 C_L \int_0^R r^2 c(r) dr \tag{3.2}$$

Using the relation $\int_0^R r^2 c(r) dr = SR^2\hat{r_2}^2$, where S is the area of one wing and $\hat{r_2}$ is the non-dimensional second moment of wing area [26] and considering that $\dot{\phi} = \Phi\omega\sin(\omega t)$, the total thrust force by one wing is written as

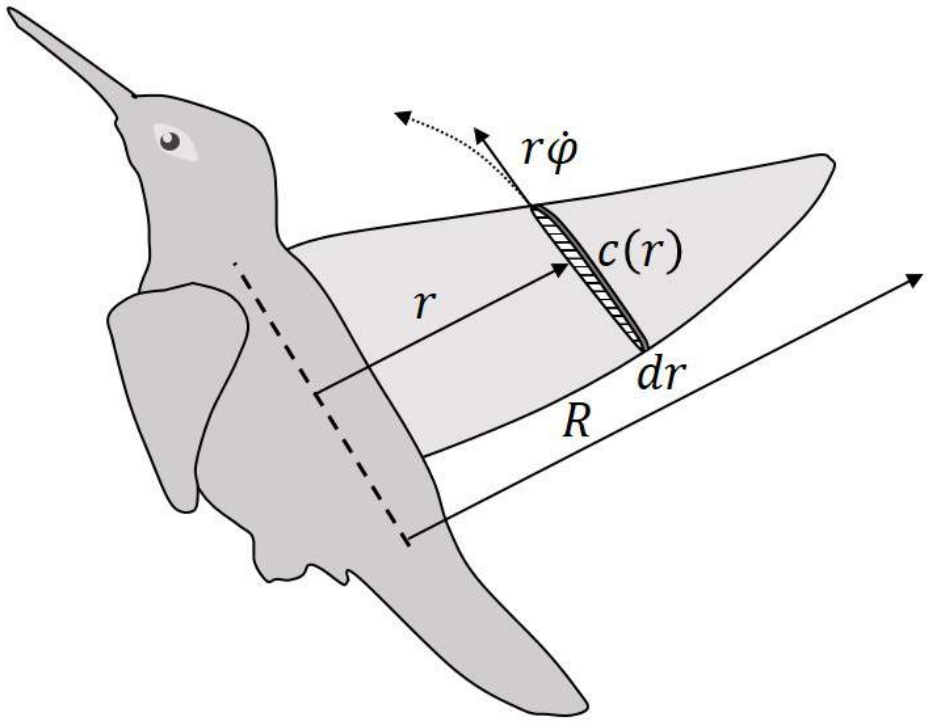

Figure 3.1: A schematic diagram of a flapping-wing animal

$$T(t) = \frac{1}{2}\rho R^2 \Phi^2 \omega^2 S \hat{r_2}^2 C_L \sin^2(\omega t) \tag{3.3}$$

Ignoring the aerodynamic effects due to wing-wing interactions (e.g., clap and fling), averaging over the flapping cycle and multiplying by the number of wings, the averaged thrust generated by a multi-winged FWMAV can be written as:

$$T = N\left(\frac{1}{2}\rho V_{ref}^2 S C_{T,1}\right) \tag{3.4}$$

where, N is the number of wings of a FWMAV, $C_{T,1}$ is the thrust coefficient for one wing, and V_{ref} is the reference speed, which is usually taken, at hovering, as the maximum flapping speed: $V_{ref} = 2\pi f R\Phi$, where f is the flapping frequency.

If the mechanism stroke angle is the same for all FWMAV models, any particular wing in a four-wings model will sweep half the stroke angle that is swept by its peer in a two-wings configuration (see Figure 3.2). Hence, since the above simple analysis shows that the total Thrust force varies linearly with the number of wings N and quadratically with the stroke amplitude Φ, then, it implies that the thrust force $T_{4,\Phi}$ generated from a four-wings model will be half that generated by a two-wings model, driven by the same mechanism at the same frequency: $\frac{T_{4,\Phi}}{T_{2,2\Phi}} = \frac{1}{2}$ if wings interactions are ignored.

Similarly, the differential drag force on the wing section is written as

$$dD(r,t) = \frac{1}{2}\rho(r\dot{\phi})^2 c(r) C_D dr \tag{3.5}$$

where C_D is the drag coefficient. The aerodynamic power consumed by this airfoil section is then written as $dP(r,t) = r\dot{\phi}dD(r,t)$. Hence, the total power consumed by one wing is

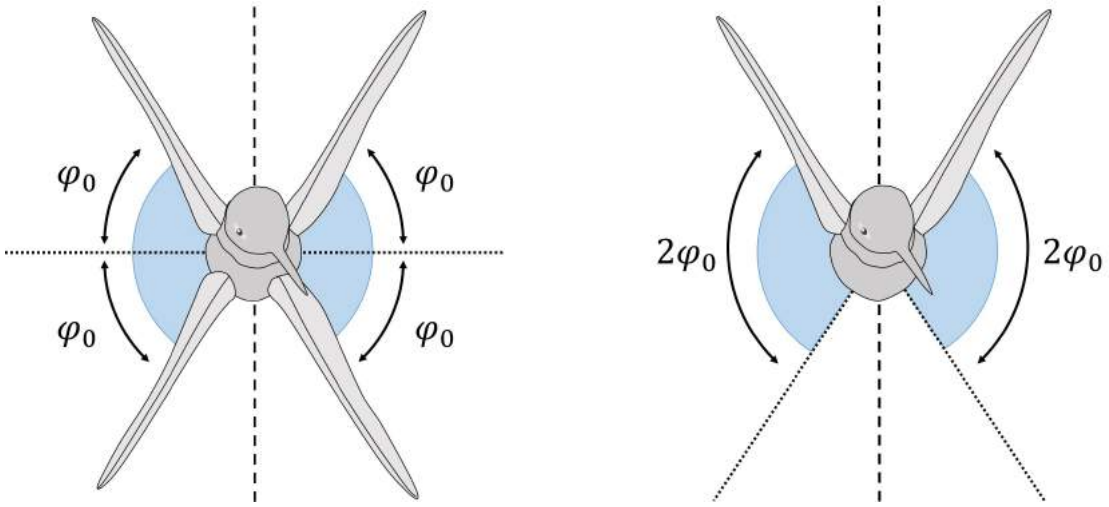

(a) FWMAV with four wings (Model B) (b) FWMAV with two wings (Model A)

Figure 3.2: Angle swept by an individual wing depending on the number of wings from the FWMAV model

given by

$$P(t) = \frac{1}{2}\rho\dot{\phi}^3 C_D \int_0^R r^3 c(r) dr \tag{3.6}$$

which results in

$$P(t) = \frac{1}{2}\rho R^3 \Phi^3 \omega^3 S \hat{r_3}^3 C_D \sin^2(\omega t)\sin(\omega t) \tag{3.7}$$

where $\hat{r_3}$ is defined as $\int_0^R r^3 c(r) dr = SR^3\hat{r_3}^3$. As such, the power consumed by a multi-winged FWMAV, ignoring wings interactions, is written as:

$$P = N\left(\frac{1}{2}\rho V_{ref}^3 S C_{P,1}\right) \tag{3.8}$$

where $C_{P,1}$ is the power coefficient of one wing. This aerodynamic power varies linearly with the number N of wings and cubically with the stroke angle Φ, which implies that aerodynamic power by a four-wings model, each sweeping a stroke angle Φ, would be one-fourth of a two-wings model, each sweeping 2Φ.

In conclusion, the above analysis implies that a two-wings model, each sweeping a stroke angle 2Φ, would produce double the thrust, but consume four times the aerodynamic power of a four-wings-model, driven by the same flapping mechanism (i.e., each wing sweeps Φ), if wing interactions are ignored. Moreover, both model types would have the same efficiency $\eta = \frac{TV_{ref}}{P} = \frac{C_{T,1}}{C_{P,1}}$, which is equal to the efficiency of one individual wing. However, these results were found to be contrary to our experimental measurements, as shown in the Results and Discussion chapter mainly due to the effects of wing interactions.

3.2 Aerodynamics Modeling with Error Minimization

To investigate the effect of perturbation velocity on flapping wing models (Model A and Model B), it may be prudent to develop an aerodynamic model for both models, which is the focus of this section. The backbone of the adopted aerodynamic model was proposed by Berman and Wang (2007) [13], who were studying the energy-minimizing kinematics in hovering insect flight. However, this aerodynamic model only applies to FWMAV with two wings (Model A), i.e., no wing-wing interactions. Armanini et al. [5] extended the applicability of this model to FWMAVs with four wings (Model B), by including the clapping effect.

3.2.1 Aerodynamic Model For Two-winged Robot

Figure 3.3 shows a cross section (blade element) of a wing at distance r from the body of the FWMAV. The red portion represents the chord of the section $c(r)$ and (x, y) makes the reference frame at the leading edge (denoted as LE) of the blade element. The green and blue arrows at the leading edge denote the direction of perturbation velocity (i.e., due to vibration) Δv and the flapping velocity $r\dot{\phi}$, respectively. The thrust generated per unit span

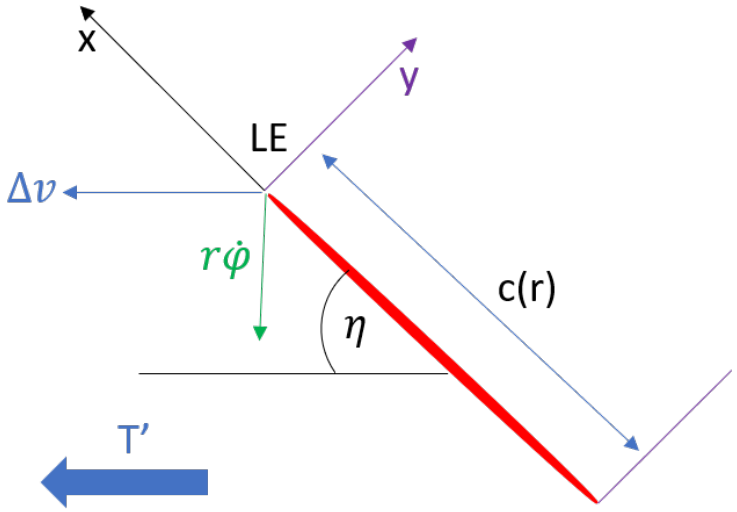

Figure 3.3: Cross section of the flapping wing at distance r from the body

is denoted as T' and can be expressed by the force generated per unit span in the x and y directions, F'_x, F'_y and the pitching angle η

$$T' = dT/dr = F'_x \cos\eta - F'_y \sin\eta \tag{3.9}$$

According to Berman and Wang [13] the forces F'_x and F'_y can be expressed in terms of the bound vortex Γ, added masses m_{11} and m_{22}, the velocity and acceleration components v_x, v_y, a_x & a_y and the viscous forces in those directions F'^v_x and F'^v_y

$$F'_x = -\rho\Gamma v_y - m_{11}a_x - F'^v_x \tag{3.10}$$

$$F'_y = \rho\Gamma v_x - m_{22}a_y - F'^v_y \tag{3.11}$$

The bound vortex Γ can be written in terms of the translational and rotational coefficients C_t & C_R, the total velocity $|v| = \sqrt{v_x^2 + v_y^2}$, as well as the angle of attack α and pitching

rate $\dot{\eta}$. The relation is shown in equation 3.12.

$$\Gamma = -\frac{1}{2}C_t c(r)|v|\sin 2\alpha + \frac{1}{2}C_R c^2(r)\dot{\eta} \tag{3.12}$$

The viscous force F'^v are given by

$$F'^v = \frac{1}{2}\rho c(r) C_D |v| < v_x, v_y > \tag{3.13}$$

The added mass terms are given by

$$m_{11} = \frac{1}{4}\pi\rho a^2 \qquad \& \qquad m_{22} = \frac{1}{4}\pi\rho c^2(r) \tag{3.14}$$

The coefficient of drag is written as

$$C_D = 2C_t \sin^2\alpha \tag{3.15}$$

The angle of attack α is given by

$$\alpha = \tan^{-1}\left(\frac{v_y}{v_x}\right) \tag{3.16}$$

Where the velocity and the acceleration components are given as

$$v_x = -r\dot{\varphi}\,\mathrm{Sin}\,\eta \tag{3.17}$$

$$v_y = -r\dot{\varphi}\,\mathrm{Cos}\,\eta \tag{3.18}$$

$$a_x = \dot{v}_x \tag{3.19}$$

$$a_y = \dot{v}_y \tag{3.20}$$

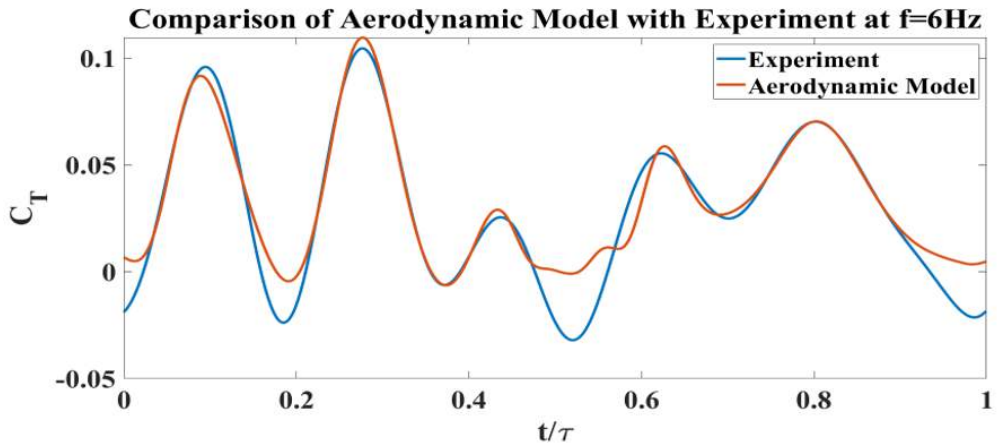

Figure 3.4: Comparison of aerodynamic model results with experiment at 6 Hz for 2wings

$\phi(t)$ is the flapping angle of the wing which is measured using the previously mentioned motion capture system. The pitching angle of the wing $\eta(r,t)$ is a function of r (spanwise location) and t (time). The pitching angle is modeled as a Fourier series in time since the motion is periodic, with spatially varying coefficients to account for wing flexibility.

$$\eta(r,t) = a_0(r) + a_1(r)\cos(2\pi ft) + b_1(r)\sin(2\pi ft) + a_2(r)\cos(4\pi ft) + b_2(r)\sin(4\pi ft) \tag{3.21}$$

Cubic polynomials are assumed for these coefficients as

$$a_i = A_{i1}r + A_{i2}r^2 + A_{i3}r^3 \tag{3.22}$$

$$b_i = B_{i1}r + B_{i2}r^2 + B_{i3}r^3 \tag{3.23}$$

After obtaining thrust per unit span T' from equation 3.9, it is then integrated over the span of the wing to determine total thrust generated by the FWMAV and then normalized to obtain the coefficient of thrust according to equation 3.24.

$$C_T(t) = \frac{T(t)}{\frac{1}{2}\rho V_{ref}^2 2S} \tag{3.24}$$

Upon defining the complete structure of the aerodynamic model, some unknown parameters must be specified. These include A_{01}, A_{02}, A_{03}, A_{11}, A_{12}, A_{13}, A_{21}, A_{22}, A_{23}, B_{11}, B_{12}, B_{13}, B_{21}, B_{22}, B_{23}, C_t & C_R. They are determined by formulating an optimization problem to minimize the error between the theoretical prediction and the experimental measurements of thrust time-variation over the cycle using the same kinematics. The results from this optimization problem are shown in Figure 3.4, which compares the optimized aerodynamic model with experimental measurements (the load cell test data, shown in Figure 2.8, are used in this case). As can be seen, the resulting coefficient of thrust from the model and from the experimental setup has a close match over the majority of the cycle. The measured perturbation velocity Δv can be applied to the model to study the effect of induced vibrations during the flapping cycle. To apply this perturbation, we need to modify the components v_x and v_y of each airfoil section to account for the contribution of Δv. The modified velocities are written as,

$$v_x = \Delta v \,\mathrm{Cos}\,\eta - r\dot{\varphi}\,\mathrm{Sin}\,\eta \tag{3.25}$$

$$v_y = -\Delta v \,\mathrm{Sin}\,\eta - r\dot{\varphi}\,\mathrm{Cos}\,\eta \tag{3.26}$$

3.2.2 Aerodynamic Model For Four-winged Robot

In the case of the four-winged robot, the aerodynamic model is almost the same as that of the two-winged robot with a few extensions to capture the effect of wing-wing interaction.

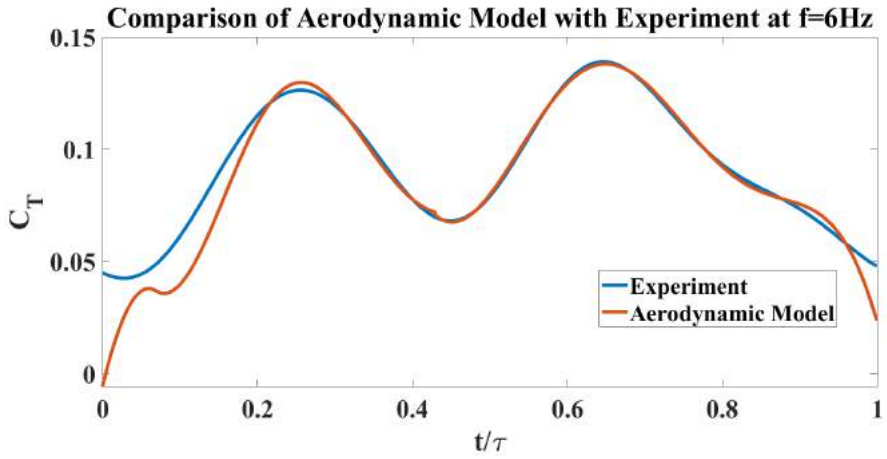

Figure 3.5: Comparison of aerodynamic model results with experiment at 6 Hz for 4wings

During the 'peel' motion, a suction is created between the wings, which sucks air from the ambient towards it and strengthens the leading edge vortex. Therefore, the generated circulation is modified in a way that empirically captures the change in the strength of the leading edge vortex.

$$\begin{aligned}\Gamma &= -\frac{1}{2}C_t c(r)|v|\,\mathrm{Sin}\,2\alpha + \frac{1}{2}C_F c^2(r)\dot{\eta}_{\text{fling}}\,, \quad \dot{\eta}_{\text{fling}} > 0 \\ \Gamma &= -\frac{1}{2}C_t c(r)|v|\,\mathrm{Sin}\,2\alpha + \frac{1}{2}C_R c^2(r)\dot{\eta}\end{aligned} \tag{3.27}$$

Also, the added mass term m_{22} is modified to take into account the 'peeled away' portion of the chord [5].

$$m_{22} = \frac{1}{4}\pi\rho c_{eff}^2(r,t) \tag{3.28}$$

The result of the match of the optimization formulation is shown in Figure 3.5. Similar to the previous case, the measured Δv can be applied to this model to analyze the effect of vibration during the flapping cycle.

Chapter 4

Results and Discussion

4.1 Averaged Thrust and Power Measurements

Figure 4.1 shows the variations of the measured thrust and aerodynamic power consumption with flapping frequency for all of the four FWMAV models described earlier. In order to extract the aerodynamic power from the total power measurements, we perform the test without the wings being installed to obtain an estimate for the mechanical power (used to drive the flapping wing mechanism); subtracting it from the total power, we managed to determine the aerodynamic power consumption. Note that the wing is extremely light in comparison to the flapping mechanism, as it is an EPP film (expanded polypropylene). So, it is expected that most of the inertial/mechanical power is spent in the mechanism, and hence, is captured by just removing the wing from the test. We show these measurements of the total power and mechanical/inertial power in the Appendix and the Aerodynamic power in Figure 4.1b.

The measured thrust and aerodynamic power consumption confirm the well-known behaviors of quadratic thrust-frequency variation and cubic power-frequency variation as shown in

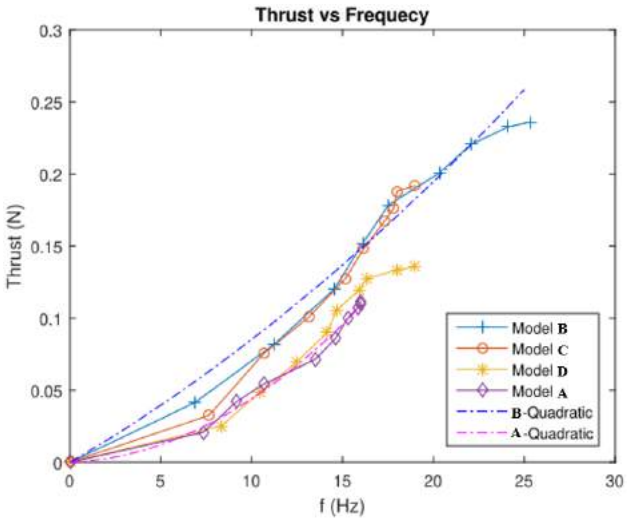

(a) Thrust vs Frequency

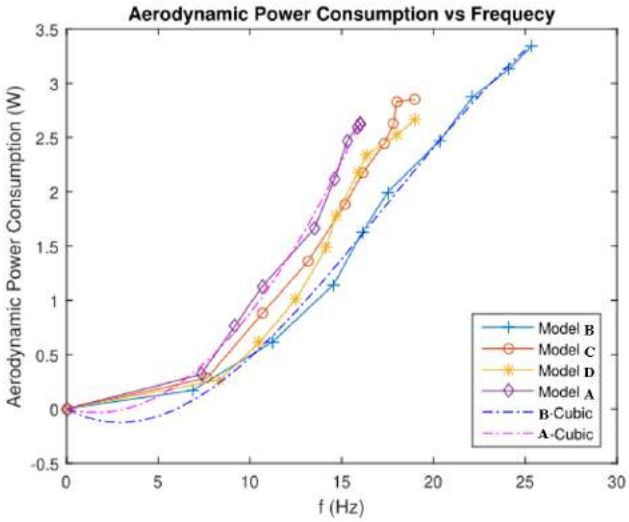

(b) Aerodynamic Power Consumption vs Frequency

Figure 4.1: Experimental measurements of the averaged thrust and aerodynamic power at different flapping frequencies

Equations 3.4 & 3.8. Moreover Table 4.1 shows the results of the regression equations calculated for the models A & D, which fit the experimental data almost perfectly. However, at high frequency span-wise elastic effects led to a decrease in the angle of attack; and the thrust generation deviates from quadratic behaviour, in accordance with the results of Percin et al. [58], as seen in figure 4.1a.

In contrast to the basic force and power analysis provided in section 3.1, ignoring wings interactions, figure 4.1a shows that the thrust of the four-wings model (model B) is significantly (almost double) higher than that of the two-wings model (model A) (this enhancement was observed to be 25% by Marden et al. [51], two times more by Nakata et a. [54] and Tay et al. [74], and 44.82% by Nguyen et al. [55]). Moreover, this significant additional thrust is generated in a considerably efficient way, for model B requires much less power than model A, making it almost twice efficient. Indeed, Figure 4.1 shows that model A (four wings that clap completely) produces the largest thrust among the four models, and even consumes the least aerodynamic power, making it the most efficient among the considered four models.

To assess whether the enhanced thrust and efficiency of the four-wings model (model B) beyond the two-wings model (model A) is due to clapping, we designed two different models (C, D) with different levels of wings interactions. Both models are driven by the same mechanism as model B. The only difference is that the wings of model C would not touch each other (i.e., do not clap) if they were rigid, since there is a 23° geometrical separation between the two wings on the same side. Yet, the wings come to touch each other due to flexibility, though do not clap completely as in model B due to the geometrical separation. In contrast, the model D has a structure separator that actually prevents the wings from exceeding the designed stroke angle by virtue of their flexibility, and hence precludes any possibility of clapping. The wings of this model (D) do not clap, but enjoy some aerodynamic interactions because they come close to each other. The comparison between these two models (C, D) is quite interesting because the two mechanisms are indeed identical, and the whole models

are almost identical (only one model has a structure separator, which would not be effective at all in the case of rigid wings). Despite this similarity, their aerodynamic performances are significantly different. As we can see in Figure 4.1a, model C produces almost 30% more thrust than model D when operating at the maximum frequency in the test. Moreover, their aerodynamic power consumption is quite similar, which implies that model C is significantly more efficient than model D despite the similarity. Indeed, this difference in aerodynamic performance is attributed to (partial) clapping.

Since the four models have slightly different parameters (e.g., stroke angle), we should study the normalized thrust and power. Therefore, we adopt the usual definition of thrust and power coefficients as follows:

$$C_T = \frac{T}{N\frac{1}{2}\rho V_{ref}^2 S} \tag{4.1}$$

$$C_P = \frac{P}{N\frac{1}{2}\rho V_{ref}^3 S} \tag{4.2}$$

We also define the efficiency as $\eta = \frac{C_T}{C_P}$, similar to a typical hovering machine (e.g., a helicopter). It must be emphasized that this typical definition of the efficiency for a hovering mode should not be interpreted as output power relative to an input power. Figure 4.2 shows the variations of the thrust C_T and power C_P coefficients with the flapping frequency as well the efficiency η. Figure 4.2a shows a clear trend of thrust-producing capability with clapping: C_T increases if more clapping is allowed, with the highest capability observed for model B, which allows full clapping. It is also noteworthy to mention that while model D prevents clapping, it has a higher thrust-producing capability than the two-wings model (A), which is attributed to wing-wing interactions: although the wings do not touch, they come close to each other.

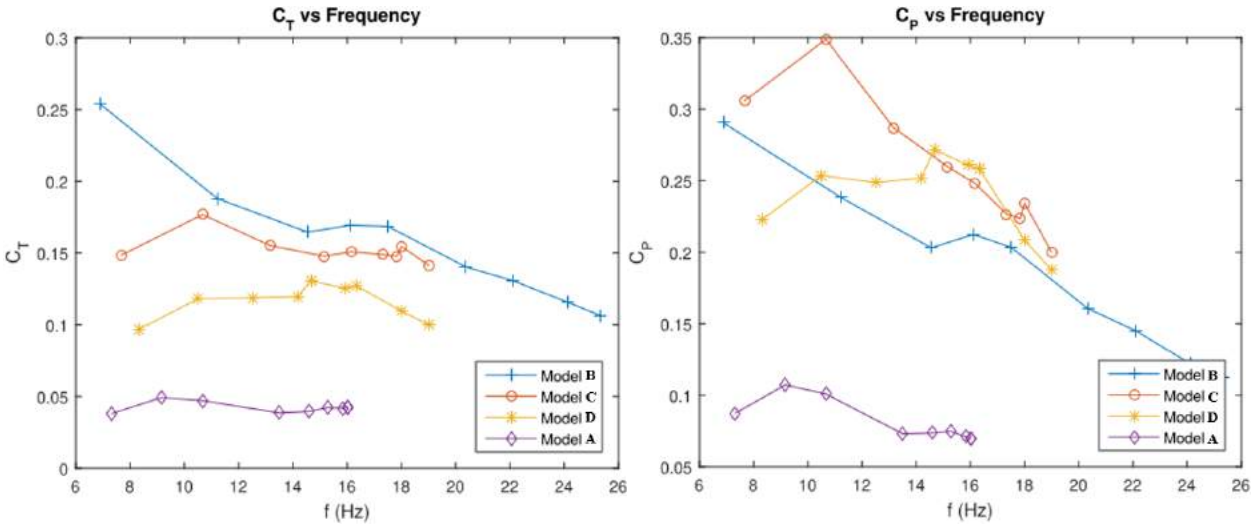

(a) C_T vs Frequency (b) C_P vs Frequency (only from the mechanism)

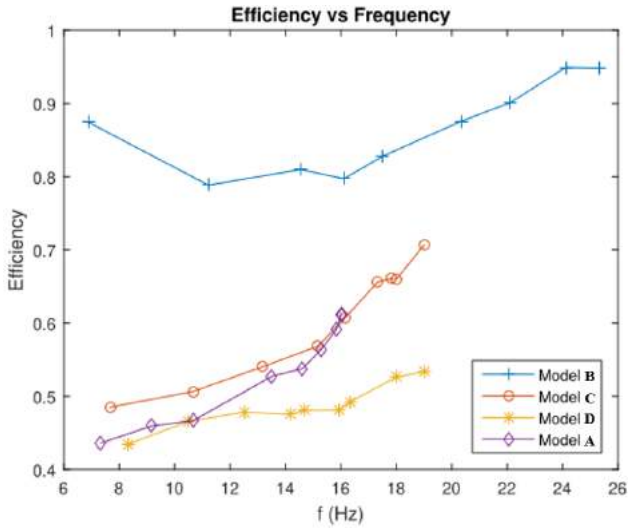

(c) Efficiency vs Frequency

Figure 4.2: Variations of the thrust and power coefficients C_T, C_P with frequency, as well as the efficiency $\eta = \frac{C_T}{C_P}$

Plot	**Model**	R^2	**Equation**
Thrust - Freq.	B	0.980	$T(f) = 0.007324f + 0.0001205f^2$
Thrust - Freq.	A	0.990	$T(f) = 0.0004643f + 0.000394f^2$
Aero. Cons. - Freq.	B	0.996	$P(f) = -0.09096f + 0.017111f^2 - 0.0003272f^3$
Aero. Cons. - Freq.	A	0.995	$P(f) = -0.04285f + 0.01327f^2 - 1.84 \times 10^{-5}f^3$

Table 4.1: Information about the Multiple Regressions of the Models

As for power consumption (efficiency), model B which allows full clapping is much more efficient than the rest, with model D being the least efficient. It is interesting to conclude that a FWMAV with two wings is around two times more efficient than a FWMAV with 4 wings that do not clap. Indeed, clapping can be a key to the success of these FWMAVs; if sufficiently exploited, it would provide quite an efficient means of producing a significantly larger thrust than the rest of configurations that do not enjoy the same level of clapping. These results support and provide more specific quantitative values to the previous studies in literature [59, 85].

It is interesting to observe that the thrust coefficient C_T of the two-wings model (A) is almost independent of the frequency, which follows theoretical prediction, though its C_P experiences some variations. On the other end, it is clear that the clapping thrust enhancement effects decrease as the frequency increases as observed by Percin et al. [58]; the less clapping effects, the less variations of C_T with frequency. It is also noteworthy to point to the maximum frequency of the system for a given drive motor. We can see how the length (stroke) of the trajectory of the wing during the cycle has an important effect on the maximum achievable frequency. Flapping with more wings that move a shorter stroke increase the maximum frequency. This result supports the recommendation of having four wings instead of two for future designs of MAV.

Finally, it is worth discussing the regression data of Table 4.1, which shows that both Model B

& A have a quadratic fit for the variation of the average thrust with the flapping frequency. Model B, fitting is given by $T(f) = A_4 f + B_4 f^2$; and Model A, fitting is $T(f) = A_2 f + B_2 f^2$, where $A_4 = 0.007324$, $B_4 = 0.0001205$, $A_2 = 0.0004643$ & $B_2 = 0.000394$. The coefficients of f^0 are zero because the models do not generate thrust when they are not flapping. Inspecting the coefficients of these fitting quadratic polynomials, it is interesting to observe that, $B_2 \sim 3B_4$ but, $A_4 \sim 15A_2$. Note that in the absence of wing-wing interactions, no linear dependence of average thrust on frequency is expected (only quadratic). Therefore, the fact that $B_2 > B_4$ is anticipated from the basic force analysis performed in Section 3.1; i.e., if the effects of wing-wing interactions are neglected, then the two-wings model (A) will produce larger thrust than the four-wings model (B). Hence, the observed stark difference in linear dependence to the advantage of model A is intuitively attributed to clapping. Moreover, normalizing the thrust force to obtain the thrust coefficient (i.e., dividing by f^2), the weak linear dependence term A_2 can be neglected, resulting in an almost constant thrust coefficient for model A. In contrast, the strong linear dependence term A_4 (due to clapping) leads to a thrust coefficient that decreases when f is increased: the coefficient of thrust takes the form $C_T = b_4 + \frac{a_4}{f}$, where a_4 & b_4 are constants. In other words, the thrust due to clapping is dominantly linear in frequency and hence, its coefficient decreases with increasing the frequency f as observed by Percin et al. [58].

It should be noted that while all four models have the same wing material, geometry, and kinematics (so the same aeroelastic effects) and although the only difference is the level of wing-wing interactions, the final results cannot be solely attributed to wing-wing interaction effects (e.g., clapping). These effects are enabled by specific aeroelastic properties of the wings, which are not studied in the current work, and should be studied in the future for a more comprehensive conclusion. For example, Ramananarivo et al. (2011) and Wu et al. (2011) observed how flexible wings store and release elastic energy every cycle which consequently increases their efficiency [59, 85]. Also Kim et al. (2013) showed how different aspect ratios and stroke angles of clapping motion have an effect on the generation of thrust

[43]. We also observed a similar effect: decreasing the size of the wing by half reduced the efficiency significantly at the same range of frequencies (almost 50%) [87].

The averaged thrust and power measurements, discussed above, imply that clapping indeed provides a significantly efficient thrust enhancement. It is interesting to study the underlying physics behind such a thrust enhancement mechanism, which is attempted in the next section using flow visualization.

4.2 Flow Visualization

The two-dimensional flow visualization experiment, discussed in section 2.4, was carried out at three different parallel sections along the span of the wing. These sections are shown schematically in Figure 4.3. For each of the four FWMAV models, a qualitative flow field at 35% and 50% of the wing span is shown in Figures 4.4 and 4.5. There is no free stream considered for these cases (i.e., pure hovering). The comparison was made for the different FWMAV models flapping at the same frequency. The flow was captured at six different instants (t/τ = 0, 0.2, 0.4, 0.5, 0.6 & 0.8) during the cycle, where $\tau = 1/f$ is the flapping period.

Figure 4.4 shows a clear difference between the flow fields of models B and A. Perhaps, the only similarity that can be observed is the presence of a leading-edge vortex (circumscribed by a red dashed circle). However, the figure shows that the lifting mechanisms in models B and A are fundamentally different. For model B, during the first half of the cycle where the wings are opening up (departing from each other or during 'fling'), the air is sucked in the open space between the wings, and when the wings are closing the air mass accumulated during the previous half-stroke is forcibly ejected downstream (in accordance with Sane's observation [60]). That is, the clapping model (B) enjoys a jet-effect thrusting mechanism—

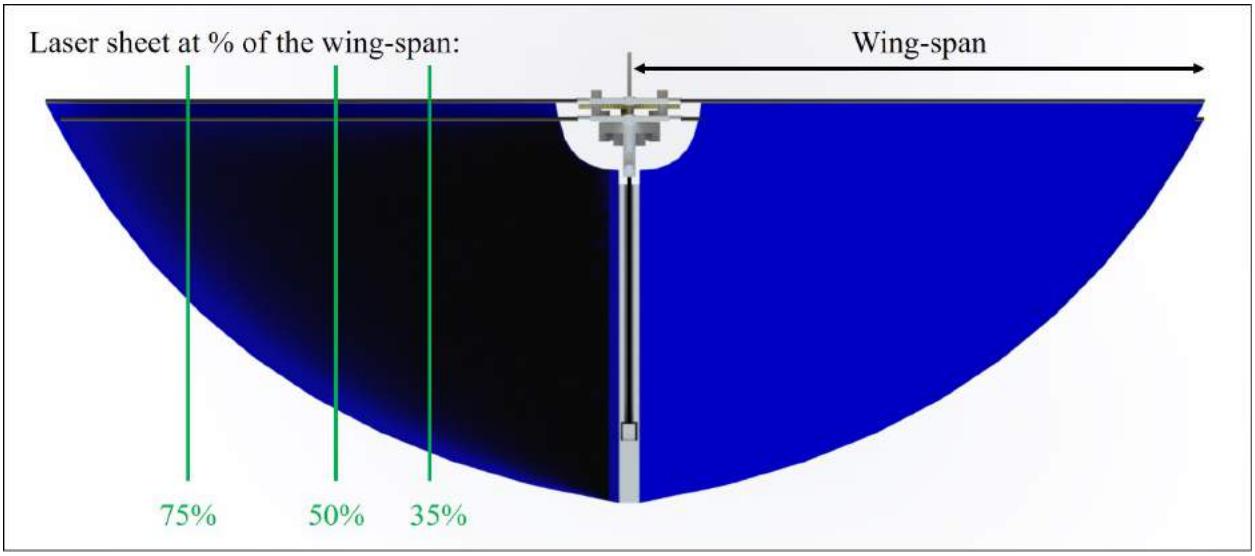

Figure 4.3: Schematic diagram showing the sections on the wing where the flow visualization experiment was carried out

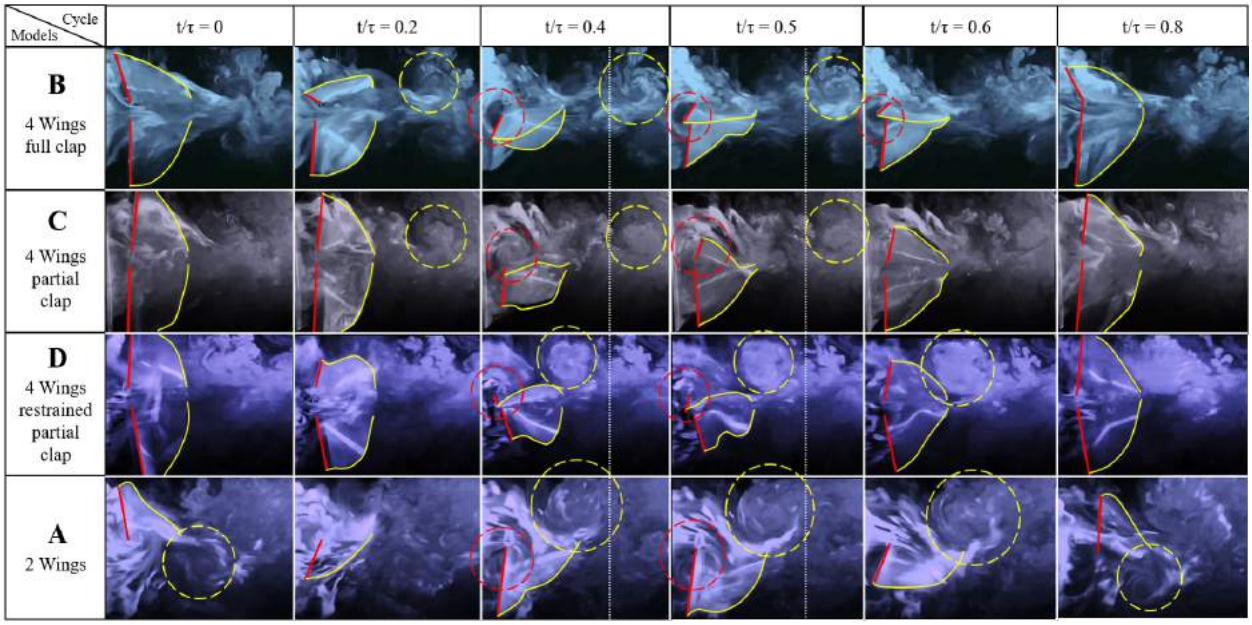

Figure 4.4: Flow Visualization of the four different models at 35% wingspan at different time instants ($t/\tau = 0$, 0.2, 0.4, 0.5, 0.6 & 0.8) during a cycle. The red bold line represents a wing leading edge (LE), the yellow bold line represents a wing trailing edge (TE), the red dashed line circumscribes a LE vortex and the yellow dashed line circumscribes a TE vortex.

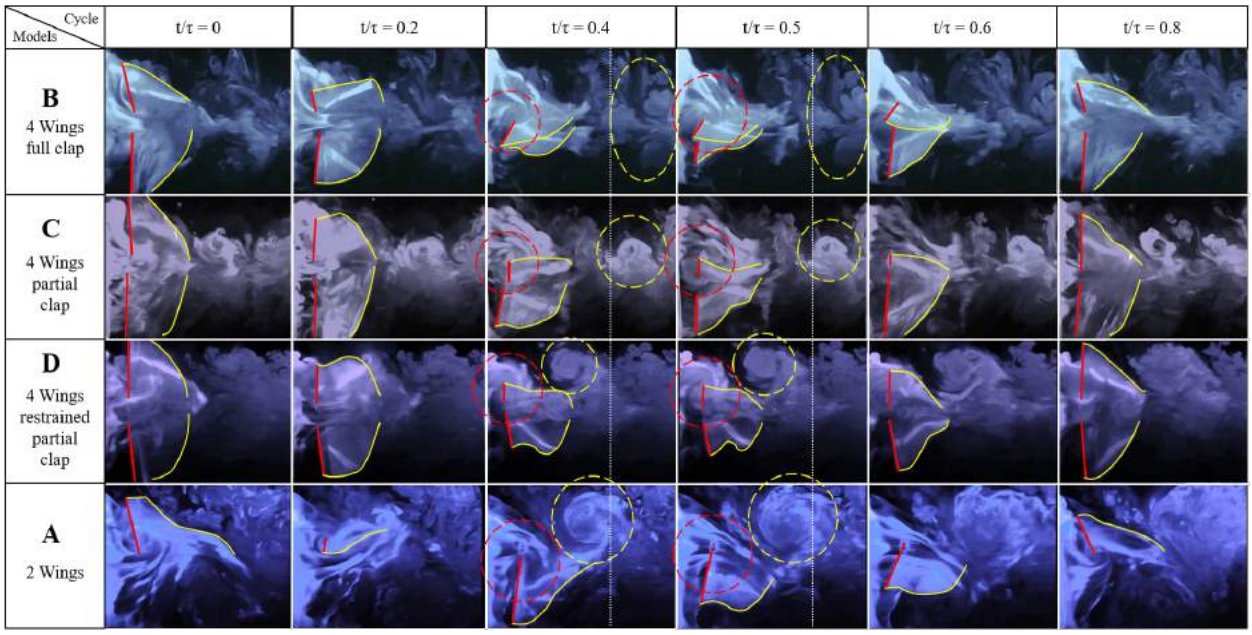

Figure 4.5: Flow Visualization of the four different models at 50% wingspan at different time instants ($t/\tau = 0$, 0.2, 0.4, 0.5, 0.6 & 0.8) during a cycle. The red bold line represents a wing leading edge (LE), the yellow bold line represents a wing trailing edge (TE), the red dashed line circumscribes a LE vortex and the yellow dashed line circumscribes a TE vortex.

we call it a *thrust burst*. Similar behavior is observed for Model C. In contrast, the two wings model (A) experiences a classical unsteady lifting mechanism: a trailing edge vortex (*starting vortex*) is shed whenever there is a change in the wing motion which, by virtue of conversation of circulation, leads to a change in the wing bound circulation (and consequently lift). This unsteady lifting mechanism has a transient response (Wagner's response [75]) due to such a trailing edge vortex (TEV) [60]; the closer the TEV to the wing, the smaller the unsteady lift in comparison to the steady value corresponding to the instantaneous wing motion. Therefore, insofar as the starting TEV is essential to the lift development because it dictates how much circulation around the wing, it is negatively impacting the transient lift development; the steady lift is not attained until the starting TEV is washed away. It is interesting to observe that the bursting jet in the clapping models (B, C) washes away the TEV [48]; it convects downstream much faster than in the case of model D, as shown in Figure 4.4 and the explanatory schematic in Figure 4.6. Also, in the four-wings model, there are two counter-rotating TEVs per side (one per wing). As traditionally known, these counter-

rotating vortices induce a downstream flow on each other [5], increasing their convective speed even more. As a result, the TEVs are always further away from the wings in B, and C than in A.

In the case of Model D, which has a separator that restrains clapping, Figure 4.4 shows that the air sucked in the opening phase is not strongly ejected in the form of a jet; the separator precludes the wings from closing and compressing the accumulated air mass between them to form a jet. Moreover, the figure also shows a TEV close to the trailing edge in this case. It can be recognized comparatively that the location of the TEV is furthest downstream for Models B & C but near the TE for Models D & A. This explains why models B & C have more thrust than models D & A. But, to understand the difference between models B & C, we need to look into the flow visualization at 50% wingspan which is shown in Figure 4.5.

The wing translational speed ($r\dot{\varphi}$) at 50% of the wingspan is larger than at 35%, leading to larger convective speeds and stronger effects. For example the bursting jets are clearer in Figure 4.5 than in Figure 4.4. Additionally, Figure 4.5 shows a leading edge vortex (LEV) in all models at the instances t/τ=0.4 & 0.5. In the non-clapping models D and A, the TEVs are close to trailing edge of the wings, with the TEV in model D being little further off from the trailing edge than in model A. For models B & C, the figure shows that the air is sucked in the early instances of the flapping cycles and is ejected downstream in the form of a jet as observed by Sane [60] and Jadhav [39]. Similar to the 35% flow, Figure 4.5 shows TEVs in the clapping models B, C further away from the wings than in the non-clapping models D, A. Finally, to better present the main flow features, a schematic in Figure 4.6 provides a qualitative comparison between the flow field of model B and that of model A.

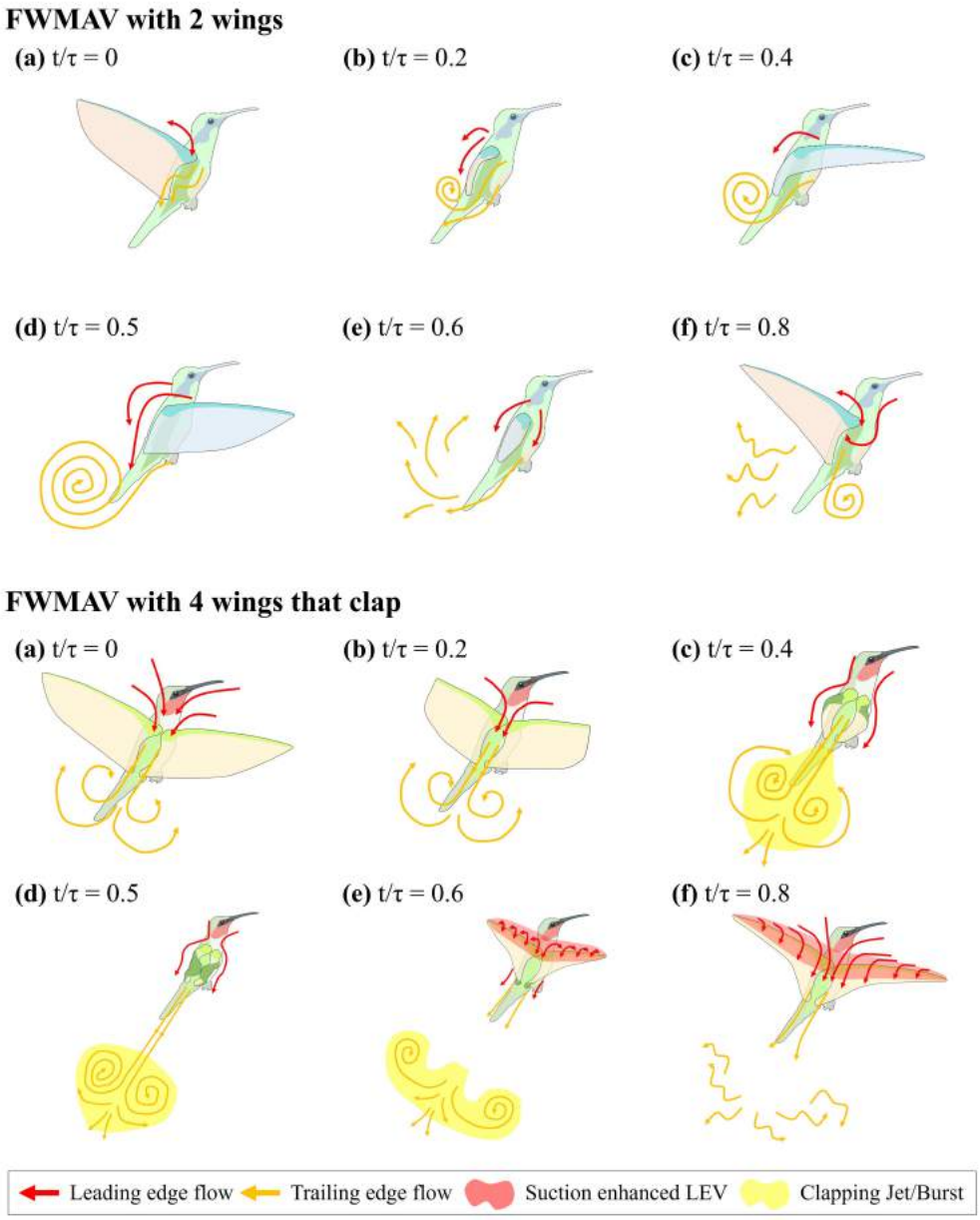

Figure 4.6: A schematic comparing the flow fields over a clapping four-wing FWMAV model and a non-clapping two-wing FWMAV model. (a) Stroke Start: no appreciable LE flow over the two-wing FWMAV model while the opening of the clapping wings creates a suction of the flow near the LE inside the space between the wings. (b) Middle of Downstroke: In both cases, the wings attain maximum translational speed and a TEV is formed. However, in the clapping case, there are two counter-rotating TEVs (one per each wing), which increases the downstream flow in the opening space between the wings. (c,d) End of Downstroke and Beginning of Upstroke: In both cases, the wings come to a stop and the TEVs become larger. In four-wings model, the wings are completely closed, ejecting downstream the sucked air between the wings in the form of a jet (air burst), which washes away the TEVs. (e) Middle of Upstroke: The TEVs are further away from wings in the clapping case whereas the TEV, in the two-wings model, has diffused.

4.3 Effects of Self-induced vibrations in BIFRs

In this section, we focus on the behavior of the flapping models at one flapping frequency ($6Hz$) to present a more complete picture than just inspecting thrust measurements. We scrutinize the flow field using flow visualization along with measuring the oscillatory motion of the body and feeding it into the presented aerodynamic model to gain some insight into the observed behaviors presented in Fig. 2.9. While the selected frequency should be representative of the considered regime, there is no guarantee that the explanations suggested in this section for the $6Hz$ case will hold exactly at other frequencies. However, we expect the pictures to be reasonably similar. The spanwise sections of 25% and 35% of the wing are chosen for flow visualization of model A. The sectional flapping velocities at the above mentioned locations are presented simultaneously with the perturbation velocity at a given point during the flapping cycle. For model B, 15% spanwise position is chosen and similar flow field images and velocities are investigated. Reference speed $V_{ref} = 2\pi f R\Phi$ is used to non-dimensionalize both the sectional velocity $r\dot{\phi}$ and the induced velocity Δv.

4.3.1 Effects of Self-Induced Vibrations on Model A

The images presented in Figure 4.7 primarily compare the flow fields produced by the flapping of Model A, at 25% spanwise location: 1^{st} row is without any perturbation and the 2^{nd} row is with the self-induced vibrations, shown in Figure 4.8. Both cases are compared at $6Hz$ flapping frequency (f). The row presents flow fields at a given time during the flapping period. The time parameter is denoted by t, whereas τ is the time period of flapping. In the figures (Fig. 4.7, 4.9 & 4.12) red shows the trailing edge outline and yellow is used for the leading edge. Figure 4.8 shows the comparison between non-dimensional flapping velocity and normalized perturbation velocity at 25% wingspan. The flapping cycle begins at $t/\tau = 0$, when the wing starts its down-stroke near the maximum angle of flapping. The

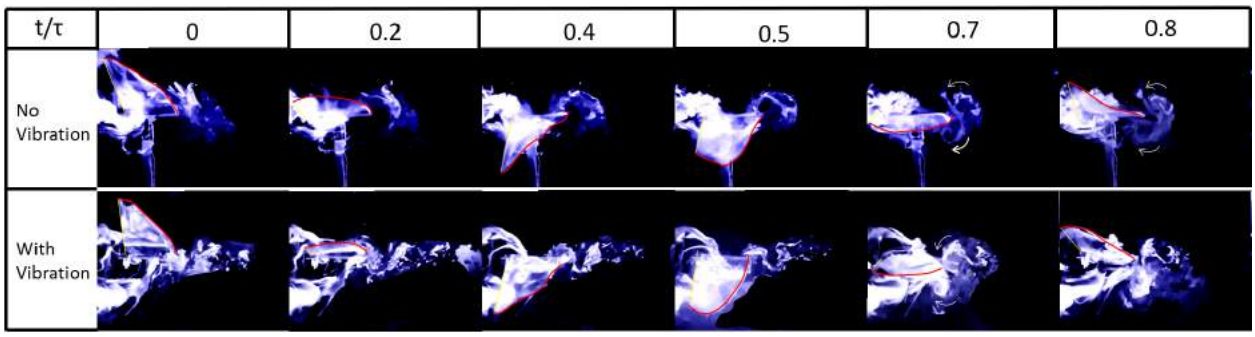

Figure 4.7: Flow visualization images from oscillatory test (with vibration) & fixed test (no vibration) at 25% spanwise location for Model A

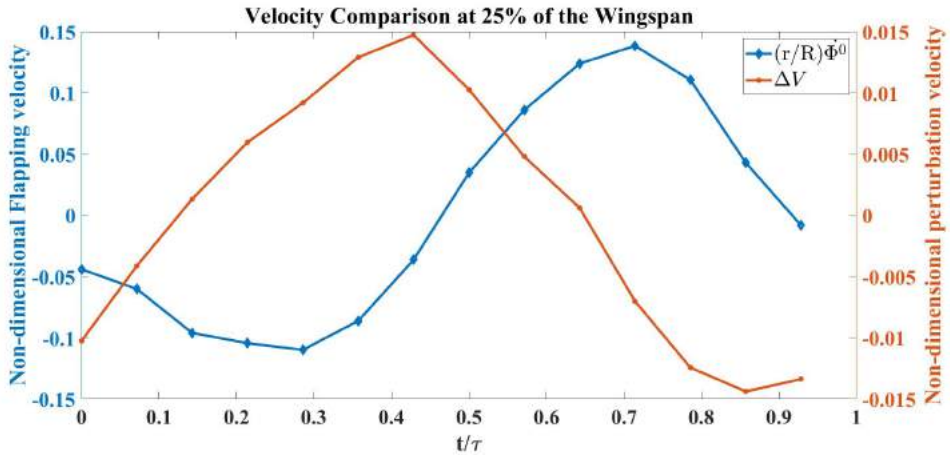

Figure 4.8: Normalized vibration and flapping velocity at 25% spanwise location for Model A

wing finishes down-stroke around $t/\tau = 0.5$ and ensues into upstroke.

Figure 4.7 shows a couple of vortices with opposite rotations near the TE for all the cases at the instant $t/\tau = 0.7$. The white arrows denote the direction of rotation of the vortices. A similar pair of vortices with opposite rotations can be seen in the no vibration case at $t/\tau = 0.8$ but they disappear in the case with vibration at a similar time instant. This pair of vortices at the trailing edge indicates the presence of a jet, which favors thrust generation. Figure 4.8 shows a negative perturbation velocity at $t/\tau = 0.7$ & 0.8, which implies a motion of the FWMAV model towards the jet due to the self-induced vibration. That is, the whole body is moving towards the counter-rotating vortices, which ebbs the jet effect and consequentially decreases the thrust in the oscillatory case. Similar physics can

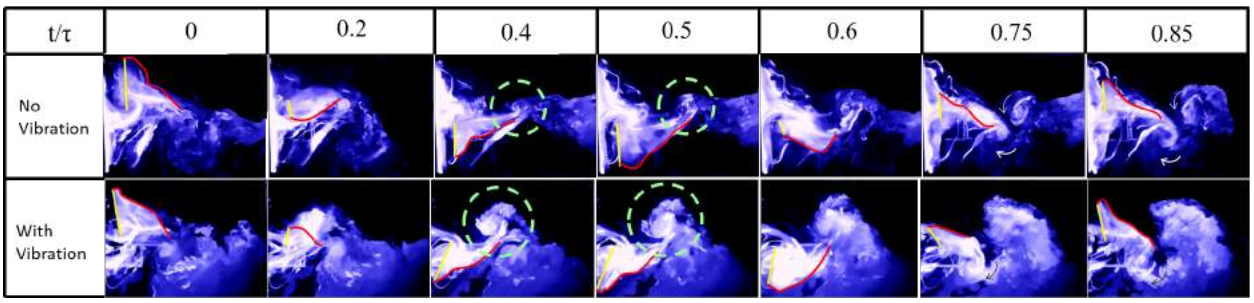

Figure 4.9: Flow visualization images from oscillatory test (with vibration) & fixed test (no vibration) at 35% spanwise location for Model A

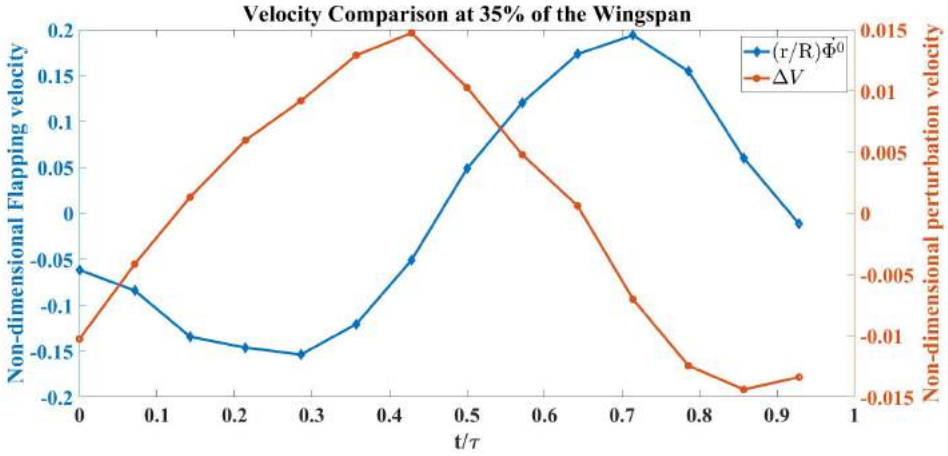

Figure 4.10: Normalized vibration and flapping velocity at 35% spanwise location for Model A

be observed at 35% of the wingspan, which is shown in Figure 4.9. Also, the normalized velocity comparison at 35% wingspan is shown in Figure 4.10.

Figure 4.11 shows the coefficient of thrust during a flapping cycle for model A, with and without self-induced vibration. C_{T_0} denotes the thrust coefficient based on the aerodynamic model discussed in section 3.2.1 [13] without any perturbation, while C_{T_v} is the coefficient of thrust when the measured vibration-induced perturbation is applied to the aerodynamic model. Figure 4.11 shows that approximately in between $t/\tau = 0.2$ & 0.7, C_{T_v} is greater than C_{T_0}. The reason can be seen in the flow visualization. Presented in Figure 4.9; that at $t/\tau =$ 0.4 & 0.5, in the no vibration case, there is a single trailing-edge vortex (TEV) attached to the trailing edge. By contrast in the oscillatory case, TEV is detached from the trailing edge.

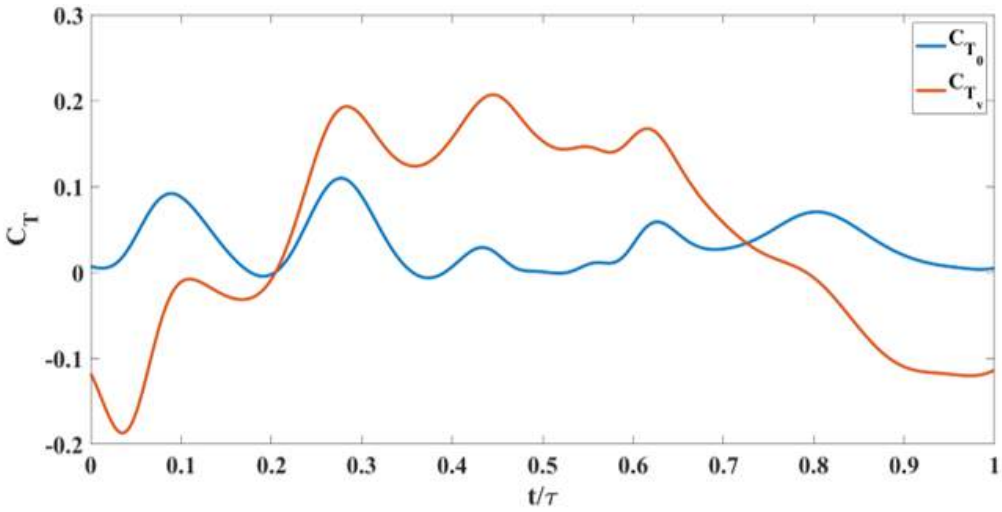

Figure 4.11: Thrust coefficient comparison for Model A with and without self-induced body vibration

The TEVs are shown in green dashed circles. Model A generates thrust using a conventional unsteady lifting mechanism: A TEV is shed whenever there is a change in the wing motion, which changes the wing-bound circulation as well as aerodynamic forces, because of the conservation of circulation. This mechanism has a transient response (Wagner's effect [75]). Due to this response, the closer the TEV is to the trailing edge, the smaller its strength is compared to the steady value. Figure 4.9 shows that at $t/\tau = 0.4$ & 0.5, ΔV is positive, which means that the whole body, due to the perturbation is moving to the left, leaving the TEV detached from the trailing edge. This results in an increase in C_{T_v} over a specific duration. But after $t/\tau = 0.7$, ΔV becomes negative and the whole body moves into the jet and loses thrust as discussed previously. This is reflected in Figure 4.11 that beyond $t/\tau > 0.7$, C_{T_v} becomes way less than C_{T_0}. In the end, the average C_{T_v} is less than the average C_{T_0} over the flapping cycle.

4.3.2 Effects of Self-Induced Vibrations on Model B

This sub-section is dedicated to analyzing the effect of self-induced vibration in the flow field of Model B at a 15% spanwise location. As mentioned by Balta et al. [10], the four-wings

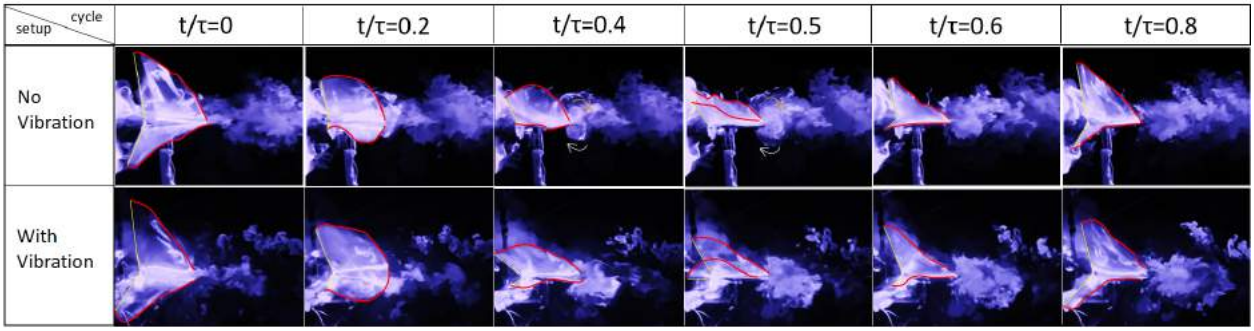

Figure 4.12: Flow visualization images from oscillatory test (with vibration) & fixed test (no vibration) at 15% spanwise location for Model B

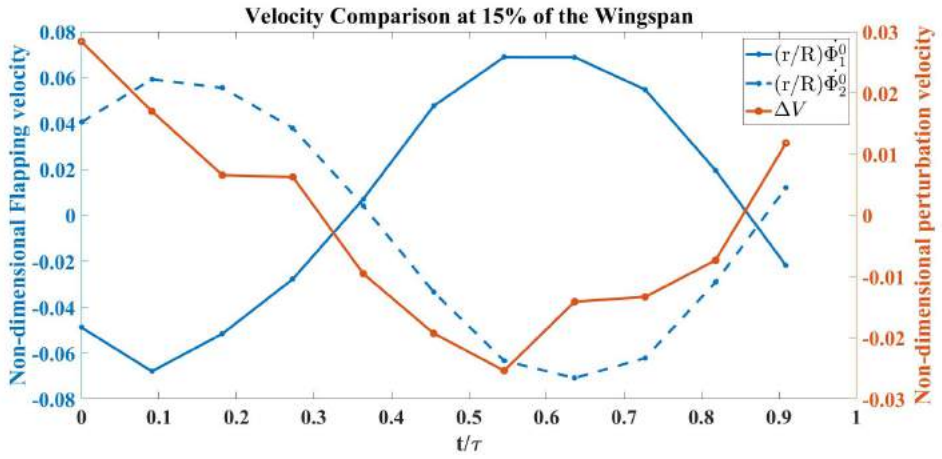

Figure 4.13: Normalized vibration and flapping velocity at 15% spanwise location for Model B

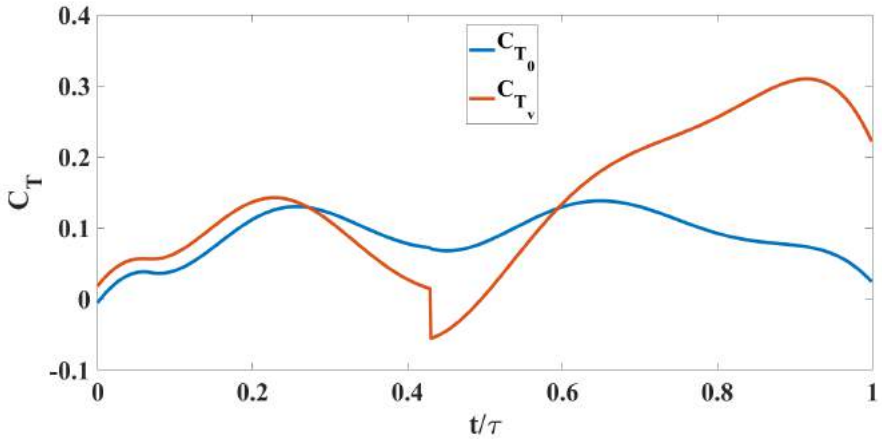

Figure 4.14: Thrust coefficient comparison for Model B with and without self-induced body vibration

mechanism generates thrust through the clap and peel mechanism. During the peel motion, it creates a suction between the wings, which intakes a significant amount of air. During the clap motion, it pushes the air downstream creating a 'jet burst'. Figure 4.12 shows that for the no vibration case, there are two counter-rotating vortices at $t/\tau = 0.4\,\&\,0.5$ which are indicative of the 'jet burst'. However, the figure does not show similar vortices in the oscillatory case at the same instant. Figure 4.13 shows that the perturbation velocity at $t/\tau = 0.4\,\&\,0.5$ is negative. This implies that the FWMAV is moving to the right during this time. This motion of the FWMAV towards the jet decreases the thrust, which can be seen in Figure 4.14. In this figure, C_{T_v} is the thrust coefficient resulting from the aerodynamic model presented in section 3.2.2 with the perturbation and C_{T_0} is the coefficient without the perturbation. We can see that C_{T_v} is less than C_{T_0} at $t/\tau = 0.4\,\&\,0.5$. In contrast, Figure 4.13 shows that ΔV is increasing during the ensuing period which means the flapping robot is moving away from the jet. The jet bursts and the self-induced perturbation takes the vortices away from the trailing edge. Thus it enhances the clapping effect; and the thrust increases significantly, as shown in Figure 4.14 after $t/\tau = 0.6$, compared to the case with no vibration. This enhanced clapping effect dominates the average C_{T_v} over the average C_{T_0}.

In table 4.2, the experimental and aerodynamic modeling values of $\frac{\overline{C_{T_v}} - \overline{C_{T_0}}}{\overline{C_{T_0}}}$ are presented in

percentage format for flapping frequency 6Hz.

	2 wings	4 wings
Experimental	-59.1%	64.4%
Aerodynamic Modeling	-24.4%	55.6%

Table 4.2: Percentage of average thrust coefficient change from ideal hovering to the case with perturbation, using aerodynamic modeling and experimental measurement

Finally, it may be prudent to emphasize that the obtained results and conclusions might not be directly extended to biological flyers or FWMAVs in free flight. The constraints in the pendulum setup may limit body motion, which, if allowed, could decrease the resulting aerodynamic loads (particularly for the two-winged model): A flapping wing experiences drag as it sweeps back and forth; this drag is transferred to the body, which causes the body to move opposite to the flapping wing. As such, the speed of the flapping wing with respect to the surrounding quiescent air is less (it is the flapping speed minus the body's backward speed), which results in smaller aerodynamic loads [73] [84]. This interaction is not captured in the pendulum setup because the stroke plane is almost parallel to the pendulum rod; the backward body motion (along the stroke plane) is restrained. From this discussion, it may be concluded that the measured thrust forces in the two-winged model, pendulum-setup case are higher than those in free flight, which does not contradict the general conclusion of the study: body oscillations reduce the averaged thrust in the two-winged model. In the four-winged model, however, the pendulum constraint may not be as restrictive because the instantaneous drag and inertial forces coming from each wing may cancel when transferred to the body (as they move in opposite directions).

4.4 Stability Assessment of the BIFR models

This section focuses on the the stability characteristics of the two BIFRs, at various flapping frequencies. Interestingly, we found that, in contrast to model A, the four-wing configuration (model B), which exploits clap-and-peel, attains natural (i.e., passive) stability beyond a certain flapping frequency. The natural stability of Model B is clearly demonstrated in figure 4.15, which presents the response of the BIFR system (in terms of γ, θ) as the flapping frequency progressively increases from an inert state at $t = 2$ seconds towards 18 Hz. During this excursion, the system traverses into instability, prior to crossing a critical frequency threshold. This pivotal frequency is ascertained to be about 18 Hz in the present work. Subsequently, at $t \sim 12$ figure 4.15 shows an evident transition to stability, providing a clear demonstration of the phenomenon of "vibrational stabilization" [68] [69]. No similar passive stabilization was observed with Model A at any achievable flapping frequency, which points to the positive effect of clap-and-peel on vibrational stabilization in flapping flight [72] [14].

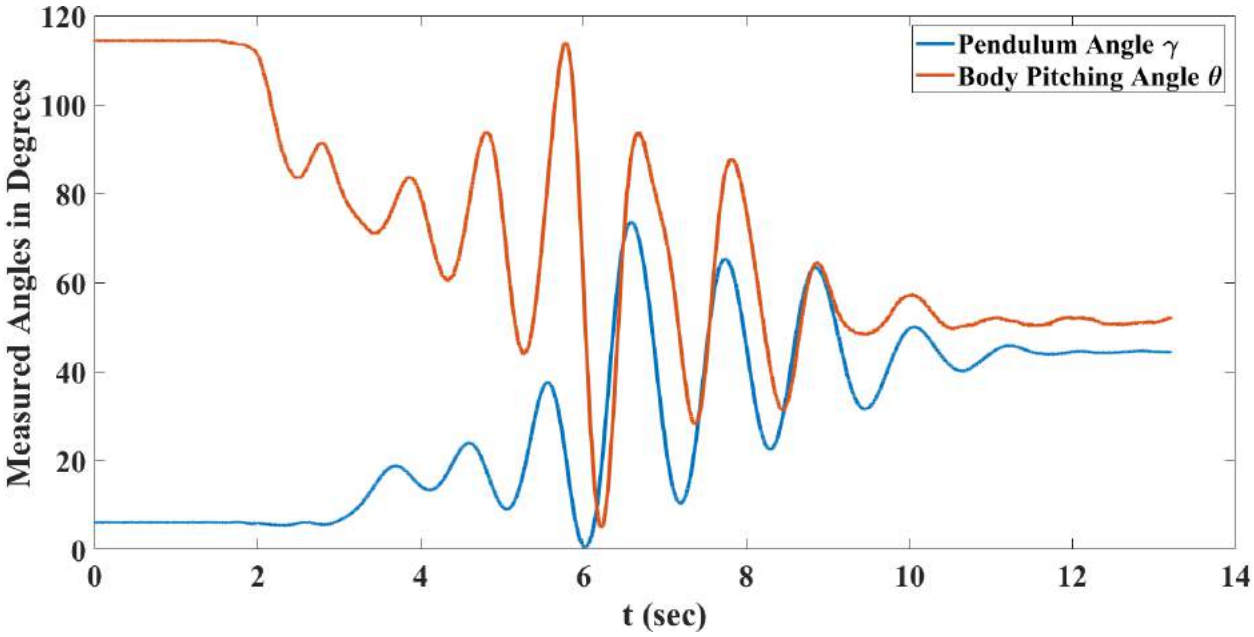

Figure 4.15: Response of Model B in terms of the pendulum angle γ and the body pitching angle θ as the flapping frequency increases from zero to beyond the critical frequency for

4.4.1 Natural Response of the Two BIFR Models

Figure 4.16 shows the response (in terms of γ, θ) of the two BIFR models at a flapping frequency of 14 Hz. The angular measurements encompassing γ and θ associated with flapping Model A are displayed in figure 4.16a. Both systems are found to be unstable at this frequency; both angles undergo oscillations with large (and slowly increasing) amplitudes.

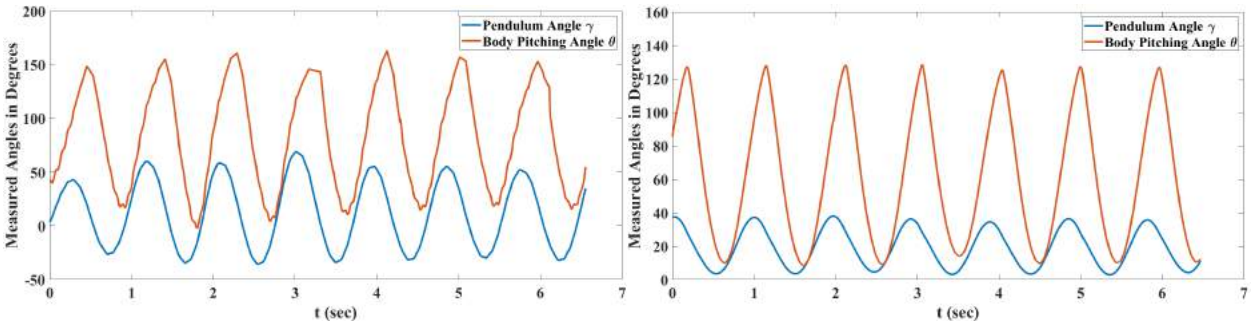

(a) Model A (b) Model B

Figure 4.16: System Response Subjected to different FWMAV models at Flapping Frequency 14 Hz

Figure 4.17 shows the response of the two BIFR models (A & B) at a flapping frequency of about 18 Hz. The response of Model B is naturally (i.e., passively) stabilized via vibrational stabilization, as shown in figure 4.17b. The system undergoes a stable periodic orbit (limit cycle) in which both angles undergo oscillations with very small amplitudes about a mean of $(\bar{\theta}, \bar{\gamma}) = (60^o, 30^o)$, In other words, this point is a hyperbolic stable equilibrium point of the averaged dynamics [50]. In contrast, the response of the angles θ and γ for Model A, shown in figure 4.17a, diverge in an unstable fashion. That is, the system possesses an unstable periodic orbit.

Evidently, this comparative observation underscores a compelling disparity between the two models under an identical flapping frequency of 18 Hz. This discernible discrepancy can be ascribed to the phenomenon known as the 'clapping effect'. Despite their same crank and rocker mechanism, wing geometry, and wing material, the pivotal variance lies in the aerodynamic response, particularly the presence of the 'clap-and-peel' mechanism within

Model B. The aerodynamic characteristics of the 'clapping effect', seem to be the driving factor behind the vibrational stabilization, observed in Model B in contrast to Model A.

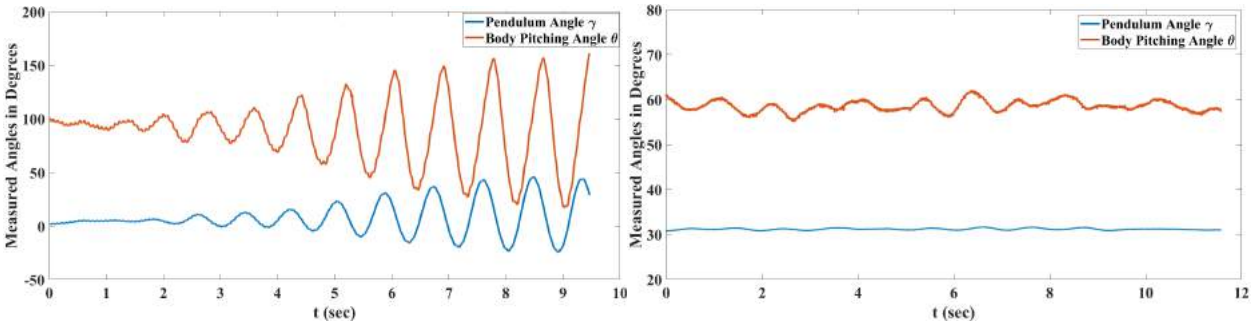

(a) Model A (b) Model B

Figure 4.17: System Response Subjected to different FWMAV models at Flapping Frequency 18 Hz

4.4.2 Recovery of Model B from Various Perturbations

Upon achieving vibrational stabilization at a flapping frequency of 18 Hz for Model B, the system is subjected to various perturbations to study its qualitative recovery from these perturbations. Figure 4.18 shows the responses of the system in terms of $\gamma(t)$ and $\theta(t)$ after the application of different perturbations (initial conditions).

Four different perturbations are considered. First, the flapping robot's body is set to a reduced angle ($\theta(0) < \bar{\theta}$) and subsequently released. The system restores its equilibrium in a bout 4 seconds, as shown in figure 4.18a. A similar relatively fast recovery is observed when Model B is subjected to the second type of perturbation: the system is released at an initial pendulum angle larger than the equilibrium value (i.e., $\gamma(0) > \bar{\gamma}$), as shown in figure 4.18c. Moreover, figure 4.18a indicates that a significant perturbation in the body angle may not cause a significant influence on the pendulum angle. In contrast, figure 4.18c shows that an initial disturbance in the pendulum angle γ may significantly impact the body pitching angle θ.

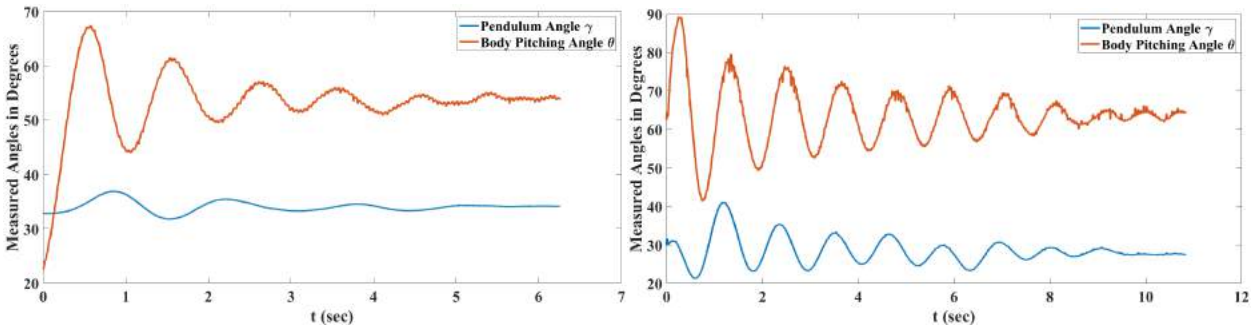

(a) System's Response Upon Release from Initial Body Angle

(b) System Behavior Following Body Impact Perturbation

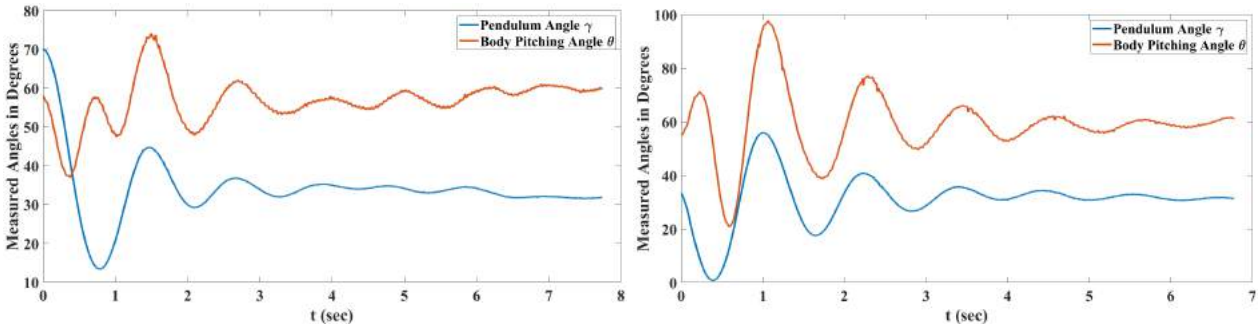

(c) System's Response Upon Release from Initial Pendulum Angle

(d) System Behavior Following Pendulum Impact Perturbation

Figure 4.18: Recovery of Model B from different perturbations.

The other two perturbations considered in this work are concerned with applying an initial velocity (i.e., an impact) to the pendulum and the body. Figure 4.18b shows the system's recovery from an initial body impact $\dot{\theta}(0) > 0$. It may be prudent to emphasize that these perturbations were applied manually, so uniformity was not the concern. The accompanied. Supplementary material provides video recordings of the system's recovery in each case presented in figure 4.18.

Finally, we would like to conclude by stating the main finding of this work: the stability of two almost-identical BIFRs, one with conventional flapping and another that exploits clapping, was tested over a range of flapping frequencies. The latter exhibited vibrational (passive/natural) stabilization above a certain frequency and the former did not (it was unstable at all frequencies). This finding implies that the clapping effect promotes vibrational stabilization in flapping flight. Combined with our previous efforts [32] that showed the

superiority of the clapping BIFR over the traditional one in terms of thrust generation [32] and handling self-induced vibrations [20], one may conclude that the clapping effect offers a very attractive design choice for bio-inspired flapping robots [24].

Chapter 5

Introduction to Quadflapper

The investigation on the clapping effect revealed its benefits in terms of aerodynamics and flight stability. Particularly, the clapping effect enjoys a passive thrust enhancement due to the wing-wing interaction. Moreover, it benefits from the self-induced vibration during hovering. The advantage of the clapping effect does not end in the field of aerodynamics. The natural stability exhibited by the four-winged BIFR can be attributed to the clapping effect. The next natural direction for the clapping effect is the application. Since the wing-wing interaction has these benefits, it is chosen for a novel design of a drone, named Quadflapper. Figure 5.1 shows the images of the Quadflapper drone. Four model B flapping robots are put together in a structure made from carbon fibres. The detail of this drone is documented in a Master's thesis [37]. The drone is controlled by a PID controller, placed at the geometric center of the structure. In order to avoid the cogging issue in the mechanism, we replaced the previous motor with an out-runner motor. This motor provides more torque than an in-runner motor. This replacement helped us overcome the fragility issue of this particular crank-rocker mechanism. The Quadflapper enjoyed a lot of successful flights. Now, the lab is moving toward manufacturing a better version of this novel drone.

5.1 Quadflapper and Quadcopter Comparison

Our observations indicate that the quadflapper demonstrates advantageous aerodynamic and stability characteristics attributed to the clapping effect. The quadflapper exhibits ease of maneuverability and provides robust control. To assess its efficacy, a comparative study with a quadcopter is imperative. Flight time serves as a fundamental parameter for quantification testing.

For the purpose of this study, both a quadflapper and a quadcopter were manufactured with identical weight and dimensions. As depicted in Figure 5.2, the structural frames of both drones were constructed to be $16cm \times 16cm$ diagonally, and their weights were standardized at about 73 grams. Both the quadflapper and quadcopter were equipped with BETAFPV BT2.0 450mAh 1S 30C HV Batteries and 18000KV-37mm brushless motors, maintaining consistency across these parameters.

The total flight time of the quadcopter was approximately 3 minutes, while the quadflapper exhibited a flight time of about 4 minutes under the same conditions. Both drones commenced the test with fully charged batteries. This empirical comparison underscores that, with all parameters held constant, the quadflapper surpasses the quadcopter by nearly 1 full minute in flight time.

It is noteworthy that the sole distinction between these two drones lies in their propulsion systems—one powered by copter blades and the other employing a clap-and-peel mechanism. In conclusion, our findings suggest that the clapping effect contributes to the development of a superior-performing drone, particularly in terms of extended flight time.

5.2 Quadflapper Beta

The first generation quadflapper or the quadflapper alpha exhibited the benefits of flapping flight. However, the crank-rocker mechanism utilized in the quadflapper design, is commercially purchased and left little to no room for development. In order to have room for research and development and have more control over the mechanism, a crank-rocker mechanism is developed in the lab. This new design gives more flexibility for wing material selection, wing shape optimization, clap-gap research, etc. Moreover, we can do research on the gear-box of the mechanism and make it more robust. A homemade flapping mechanism allows us to play with different diverse parameters. This flexibility may help us scale up or scale down the quadflapper in the near future. Moreover, by researching different parameters we can obtain the most efficient clap-and-peel mechanism. One of the parameters, clap-gap is investigated in this Master's thesis [37]. It has been concluded from the study that double clap with clap-gap of 15° is the most efficient among the all mechanisms tested for the study. As a result, it has been chosen for the Quadflapper Beta generation shown in figure 5.3.

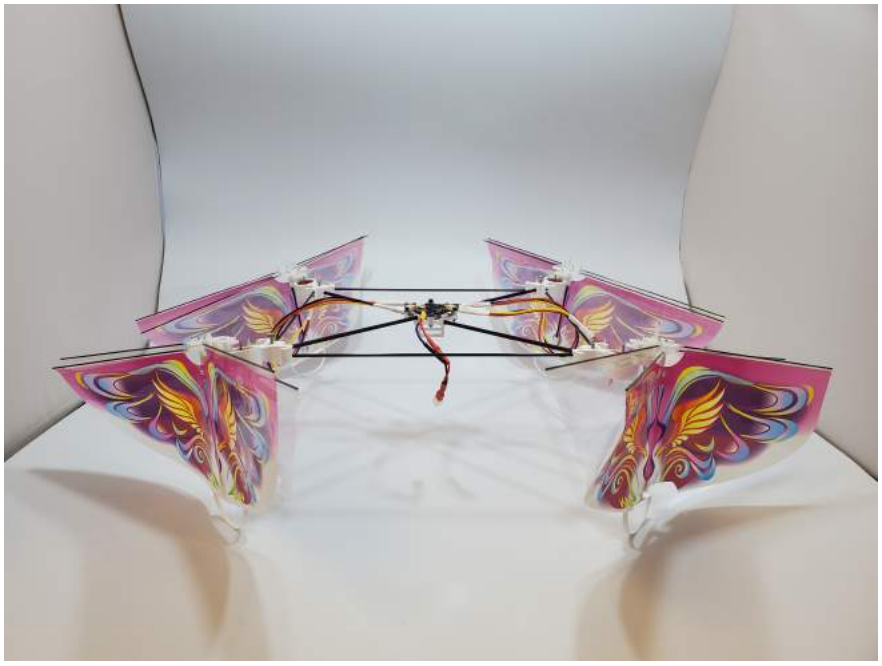

(a) Alpha Quadflapper Front View

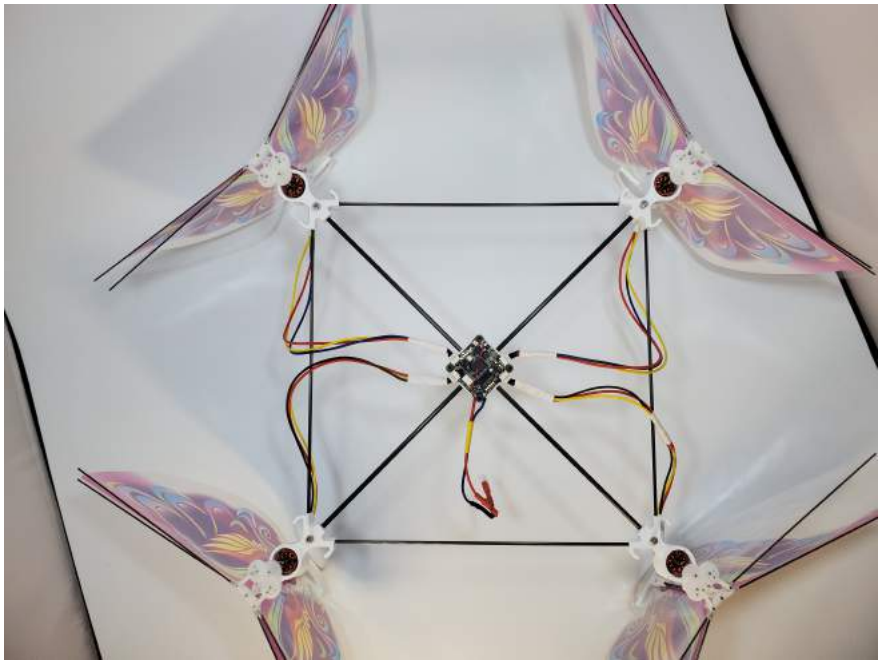

(b) Alpha Quadflapper Top View

Figure 5.1: Images of the Alpha Quadflapper

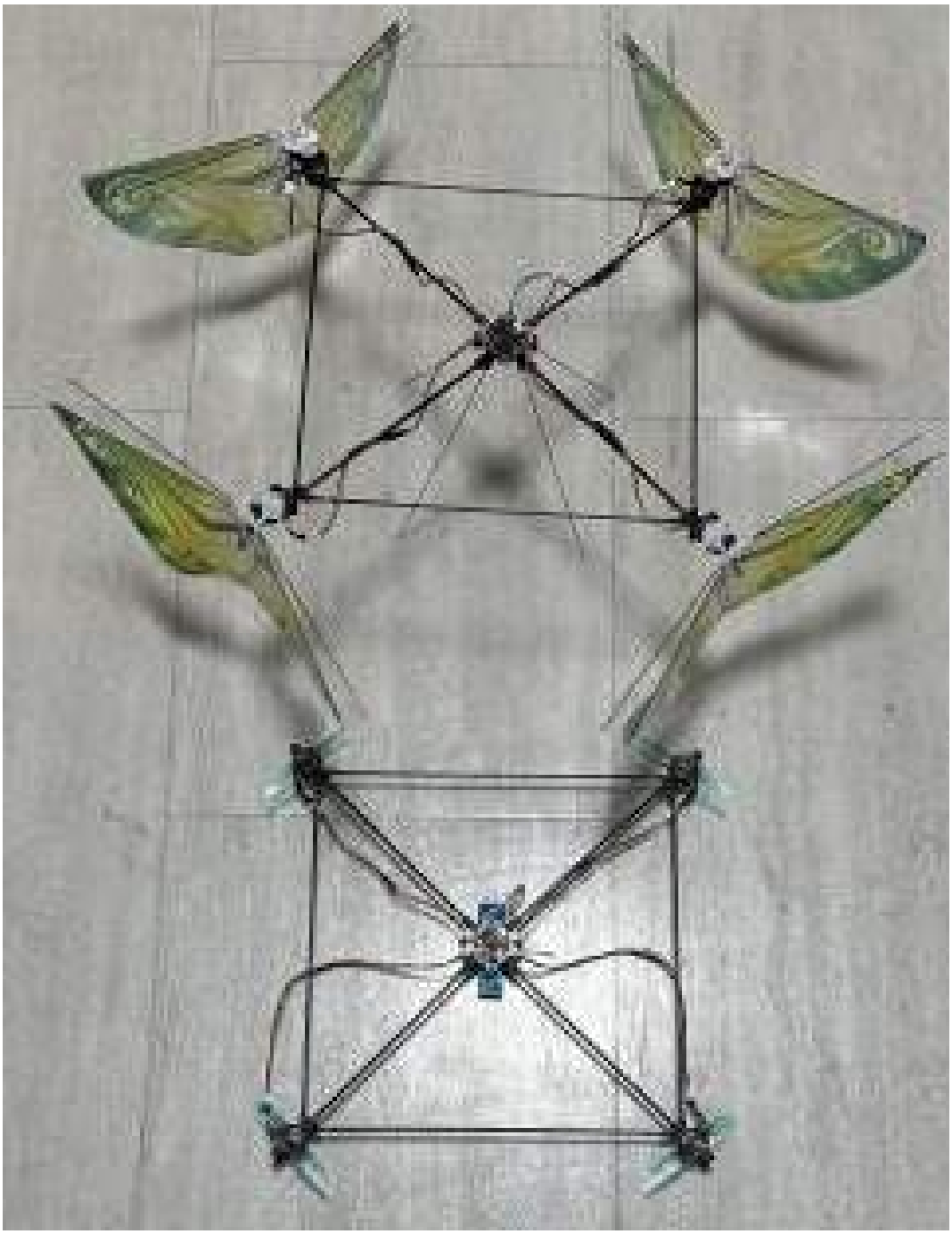

Figure 5.2: Quadflapper and Quadcopter

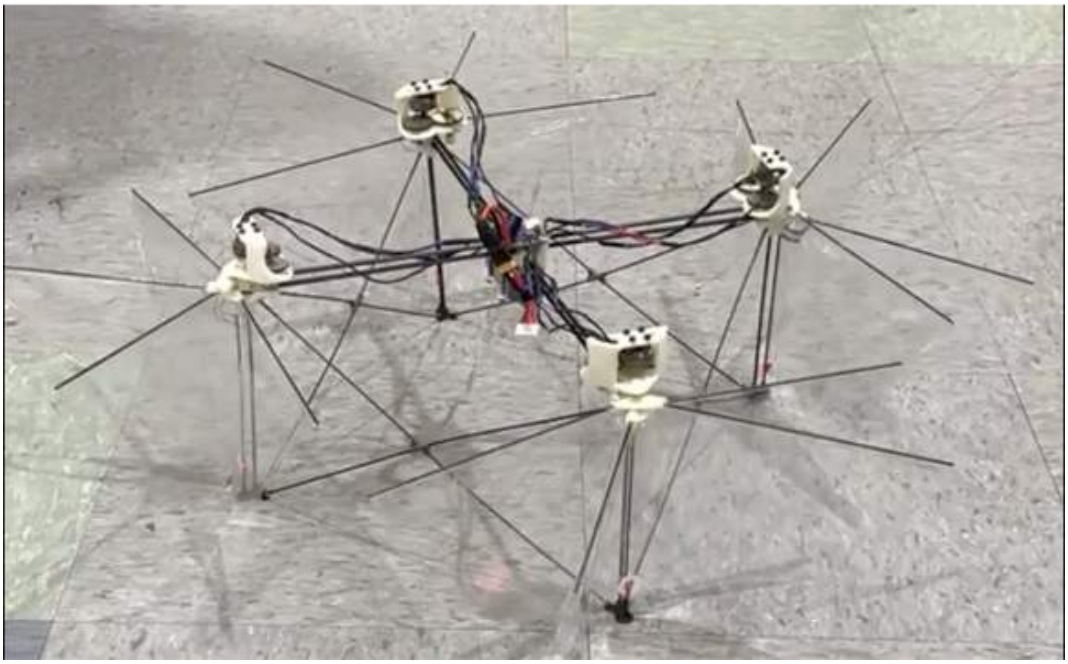

Figure 5.3: Quadflapper - Generation Beta

Chapter 6

Conclusion and Future Work

6.1 Conclusion

In this dissertation, we developed four models of bio-inspired flying robots with different levels of wing clapping: model (B) with four wings that completely clap, model (C) with four wings that partially clap, model (D) with four wings that do not clap but enjoy some wing-wing interactions, and model (A) with two wings (no clapping or wing-wing interactions). The aerodynamic performance of the four models was tested in terms of the averaged thrust and power consumption at various flapping frequencies. The four models are driven by the same flapping mechanism, which implies that each wing in the two-wings model sweeps double the stroke angle of a wing in the four-wings model. The study showed that the more clapping, the more thrust at the same frequency; the full clapping model (B) produces the largest thrust at a given flapping frequency. Moreover, it even consumes the lowest power, making it the most efficient among the four models. That is, an air vehicle with four wings that clap is significantly more efficient (almost double) and generates more thrust than the same air vehicle with only two wings sweeping double the stroke. Furthermore, from a

mechanical perspective, flapping along a shorter stroke allows operating at higher frequencies. In this regard, the four-wings model will be to operate at higher frequencies, hence generating more thrust than a two-wings model. To better understand the underlying physics behind this enhanced thrust capability due to clapping, we performed flow visualization around the flapping wings of the four models at different instants during the flapping cycle. The flow visualization study revealed that, during the opening phase of the wings in a clapping model, an air mass is sucked into the open area between the wings. As the wings close, this air mass is ejected in the form of a jet, creating an additional thrust. Moreover, this jet washes away the vortices from the trailing edges, diminishing their adverse transient effects on the wing lift development. In contrast, the two-wings model does not enjoy such a jet effect and its trailing edge vortices convect at a smaller speed. Hence, they stay in close proximity to the wing during some part of the cycle, negatively impacting its transient lift development. The presented flow visualization showed that the more clapping, the stronger the jet, and the further the trailing edge vortices are away from the wing.

This dissertation compares two cases of hovering flights. The first case is of an ideal hovering; there is no room for perturbation. The measurement in this case is carried out using the loadcell setup, which is also called the fixed test. The other case of hovering allows for concomitant self-induced vibration due to the oscillatory nature of the thrust force. A pendulum setup, which is also called the oscillatory test, is used to measure the average force in this case. This force measurement includes the effect of the self-induced vibration. These cases are studied using two different flapping wing robots: a two-winged robot or model A and a four-winged robot or model B. When these models are tested in the above-mentioned setups, it is observed that the fixed test measures more thrust than the oscillatory test for model A. The opposite behavior is observed for model B as shown in Figure 2.9. Model B exploits 'clap-and-peel' for generating thrust, whereas Model A uses the conventional flapping mechanism for the same. Due to the difference in the thrust generation mechanisms, the effect of the perturbation also differs between the two models.

Two well-known aerodynamic models ([5] [13]) for thrust generation are used to match the loadcell data by optimizing some unknown parameters. The perturbation velocity, measured using the motion capture system, is applied in the model to study the effect of the induced vibration during the flapping cycle. The perturbation is believed to have some effect on the flow field. To investigate how much impact the vibration has on the flow field, the flow visualization technique is used to look into it. The aerodynamic modeling and the flow visualization are done at the $6Hz$ flapping frequency.

Flow visualization revealed some interesting vortex interactions. In the case with no vibration, model A enjoys a certain jet effect near its trailing edge. The perturbation wanes its effect by moving the whole flapping robot into the jet. This decreases the overall thrust for model A in the oscillatory test. For model B the self-induced vibration enhances the thrust by moving the flapping robot away from the jet. This phenomenon enhances the clapping effect and consequently increases the overall thrust in the oscillatory test. The vortex interactions show how the self-induced vibration has an adverse effect on the thrust generation for a two-winged flapping robot. In contrast, the vibration enhances the effect on a four-winged flapping robot.

This dissertation studies the effect of clapping on the vibrational stabilization phenomenon in flapping flight. Since it is typically difficult to test this hypothesis in free flight, we designed an experimental setup that allows only two degrees of freedom for the bio-inspired flapping robots (BIFR) under study: body pitching and translation. The stability characteristics of two almost identical BIFR configurations are experimentally tested. The first configuration, referred to as Model A is a two-winged flapping robot that employs conventional flapping to generate aerodynamic forces. In contrast, the second configuration (Model B) is a four-winged robot, which exploits a clap-and-peel mechanism for aerodynamic force generation. At low flapping frequencies, both flapping robots exhibit unstable responses. However, a discernible departure emerges beyond a critical frequency: Model B, characterized by the

clap-and-peel mechanism, exhibits a noteworthy manifestation of vibrational stabilization, a property that eludes Model A. It is noteworthy that both models share uniform attributes: the crank and rocker mechanism, wing geometry, and material composition. Consequently, the pivotal demarcation is attributed to the aerodynamic effects of clapping, which is enjoyed by Model B but not by Model A. In this context, the vibrational stabilization observed in Model B is attributed to the distinctive 'clapping effect'.

We also tested the recovery of Model B towards its stable equilibrium after applying different perturbations. These perturbations include a release from angular positions different from equilibrium values and impact perturbations imparted to both the body's initial angular velocity and translational velocity. The vibrational stabilization of Model B was robust enough to sustain a variety of perturbations with significant magnitudes. However, the response characteristics during recovery (e.g., settling time) were different for different perturbations, which points to the underpinning nonlinear dynamics of the system. This study unveils an interesting outcome that may be important for the design of flapping-wing robots. The clapping effects promote natural/passive (vibrational) stabilization of flapping robots, which may relax the stringent requirements of the flight controller and its actuators, making flapping robots more feasible and easier to design. Wedded on previous results in the literature of clapping aerodynamics that showed positive effects on thrust generation and handling self-induced vibrations, clapping seems to be an attractive design choice.

The Quadflapper is able to demonstrate the concept of applying the clapping effect in a flight involving BIFRs. It can be improved further by optimizing the clapping effect with researching different parameters like clap gap, wing geometry, involvement of artificial ribs, etc. Our goal is to make a novel drone by utilizing the BIFRs that can be easily controllable, maneuverable, and which is able to carry a considerable amount of payload.

6.2 Future Work

This dissertation focuses on the aerodynamic and stability benefits of the clapping effect. The novel drone, quadflapper exploits these benefits in its flight. Although the quadflapper proves the concept of exploiting clapping effect in flight, the design is still very preliminary. There are a lot of parameters to work on and scaling of the quadflapper is still unexplored. Here are a few points to be considered for the future of the quadflapper.

- Any improvement of the quadflapper requires a theoretical foundation. The equation of motion of the quadflapper with six degrees of freedom, coupled with the aerodynamic modeling will provide more insight into the dynamics and stability of this novel drone design.

- An aerodynamic model is needed that captures the 'jet effect' due to the wing-wing interaction. This aerodynamic model can shed light on the phenomenon of vibrational stabilization from a theoretical point of view.

- The scaling of the quadflapper is still an unexplored realm of research. In my opinion, proper scaling of the quadflapper requires a few dimensionless parameters involving geometry, flapping frequency and the material properties of the wing. These dimensionless numbers can help in the scaling process without compromising the efficiency of the flapping mechanism.

- The new generation of Quadflapper, Beta provides us with a lot of opportunities for engineering research on the geometry of the wing and its materials. For different sizes and flapping frequency ranges, the most efficient mechanism may vary. The parameters of these mechanisms can be utilized for choosing non-dimensional numbers mentioned above.

- A combination of the quadflapper and the quadcopter can be manufactured. The load

carrying capacity of the quadcopter, maneuverability and the controllability of the quadflapper can be combined for a superior design of drone.

Bibliography

[1] Federal business opportunities, baa 06-06 proposer information pamphlet: Nano air vehicles (nav) program, 2005.

[2] Small powered flapping wings bird toys flying pigeon bird outdoor kids boys'toy, 2018.

[3] S. ALBEN. Wake-mediated synchronization and drafting in coupled flags. *Journal of Fluid Mechanics*, 641:489–496, 2009.

[4] B. Apffel, F. Novkoski, A. Eddi, and E. Fort. Floating under a levitating liquid. *Nature*, 585(7823):48–52, 2020.

[5] S. F. Armanini, J. Caetano, G. De Croon, C. De Visser, and M. Mulder. Quasi-steady aerodynamic model of clap-and-fling flapping mav and validation using free-flight data. *Bioinspiration & biomimetics*, 11(4):046002, 2016.

[6] S. F. Armanini, J. V. Caetano, C. C. de Visser, and G. de Croon. *Modelling wing wake and tail-wake interaction of a clap-and-peel flapping-wing MAV*, chapter 581. AIAA, 2017.

[7] S. F. Armanini, J. V. Caetano, C. C. de Visser, and G. de Croon. *Modelling wing wake and tail-wake interaction of a clap-and-peel flapping-wing MAV*. AIAA, 2017.

[8] N. Arora, A. Gupta, S. Sanghi, H. Aono, and W. Shyy. Lift-drag and flow structures associated with the "clap and fling" motion. *Physics of Fluids*, 26(7):071906, 2014.

[9] M. Balta, K. A. Ahmed, P. L. Wang, J. M. McCarthy, and H. E. Taha. Design and manufacturing of flapping wing mechanisms for micro air vehicles. In *58th AIAA/ASCE/AHS/ASC Structures, Structural Dynamics, and Materials Conference*, page 0509, 2017.

[10] M. Balta, D. Deb, and H. E. Taha. Flow visualization and force measurement of the clapping effect in bio-inspired flying robots. *Bioinspiration and Biomimetics*, 2021.

[11] Y. Bayiz, M. Ghanaatpishe, H. Fathy, and B. Cheng. Hovering efficiency comparison of rotary and flapping flight for rigid rectangular wings via dimensionless multi-objective optimization. *Bioinspiration & Biomimetics*, 13(4):046002, may 2018.

[12] G. J. Berman and Z. J. Wang. Energy-minimizing kinematics in hovering insect flight. *Journal of Fluid Mechanics*, 582:153–168, 2007.

[13] G. J. BERMAN and Z. J. WANG. Energy-minimizing kinematics in hovering insect flight. *Journal of Fluid Mechanics*, 582:153–168, 2007.

[14] F. Bullo. Averaging and vibrational control of mechanical systems. *SIAM Journal on Control and Optimization*, 41(2):542–562, 2002.

[15] C. Chen and T. Zhang. A review of design and fabrication of the bionic flapping wing micro air vehicles. *Micromachines*, 10(2):144, 2019.

[16] X. Cheng and M. Sun. Aerodynamic forces and flows of the full and partial clap-fling motions in insects. *Life and Enviroment Sciences*, 2017.

[17] G. De Croon, M. Perçin, B. Remes, R. Ruijsink, and C. De Wagter. The delfly. *Dordrecht: Springer Netherlands. doi*, 10:978–94, 2016.

[18] G. C. De Croon, M. Groen, C. De Wagter, B. Remes, R. Ruijsink, and B. W. van Oudheusden. Design, aerodynamics and autonomy of the delfly. *Bioinspiration & biomimetics*, 7(2):025003, 2012.

[19] D. Deb, K. Huang, and M. Fouda. *Effect of Self-Induced Body Vibrations on Thrust Generation in Bio-inspired Flying Robots*. 2022.

[20] D. Deb, K. Huang, A. Verma, M. Fouda, and H. E. Taha. Thrust enhancement and degradation mechanisms due to self-induced vibrations in bio-inspired flying robots. *Scientific Reports*, 13(1):18317, Oct 2023.

[21] D. Deb, P. Shetty, K. Poddar, and S. Kumar. Flow induced oscillation of two rigid rectangular plates in a side-by-side configuration. *Journal of Fluids and Structures*, 99:103133, 2020.

[22] K. K. Dhiman, Abhishek, and M. Kotharic. Flight dynamics and control of an unmanned helicopter with underslung double pendulum. *Journal of Aircraft*, 59(1):137–153, 2022.

[23] K. K. Dhiman, Abhishek, and M. Kotharic. Flight dynamics and control of an unmanned helicopter with underslung double pendulum. *Journal of Aircraft*, 59(1):137–153, 2022.

[24] M. H. Dickinson, F.-O. Lehmann, and S. P. Sane. Wing rotation and the aerodynamic basis of insect flight. *Science*, 284(5422):1954–1960, 1999.

[25] D. B. Doman, M. W. Oppenheimer, and D. O. Sigthorsson. Wingbeat shape modulation for flapping-wing micro-air-vehicle control during hover. *Journal of guidance, control, and dynamics*, 33(3):724–739, 2010.

[26] C. P. Ellington. The aerodynamics of hovering insect flight. iv. aerodynamic mechanisms. *Philosophical Transactions of the Royal Society of London. B, Biological Sciences*, 305(1122):79–113, 1984.

[27] C. P. Ellington and M. J. Lighthill. The aerodynamics of hovering insect flight. i. the quasi-steady analysis. *Biological Sciences*, 1984.

[28] C. P. Ellington and M. J. Lighthill. The aerodynamics of hovering insect flight. iv. aerodynamic mechanisms. *Philosophical Transactions of the Royal Society of London. B, Biological Sciences*, 305(1122), 1984.

[29] C. P. Ellington and M. J. Lighthill. The aerodynamics of hovering insect flight. iv. aerodynamic mechanisms. *Biological Sciences*, 1984.

[30] C. P. Ellington, C. Van Den Berg, A. P. Willmott, and A. L. Thomas. Leading-edge vortices in insect flight. *Nature*, 384(6610):626, 1996.

[31] C. P. Ellington, C. van den Berg, A. P. Willmott, and A. L. R. Thomas. Leading-edge vortices in insect flight. *Nature*, 384(630):1476–4687, 1996.

[32] A. M. Hassan and H. E. Taha. Combined averaging–shooting approach for the analysis of flapping flight dynamics. *Journal of Guidance, Control, and Dynamics*, 41(2):542–549, 2018.

[33] A. M. Hassan and H. E. Taha. Differential-geometric-control formulation of flapping flight multi-body dynamics. *Journal of Nonlinear Science*, 29(4):1379–1417, 2019.

[34] M. Hassanalian and A. Abdelkefi. Classifications, applications, and design challenges of drones: A review. *Progress in Aerospace Sciences*, 91:99–131, 2017.

[35] T. L. Hedrick and T. L. Daniel. Flight control in the hawkmoth Manduca sexta: the inverse problem of hovering. *Journal of Experimental Biology*, 209(16):3114–3130, 08 2006.

[36] Y.-W. Hu, L.-H. Feng, and J.-J. Wang. Flow-structure interactions of two tandem inverted flags in a water tunnel. *Physics of Fluids*, 32(8):087114, 2020.

[37] K. Huang. *Experimental Investigations of Bio-inspired Flight Mechanisms*. PhD thesis, University of California, Irvine, 2023.

[38] T. Hylton, C. Martin, R. Tun, and V. Castelli. The darpa nano air vehicle program. In *50th AIAA Aerospace Sciences Meeting Including the New Horizons Forum and Aerospace Exposition*, page 583, 2012.

[39] S. Jadhav, K. B. Lua, and W. Tay. Effect of clap-and-fling mechanism on force generation in flapping wing micro aerial vehicles. *Bioinspiration & biomimetics*, 14(3):036006, 2019.

[40] P. L. Kapitsa. Pendulum with vibrating suspension. *Usp. physical sciences*, 44(5):7–20, 1951.

[41] M. Keennon, K. Klingebiel, and H. Won. Development of the nano hummingbird: A tailless flapping wing micro air vehicle. In *50th AIAA aerospace sciences meeting including the new horizons forum and aerospace exposition*, page 588, 2012.

[42] M. Kiani, B. Davis, F. Pablo Quevedo, N. Cabezut, S. Hince, M. Balta, and H. E. Taha. A new bio-inspired flying concept: The quad-flapper. In *AIAA Scitech 2019 Forum*, page 1048, 2019.

[43] D. Kim, F. Hussain, and M. Gharib. Vortex dynamics of clapping plates. *Journal of Fluid Mechanics*, 714:5–23, 2013.

[44] H. Kim and D. Kim. Stability and coupled dynamics of three-dimensional dual inverted flags. *Journal of Fluids and Structures*, 84:18–35, 2019.

[45] D. Kolomenskiy, H. Moffatt, M. Farge, and K. Schneider. The lighthill–weis-fogh clap–fling–sweep mechanism revisited. *Journal of Fluid Mechanics*, 676:572–606, 2011.

[46] D. KOLOMENSKIY, H. K. MOFFATT, M. FARGE, and K. SCHNEIDER. The lighthill–weis-fogh clap–fling–sweep mechanism revisited. *Journal of Fluid Mechanics*, 676:572–606, 2011.

[47] F.-O. Lehmann and S. Pick. The aerodynamic benefit of wing–wing interaction depends on stroke trajectory in flapping insect wings. *Journal of experimental biology*, 210(8):1362–1377, 2007.

[48] F.-O. Lehmann, S. P. Sane, and M. Dickinson. The aerodynamic effects of wing–wing interaction in flapping insect wings. *Journal of Experimental Biology*, 208(16):3075–3092, 08 2005.

[49] M. J. Lighthill. On the weis-fogh mechanism of lift generation. *Journal of Fluid Mechanics*, 60(1):1–17, 1973.

[50] M. Maggia, S. A. Eisa, and H. E. Taha. On higher-order averaging of time-periodic systems: reconciliation of two averaging techniques. *Nonlinear Dynamics*, 99:813–836, 2020.

[51] J. H. Marden. Maximum lift production during takeoff in flying animals. *Journal of experimental Biology*, 130(1):235–258, 1987.

[52] N. Martin, C. Roh, S. Idrees, and M. Gharib. To flap or not to flap: comparison between flapping and clapping propulsions. *Journal of Fluid Mechanics*, 822:R5, 2017.

[53] L. A. Miller and C. S. Peskin. A computational fluid dynamics of 'clap and fling' in the smallest insects. *Journal of Experimental Biology*, 208(2):195–212, 2005.

[54] T. Nakata, H. Liu, Y. Tanaka, N. Nishihashi, X. Wang, and A. Sato. Aerodynamics of a bio-inspired flexible flapping-wing micro air vehicle. *Bioinspiration & biomimetics*, 6(4):045002, 2011.

[55] Q.-V. Nguyen, W. L. Chan, and M. Debiasi. Design, fabrication, and performance test of a hovering-based flapping-wing micro air vehicle capable of sustained and controlled flight. In *IMAV 2014: International Micro Air Vehicle Conference and Competition 2014, Delft, The Netherlands, August 12-15, 2014*. Delft University of Technology, 2014.

[56] M. W. Oppenheimer, D. B. Doman, and D. O. Sigthorsson. Dynamics and control of a biomimetic vehicle using biased wingbeat forcing functions. *Journal of guidance, control, and dynamics*, 34(1):204–217, 2011.

[57] M. Percin, Y. Hu, B. W. van Oudheusden, B. Remes, and F. Scarano. Wing flexibility effects in clap-and-fling. *International Journal of Micro Air Vehicles*, 3(4):217–227, 2011.

[58] M. Percin, B. W. van Oudheusden, G. C. H. E. D. Croon, and B. Remes. Force generation and wing deformation characteristics of a flapping-wing micro air vehicle 'delfly ii'in hovering flight. *Bioinspiration & biomimetics*, 11(3):036014, 2016.

[59] S. Ramananarivo, R. Godoy-Diana, and B. Thiria. Rather than resonance, flapping wing flyers may play on aerodynamics to improve performance. *Proceedings of the National Academy of Sciences*, 108(15):5964–5969, 2011.

[60] S. P. Sane. The aerodynamics of insect flight. *Journal of Experimental Biology*, 206(23):4191–4208, 12 2003.

[61] S. Sarkar, S. Chajjed, and A. Krishnan. Study of asymmetric hovering in flapping flight. *European Journal of Mechanics - B/Fluids*, 37:72–89, 2013.

[62] L. Schenato, D. Campolo, and S. Sastry. Controllability issues in flapping flight for biomimetic micro aerial vehicles (mavs). In *42nd IEEE International Conference on Decision and Control (IEEE Cat. No. 03CH37475)*, volume 6, pages 6441–6447. IEEE, 2003.

[63] Scientific Reports. *Appendix of Thrust Enhancement and Degradation Mechanisms Due to Self-Induced Vibrations in Bio-inspired Flying Robots*, 2023.

[64] A. Stephenson. Xx. on induced stability. *The London, Edinburgh, and Dublin Philosophical Magazine and Journal of Science*, 15(86):233–236, 1908.

[65] H. Taha, M. Kiani, and J. Navarro. Experimental demonstration of the vibrational stabilization phenomenon in bio-inspired flying robots. *IEEE Robotics and Automation Letters*, 3(2):643–647, 2017.

[66] H. Taha, M. Kiani, and J. Navarro. Experimental demonstration of the vibrational stabilization phenomenon in bio-inspired flying robots. *IEEE Robotics and Automation Letters*, 3(2):643–647, 2018.

[67] H. Taha, M. Kiani, and J. Navarro. Experimental demonstration of the vibrational stabilization phenomenon in bio-inspired flying robots. *IEEE Robotics and Automation Letters*, 3(2):643–647, 2018.

[68] H. E. Taha and M. Kiani. A new vibrational control system in nature: Flapping flight. In *AIAA Scitech 2019 Forum*, page 1417, 2019.

[69] H. E. Taha, M. Kiani, T. L. Hedrick, and J. S. Greeter. Vibrational control: A hidden stabilization mechanism in insect flight. *Science Robotics*, 5(46), 2020.

[70] H. E. Taha, A. H. Nayfeh, and M. R. Hajj. Saturation-based actuation for flapping mavs in hovering and forward flight. *Nonlinear Dynamics*, 73(1-2):1125–1138, 2013.

[71] H. E. Taha, A. H. Nayfeh, and M. R. Hajj. Effect of the aerodynamic-induced parametric excitation on the longitudinal stability of hovering mavs/insects. *Nonlinear Dynamics*, 78(4):2399–2408, 2014.

[72] H. E. Taha, S. Tahmasian, C. A. Woolsey, A. H. Nayfeh, and M. R. Hajj. The need for higher-order averaging in the stability analysis of hovering, flapping-wing flight. *Bioinspiration & biomimetics*, 10(1):016002, 2015.

[73] H. E. Taha, S. Tahmasian, C. A. Woolsey, A. H. Nayfeh, and M. R. Hajj. The need for higher-order averaging in the stability analysis of hovering, flapping-wing flight. *Bioinspiration & Biomimetics*, 10(1):016002, jan 2015.

[74] W. B. Tay, B. W. van Oudheusden, and H. Bijl. Numerical simulation of x-wing type biplane flapping wings in 3d using the immersed boundary method. *Bioinspiration & biomimetics*, 9(3):036001, 2014.

[75] H. Wagner. Über die entstehung des dynamischen auftriebes von tragflügeln. *ZAMM - Journal of Applied Mathematics and Mechanics / Zeitschrift für Angewandte Mathematik und Mechanik*, 5(1):17–35, 1925.

[76] J. M. Wakeling and C. P. Ellington. Dragonfly flight. i. gliding flight and steady-state aerodynamic forces. *Journal of Experimental Biology*, 200(3):543–556, 1997.

[77] T. WEIS-FOGH. Energetics of Hovering Flight in Hummingbirds and in Drosophila. *Journal of Experimental Biology*, 56(1):79–104, 02 1972.

[78] T. Weis-Fogh. Quick estimates of flight fitness in hovering animals, including novel mechanisms for lift production. *Journal of Experimental Biology*, 59(1):169–230, 1973.

[79] T. Weis-Fogh. Unusual mechanisms for the generation of lift in flying animals. *Scientific American*, 233(5):80–87, 1975.

[80] J. P. Whitney. *Design and performance of insect-scale flapping-wing vehicles*. PhD thesis, Harvard University, 2012.

[81] R. J. Wood. The first takeoff of a biologically inspired at-scale robotic insect. *IEEE Transactions on Robotics*, 24(2):341–347, 2008.

[82] R. J. Wood. The first takeoff of a biologically inspired at-scale robotic insect. *IEEE transactions on robotics*, 24(2):341–347, 2008.

[83] J. WU. *Unsteady aerodynamics of articulate lifting bodies*. 2012.

[84] J. H. Wu, Y. L. Zhang, and M. Sun. Hovering of model insects: simulation by coupling equations of motion with Navier–Stokes equations. *Journal of Experimental Biology*, 212(20):3313–3329, 10 2009.

[85] P. Wu, B. Stanford, E. Sällström, L. Ukeiley, and P. Ifju. Structural dynamics and aerodynamics measurements of biologically inspired flexible flapping wings. *Bioinspiration & biomimetics*, 6(1):016009, 2011.

[86] Z. Yan, H. E. Taha, and M. R. Hajj. Effects of aerodynamic modeling on the optimal wing kinematics for hovering mavs. *Aerospace Science and Technology*, 45:39–49, 2015.

[87] M. Zakaria. Experimental investigation of aerodynamic characteristics of a 4-winged flapping. Master's thesis, University of California, Irvine, 2021.

Appendix A

Appendix Title

A.1 Experimental Setup

A.1.1 Characterization of the Models

There are a couple points that can be explained further in order to understand better the models used in our research. The first is the type of mechanism used to generate the dynamics of the wings. The Crank Rocker mechanism is a four bar linkage that transforms a rotational motion into oscillatory. This mechanism uses 4 bars with different lengths, in where the shortest one (bar 2) rotates while the opposite linkage (bar 4) oscillates. The other two bars usually are longer and they are calculated to provide the required oscillatory motion. The equations that govern the relations between the bars are explained in previous publications of our research [9].

In Figure 2.1a, we can see the schematic of the crank rocker mechanism. It shows the bars from the crank rocker mechanism and how they are applied in to the passive mechanism. Figure 2.1b shows the crank rocker applied in Model A, which is the FWMAV that uses only

FWMAV	**Stroke Angle**	**Position of the Wing/s**	**r2/r1**	**r3/r1**	**r4/r1**
Model B	35°/wing	0° to ±35°	0.178	0.797	0.59
Models C & D	37°/wing	±11.5° to ±48.5°	0.162	0.726	0.54
Model A	60°/wing	-35° to 35°	0.178	0.92	0.36

Table A.1: Stroke Angle and Crank Rocker linkage ratios

2 wings to fly.

The mechanisms have been designed for an specific stroke angles, such that they provide the optimized dynamics for the wings. The way used to achieve these angles has been by adjusting the relation between the bars, using the equations that we mentioned previously. In general, these dynamics are obtained by selecting the right ratios, which are the result of defining the stroke angle of the wings and the minimum angle between the linkages. Then, the lengths of the linkages can be obtained by selecting the length of bar 1 and multiplying it with the ratios. The ratios we used in our mechanisms are shown in Table A.1.

The Crank Rocker ratios, the stroke angles and the position of the wing/s for each mechanism are in Figure A.1. The plots show both the stroke angle of the wings as well as the equilibrium position of them. These are the results of the motion of bar 4 plus the Extension (see Figure 2.1b). In Figure A.1a, which is Model A, the wing travels around 60° in where the equilibrium is almost in 0°. This helps the mechanism to be more balanced during the flight as the wings move more symmetrically with respect to the front and the back of the FWMAV. Model A has a similar performance but it divides the path by two, half per each wing (35° each wing). As we can see in Figure A.1c, despite each wing travels less, the combined stroke angle is 70°, which is 10 more° than Model A. Additionally, the equilibrium point is quite close to 0°, making this FWMAV also balanced.

On the other hand, there are the dynamics from Models C and D, which are shown in Figure A.1b. They are very similar to Model B, being the combined stroke angle of both wings

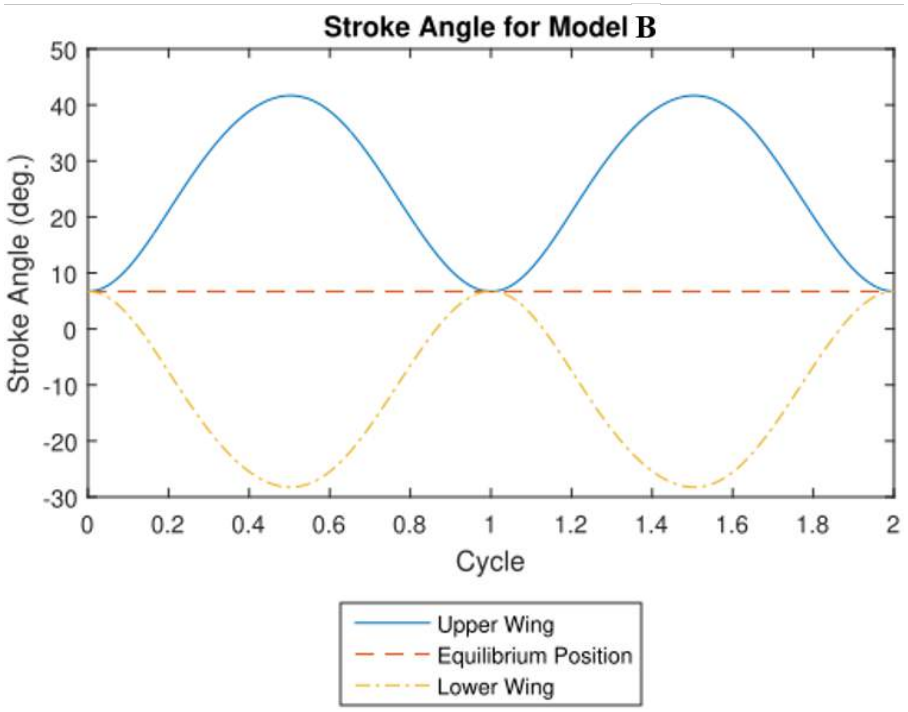

(a) Stroke Angle from the mechanism of Model B

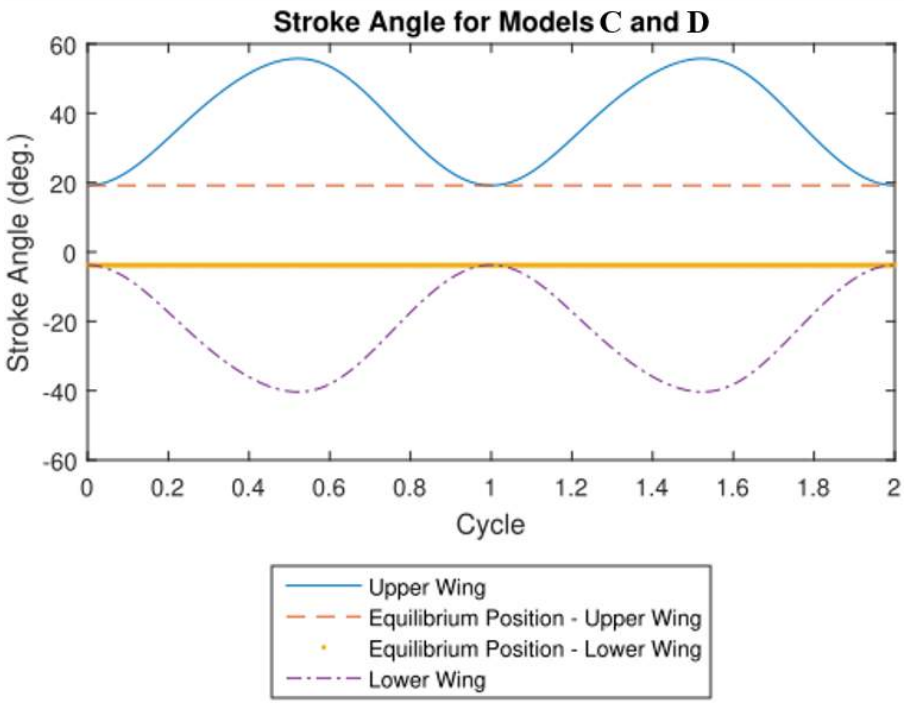

(b) Stroke Angle from the mechanism of Models C and D

Figure A.1: Stroke angles from crank rocker mechanism of each Model

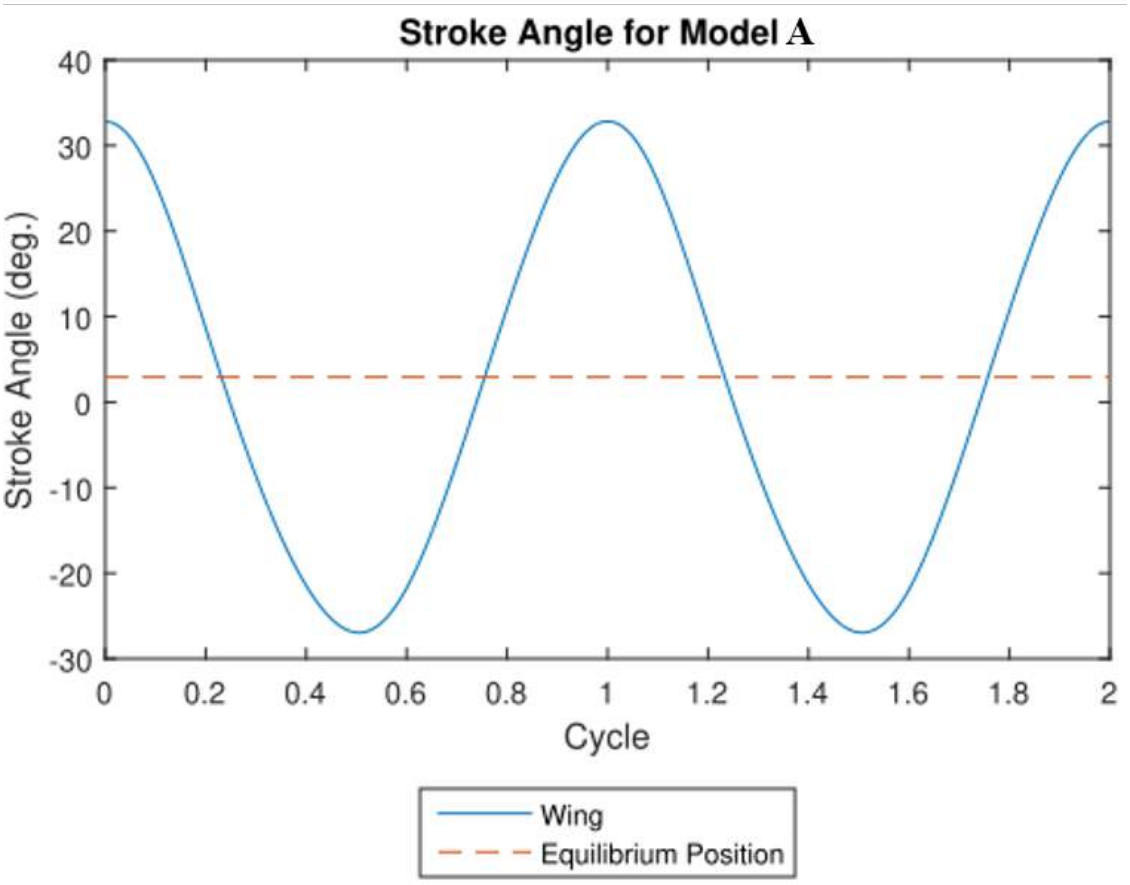

(c) Stroke Angle from the mechanism of Model A

Figure A.1: Stroke angles from the mechanisms of each Model (cont.)

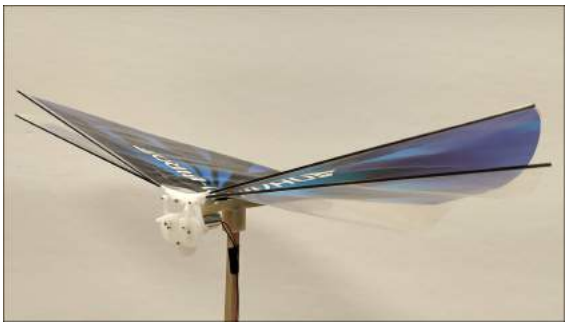

(a) Model B

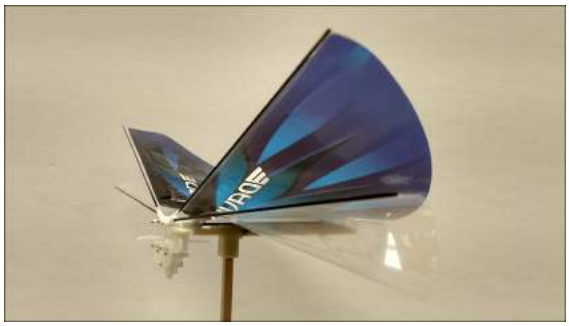

(b) Models C

(c) Model D

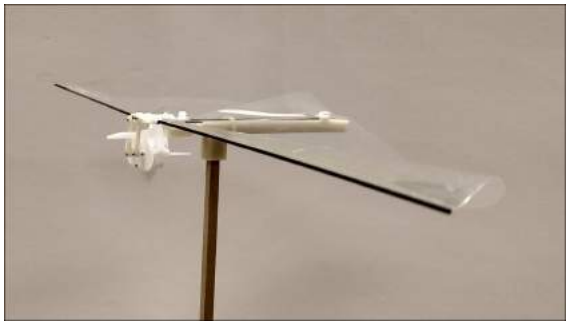

(d) Model A

Figure A.2: Top-Left Corner view of the Real Models used in the research

74°. However, in order to achieve that behavior without closing the wings completely, it was necessary to sacrifice part of the balance from the mechanism. As you can see, the average equilibrium would be around 8°, which makes the equilibrium from each wing at -2° and 20°. This creates some vibrations into the system, that luckily end up not affecting the consumption and performance. Of course, this would have brought critical issues if the model was flying alone instead of being attached to a pendulum. Even a little vibration would have compromised the stability of the system.

Finally, the FWMAVs are made out of injected plastic except for the pieces that were modified, that are 3D printed using a modified-ABS (see Figure A.2). Additionally, all FWMAVs are powered all using a 19.5 kV DC motor and have flexible and very light wings.

A.2 Averaged Thrust and Power Measurements

There are some additional plots from the "Average Thrust and Power Test" that can validate even more this study. First of all, there is the Total Power Consumption vs Frequency (see Figure A.3a), and the Mechanical Power Consumption vs Frequency (see Figure A.3a). Although these plots are introduced and explained in the paper, it is now visible how different is the magnitude of their units. That is the main reason why the Aerodynamical Power Consumption is very close the Total. Finally, the performance from each mechanism depends completely on its design and the manufacturing procedure. Consequently, Model B is the one that consumes less energy as its Crank Rocker configuration and manufacturing procedure (outside purchase) are the most optimal.

On the other hand, the relation between the voltage and the frequency has been crucial to control the models. Figure A.3c shows this relation, in which the voltage is proportional to the frequency. The only difference is the maximum voltage per model, which is directly related to the maximum thrust that can be generated by that model.

Table 4.1 shows the results of the regression equations calculated for models B and A, which fit the experimental data almost perfectly.

A.3 Flow Visualization

Figures A.4 compare the flow field for all the FWMAVs at 75% of the wing span. It can be seen that apart from Model A, everywhere the flow is turbulent in all the phases. At this section, the velocity of flapping is much higher, and probably that is why the vortices dissipate much faster compared to the sections mentioned before.

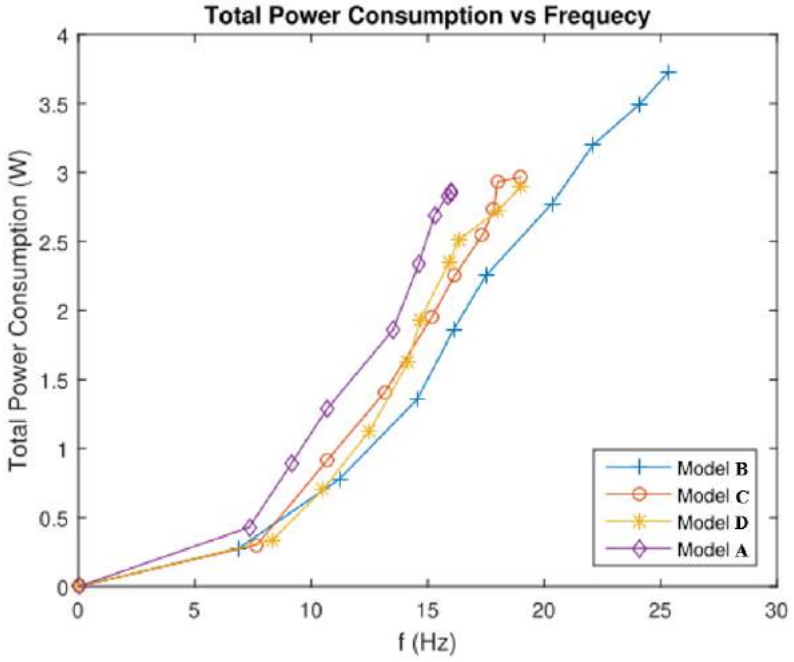

(a) Total Power Consumption vs Frequency

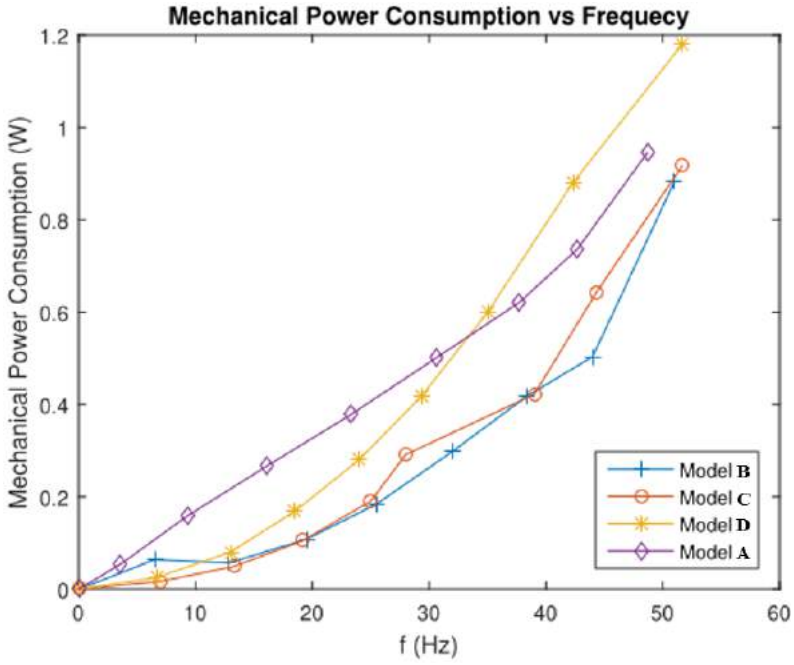

(b) Mechanical Power Consumption vs Frequency

Figure A.3: Additional Results from the Average Thrust and Power Test.

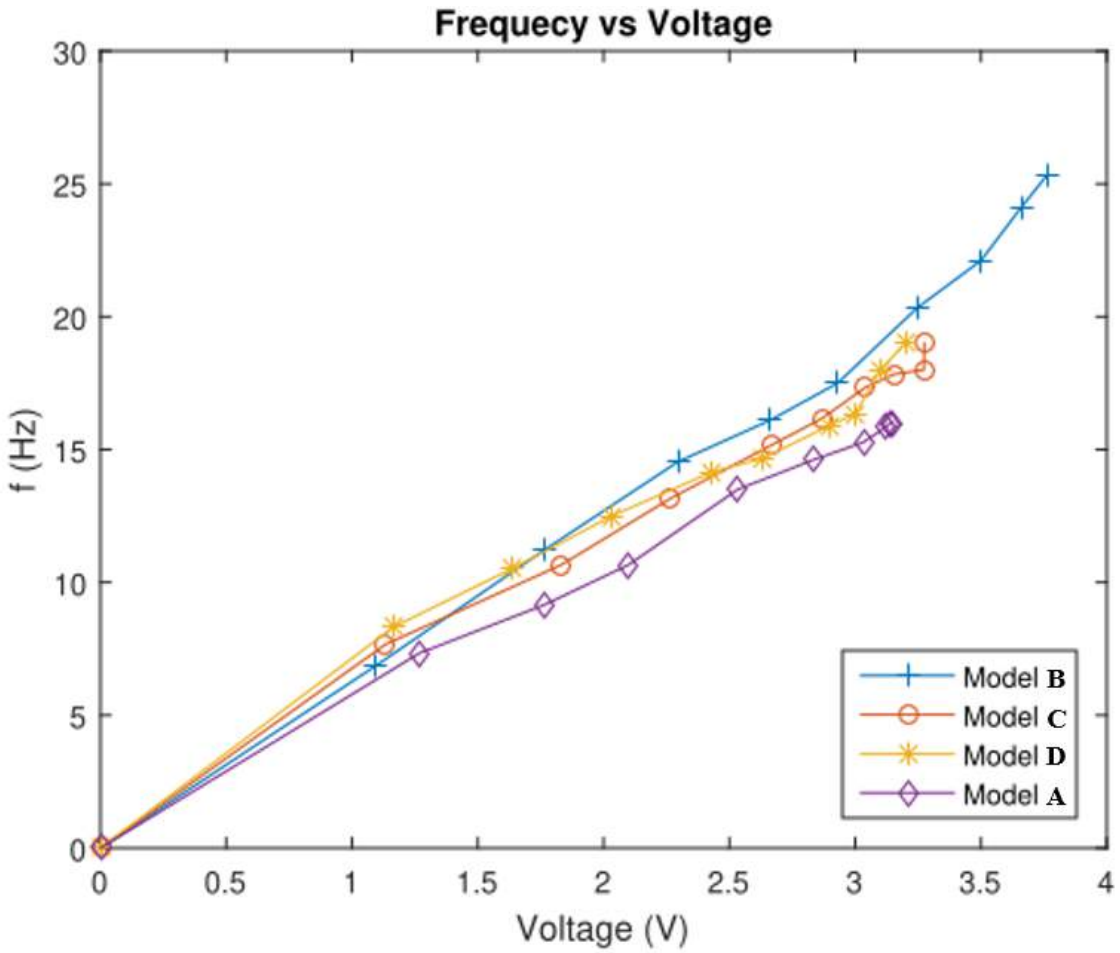

(c) Frequency vs Voltage

Figure A.3: Additional Results from the Average Thrust and Power Test. (cont.)

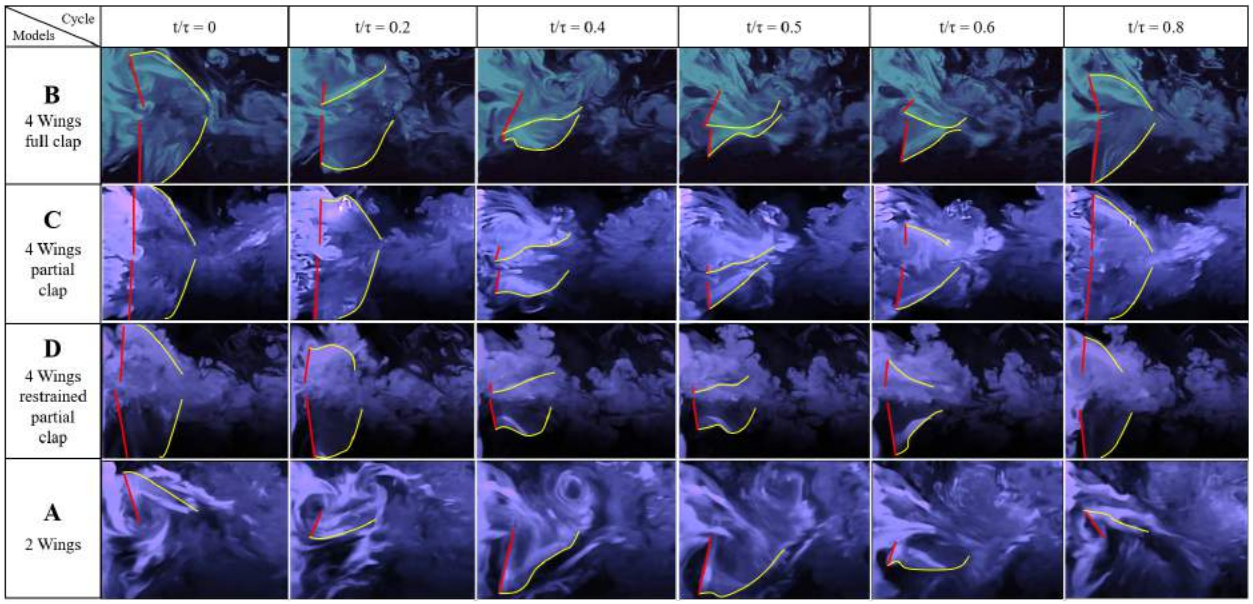

Figure A.4: Flow Visualization of the four different FWMAVs at 75% wingspan showing different time snaps (t/τ = 0, 0.2, 0.4, 0.5, 0.6 & 0.8) during a cycle where the four models are (1) 4 Wings Full Clap, (2) 4 Wings Partial Clap , (3) 4 Wings Restrained Partial Clap (4) 2 Wings

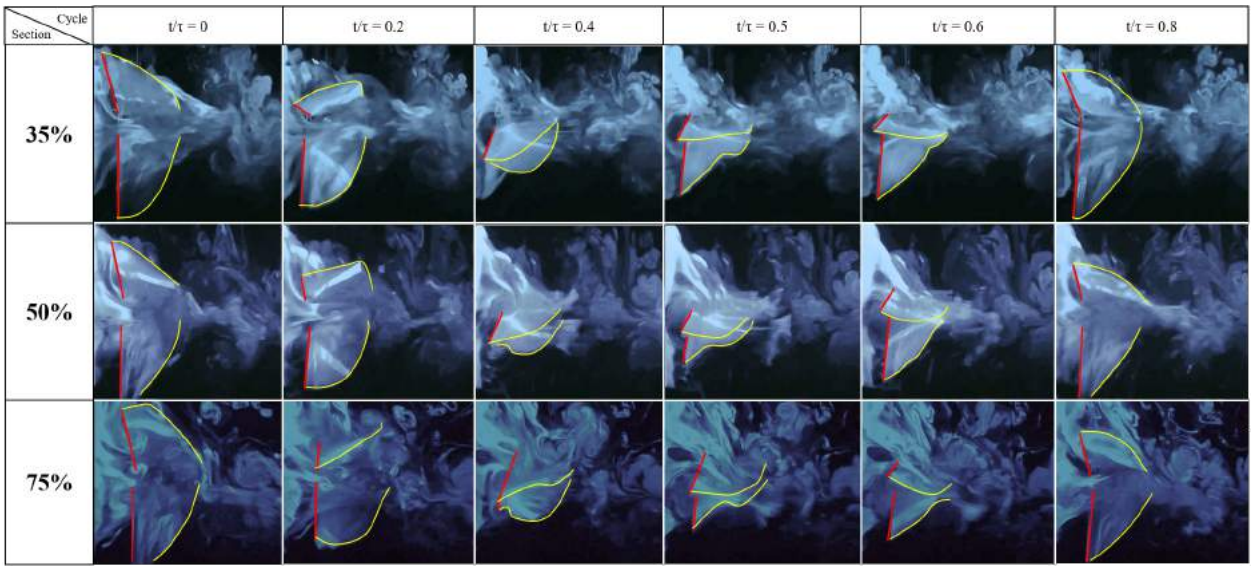

Figure A.5: Flow Visualization from Model B. Flow captured at 35%, 50% and 75% of the wingspan

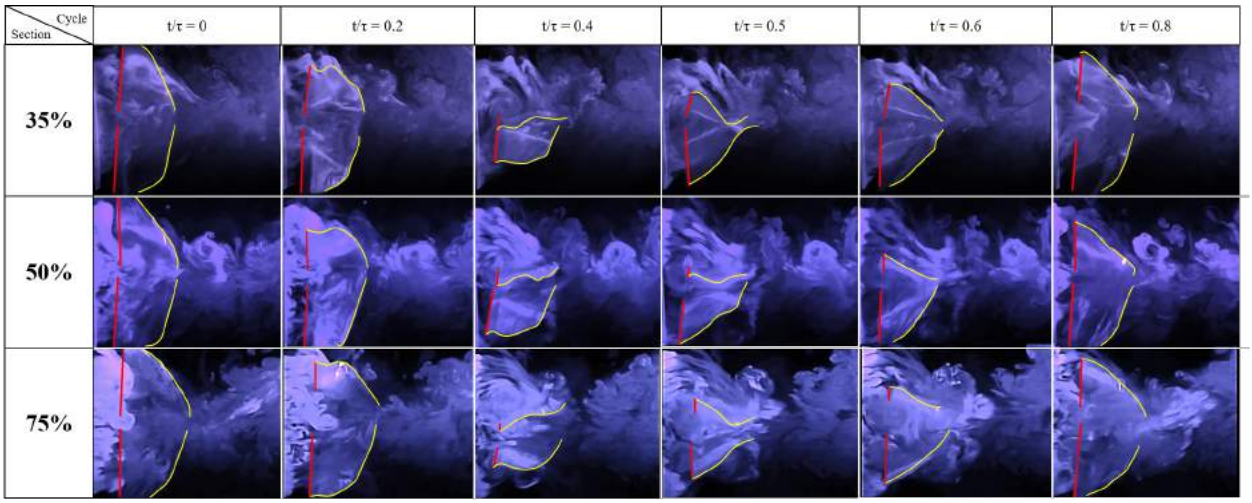

Figure A.6: Flow Visualization from Model C. Flow captured at 35%, 50% and 75% of the wingspan

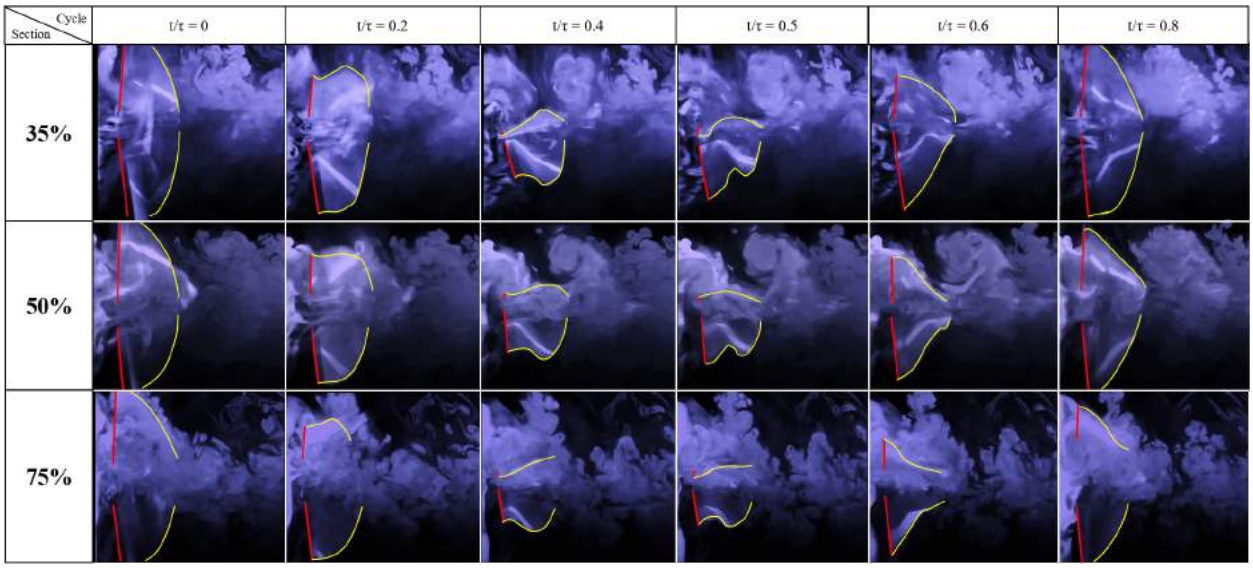

Figure A.7: Flow Visualization from Model D. Flow captured at 35%, 50% and 75% of the wingspan

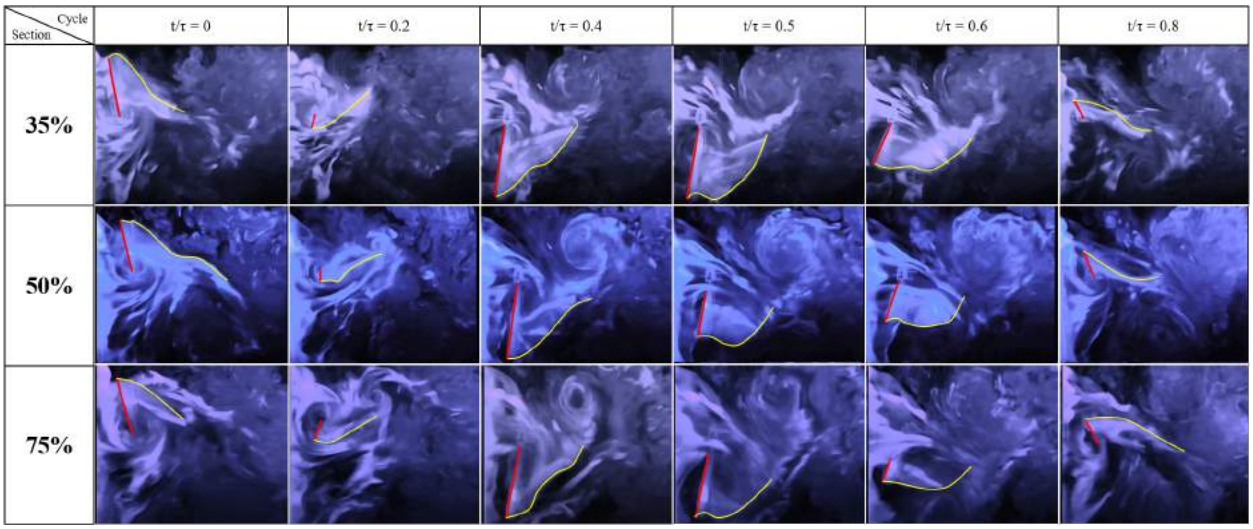

Figure A.8: Flow Visualization from Model A. Flow captured at 35%, 50% and 75% of the wingspan

A.4 Span-wise Visualization of Individual Models

There are some additional flow visualization comparison has been done on those 4 models. Figures A.5, A.6, A.7 & A.8 are looking into the flow field from a different view point. The comparison in these figures are made for a single model but for different sections of the wing. It is clear in Figure A.8 that in the phases of $t/\tau = 0.4$ & 0.5 the trailing edge votices are becoming more and more prominent closer to the tip of the wing. In Figure A.5 also the difference in relative positions of the trailing edge vortices can be seen for different sections. Same can be said for Figures A.6 & A.7.

A.5 Friction Measurement

To estimate damping in the pendulum setup, we apply a disturbance in the pendulum angle to the system without the wings. Figure A.9 shows the measured response of the pendulum angle due to such a perturbation. From these measurements, we estimate the damped frequency ($\omega_d = 0.744HZ$) and the damping ratio ($\zeta = 0.0127$), using the logarithmic

decrement rule.

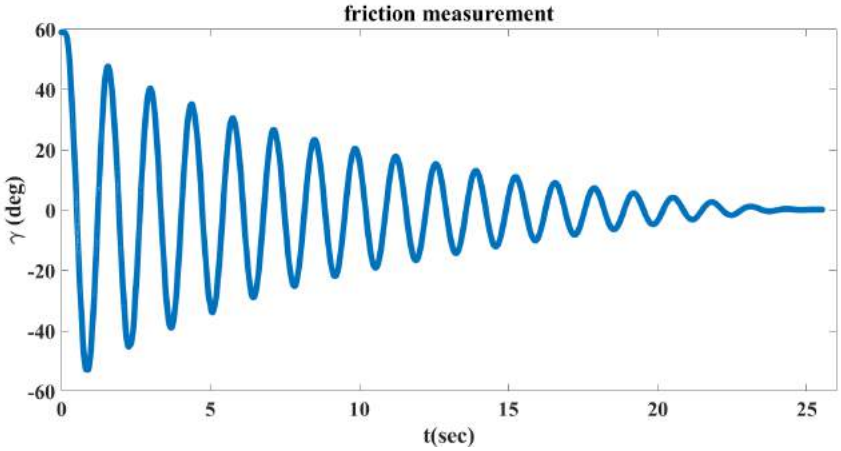

Figure A.9: Free damped oscillation of the FWMAV on the pendulum

A.6 Structural Response from the loadcell

To obtain a rough estimate of the natural frequency of the structure of the loadcell experimental setup, we performed an experimental run without the wings (so no appreciable aerodynamics). Note that the wings weigh less than 1% compared to the flapping robot. So, removing it is not expected to cause a significant change in the structural frequency of the system (it will definitely change the *aeroelastic* frequency, but this is not our concern here). In this case, zero averaged thrust is expected due to the lack of aerodynamic loads on the system.

Figure A.10 shows the time variation of the measured thrust in this case of no wings along with its FFT. The average thrust is close to zero as expected. Moreover, the FFT possesses a peak at 52 Hz irrespective of the value of the "flapping" frequency.

We use the USBPGF-S1 low pass filter from Alligator Technologies. We chose an eighth-order Butterworth filter with a cut-off frequency of 50 Hz. We expect the sharp frequency response of the eighth-order Butterworth filter to attenuate most of the content of the structural

response at 52Hz.

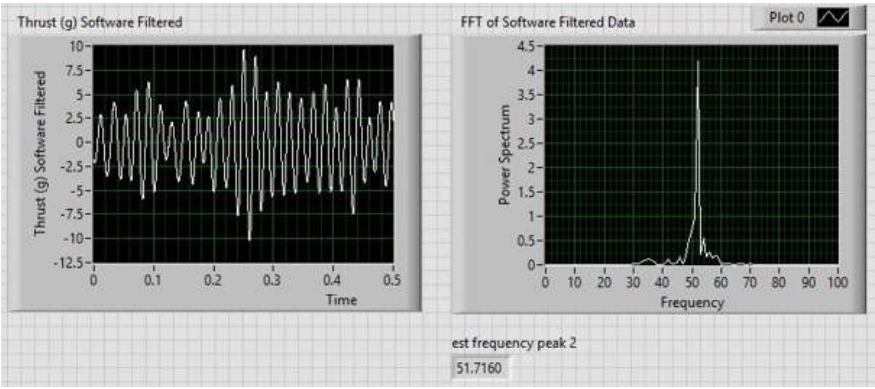

Figure A.10: Structural response from the loadcell